Continuous Variables Quantum Information in Noisy Environments

Berni, Adriano

Publication date:
2014

Document Version
Publisher's PDF, also known as Version of record

Continuous Variables Quantum Information in Noisy Environments

PhD thesis

Author:
Adriano Alberto Berni

Supervisor:
Prof. Ulrik Lund Andersen
Quantum Physics and
Information Technology

December 15, 2014

Acknowledgements

First and foremost I would like to thank my supervisor, Ulrik, for the help and encouragement he gave me in the three years and a half that I spent in the QPIT. Among the many members of my group, a special thank goes to Hugo and Amine for the countless lunch breaks spent either discussing completely random subjects or complaining about stuff while you guys roll your eyes. I would like to thank individually everyone in the QPIT, and I'll probably do it in real life. Here, on paper, I will limit myself to Jonas, Ulrich and Clemens. I spent these years mostly asking you questions. Regardless of the answers, I tank you for sharing your toughts. I learned more from you than from my own study. Among the QPIT members that left before me, I'd like to thank Mikael, Lars and Bo, with whom I started most of my projects. Unfortunately you couldn't stay to see me through. I like to think that you were smart enough to abandon the sinking ship (*i.e.* my PhD) before it was too late. Tobias deserves a special mention for the help he gave me in finalizing my project. The week we spent working in Hannover was though but (apparently) we made it, so, thank you Tobias. Apart from my colleagues, I also want to thank my fellow jugglers, especially Signe, Nathalie, Beva, Ricardo, Dana, Elias, Ogi and all the others. You're never gonna read this work but its completion wouldn't have been possible if it wasn't for your crazy sheanigans. I also want to thank my extended Danish family, Anne, Nick and Inger (and now Birk!), who welcomed me in their house and with whom I lived for the first year and a half. It has been very cozy and fun, and I can only hope to find myself a family as loving and joyful as yours. Many thanks are due to my climbing buddies. It's been a while since we met in nørrebrohallen, but I'll remember all the good advice and the fun. Many thanks also to my flatmate, Katharina. You were always around the world, for one reason or another, but the on and off time we spent sharing our cozy little house was great. I obviously thank my friends of the GUANO: Buffo, Goffo, Muffa, Loffa, Moffo and Jaffa. I used to see you almost on a daily basis for years, and it has been difficult to live all this time at a thousand kilometers from you. But you are THE MEN (all caps!), and nothing will ever change that. Finally, I thank my family for the (long distance) support. Not many packages with food arrived here, but the few that did were greatly appreciated. You walked me through the first twenty-something years of my life, and if I'm now the person that I am, is also thanks to you.

And now, let's do some physics...

Abstract

The technological progress of the last few decades has brought us the ability of exploiting quantum effects to accomplish a variety of relevant tasks. Yet, quantum phenomena are fragile, and with the ability to engineer quantum information protocols comes the problem of keeping such information safe from the detrimental effects of noise and losses. In the present work we investigate continuous variables Gaussian quantum information in noisy environments, studying the effects of various noise sources in the cases of a quantum metrological task, an error correction scheme and discord-type correlations. We engage each of the topics from a theoretical point of view, successively delving into the details of the experimental realizations and concluding with a survey of the results. In particular, we present the experimental implementation of an *ab initio*, deterministic, real-time adaptive phase estimation protocol in a realistic thermalized scenario, we investigate the performance of an error correction scheme for elimination of correlated noise in a quantum channel, and we study the robustness of discord-type quantum correlations when subject to additive noise and attenuation.

Dansk resumé

Teknologiske fremskridt indenfor de seneste årtier har givet os mulighed for at udnytte kvanteeffekter for at fuldføre en række relevante opgaver. På trods af dette er kvantefænomener skrøbelige, og med evnen til at konstruere og anvende kvanteinformationsprotokoller følger der ganske naturligt udfordringen at holde denne information intakt når den bliver udsat for støj og tab fra forskellige kilder. I denne afhandling undersøger vi Gaussisk kvanteinformation med kontinuerte variable i støjfyldte miljøer, vi studerer effekterne af forskellige støjkilder på kvantemetrologiske målinger, fejlrettende protokoller og korrelationer i tilstande med splid. Vi angriber hvert emne fra et teoretisk synspunkt, hvorefter vi beskriver detaljerne i de eksperimentelle realiseringer og konkluderer med en opsummering af resultaterne. Mere specifikt præsenterer vi en eksperimentel implementering af en *ab initio*, deterministisk, real-tid adaptiv faseestimationsprotokol i et realistisk termaliseret scenarie. Yderligere undersøger vi effektiviteten af en fejlrettende protokol der har til formål at eliminere korreleret støj i en kvantekanal, og vi studerer robustheden af kvantekorrelationer der opstår fra tilstande med splid når tilstandene er udsat for additiv støj og dæmpning.

Contents

Chapter 1

Introduction

Overview

Quantum information science has drawn the attention of the scientific community in the last few decades thanks to its ability to exploit the quantum properties of different physical systems in order to either outperform existent classical protocols, as in the case of quantum metrology [1, 2], computing [3] or error correction [4], or to introduce novel protocols which have no classical counterpart, such as quantum cryptography [5], teleportation [6] or dense coding [7].
An important drawback of all quantum protocols is their high sensitivity to noise. Entanglement and squeezing, for instance, are very fragile when they propagate through noisy and lossy channels. It is therefore of great interest to analyze the performances of different quantum information protocols in realistic environments to understand how they are negatively affected by noise and losses and to engineer new ways around such detrimental effects.
Quantum information can be encoded in either discrete (qubits) or continuous variables (CV) systems. While the former type constitute the fundamental theoretical workbench for quantum information processing, the latter has the advantage of being easier to manipulate, both from an experimental and a theoretical point of view, as we will see in Chapter 2. As a consequence, in the present work we focus on continuous-variables Gaussian systems [8, 9].
Among various physical fields, quantum optics is commonly regarded as the one in which the application of quantum information processes is mostly promising and straightforward. In fact, optical methods play a key role in many implementations of quantum information and quantum technology, since the generation of both

fundamental (e.g. vacuum and Fock states) and highly correlated quantum systems (such as squeezed and Bell states) is becoming ordinary practice in quantum optics laboratories.

Thesis structure

We start by recalling the mathematical description of CV Gaussian quantum systems in Chapter 2. We outline the theoretical framework used to describe CV quantum optical systems, focusing on the symplectic representation of phase space which is a powerful language for the description of Gaussian states and operations.

Among the different fields that constitute quantum information processing, quantum metrology occupies a special place. Indeed, measurement of physical quantities is a fundamental pillar of science and the experimental method, and it also finds countless applications in a vast number of fields. In Chapter 3 we consider the problem of quantum metrology in noisy environments. In particular, we focus on the problem of phase estimation, which in a sense can be considered almost an archetypal estimation problem in quantum physics, due to its fundamental nature and vast applicability. Specifically, we examine an *ab initio*, deterministic, real-time adaptive phase estimation protocol and we study how thermal noise affects the achievable limit on the estimation variance from both the theoretical and the experimental point of view.

Apart from the obvious problem of producing states capable of encoding high degrees of quantum information, another problem researchers in the field commonly have to deal with is how to exchange such states between parties without losing said information. Quantum states can be propagated through quantum channels, which in realistic settings contain sources of noise and are prone to losses. These effects are detrimental to the quality of the propagated information, and can be fought in different ways, for instance by encoding the quantum information in degrees of freedom that are not affected by the channel's specific noise sources, or by devising error correction protocols that are able to restore the degraded information. In Chapter 4 we consider the latter strategy by studying an error correction scheme which eliminates the correlated noise introduced by a quantum channel.

One of the most fundamental properties of quantum states responsible for the informational boost in quantum information processes is the presence of special, quantum correlations. For example, protocols such as teleportation and quantum metrology heavily rely on such correlations. Unfortunately, correlations come in

a variety of flavors and it is still not entirely clear what kind of correlations are required for what kind of applications. In Chapter 5 we focus on discord-type correlations, which the last decade has seen rising from strange theoretical discrepancy to possible candidate in a number of information applications. More specifically, we study the effect of noise on quantum discord to verify whether such correlations might be more robust than entanglement for some applications and to gain insight on its actual significance.

Chapter 2

Quantum optics formalism

In this chapter we introduce the notation and mathematical formalism used troughout the thesis. We will focus on physical systems based on continuous-spectrum quantum variables (CV), in particular on the class of Gaussian states. Gaussian states are a favourite class in CV quantum optical applications. They can be conveniently characterized and manipulated with simple analytical tools, and from an experimental point of view they are readily available in most laboratory settings, and their Gaussian properties are conserved by most linear optical transformations.

2.1 Continuous variables

We define a continuous-variable (CV) system as a physical system which has an infinite-dimensional Hilbert space described by observables with continuous spectra [8, 9]. A typical CV quantum system is composed of N bosonic modes described by field mode operators $\hat{a}_i$, $i = 1, \cdots, N$, which satisfy the commutation relation $[\hat{a}_i, \hat{a}_j^\dagger] = \delta_{i,j}$. The Hilbert space associated to such modes is therefore the tensor product $\mathcal{H}^{\otimes N} = \otimes_{i=1}^N \mathcal{H}^{(i)}$, where the $\mathcal{H}^{(i)}$ are infinite-dimensional Fock spaces. For non interacting modes, the dynamics of the system is described by the harmonic oscillator free Hamiltonian $H = \sum_{i=1}^N (\hat{n}_i + \frac{1}{2})$, with $\hat{n}_i = \hat{a}_i^\dagger \hat{a}_i$ being the number operator. The countable energy eigenbasis $\{|n\rangle_i\}_{n\in\mathbb{N}}$ is orthonormal and complete and it can be used to conveniently span the $\mathcal{H}^{(i)}$ space.
In case of a single mode system, using the Dirac formalism one can represent all the information regarding a pure quantum state as the ket $|\psi\rangle$. The state-vector

representation is only viable when the system is in a pure state, *i.e.* when we have complete control over its preparation. The most general description of a quantum state is instead obtained when we consider the state to be in a statistical mixture in which to each possible pure state $|\psi_s\rangle$ is associated a statistical distribution p_s. In such a description, we can express the state as the convex combination of the projectors over the basis $\{|\psi_s\rangle\}$ weighted by the p_s, *i.e.* as the density matrix

$$\hat{\boldsymbol{\rho}} = \sum_s p_s |\psi_s\rangle\langle\psi_s| \,. \tag{2.1}$$

For the density matrix to represent a physical system, it is required that

$$\begin{aligned} &\mathrm{Tr}\left[\hat{\boldsymbol{\rho}}\right] = 1 \\ &\hat{\boldsymbol{\rho}} = \hat{\boldsymbol{\rho}}^\dagger \\ &\langle\psi_s|\,\hat{\boldsymbol{\rho}}\,|\psi_s\rangle \geq 0 \quad \forall\, s\,. \end{aligned} \tag{2.2}$$

In the same way, a general N-mode quantum state can be fully described by a density matrix $\hat{\boldsymbol{\rho}}^{(N)}$ defined on the composite Hilbert space $\mathcal{H}^{\otimes N}$. If the state can be prepared by means of local operations on the subsystems and classical communication between them (LOCC), then it is called *separable* and it may be expressed as the product state

$$\hat{\boldsymbol{\rho}}^{(N)}_{\mathrm{sep}} = \bigotimes_{i=1}^{N} \sum_s p_s^{(i)} |\psi_s\rangle_i\langle\psi_s| = \bigotimes_{i=1}^{N} \hat{\boldsymbol{\rho}}^{(i)} \,. \tag{2.3}$$

In turn, if the state cannot be prepared by LOCC, it means that it either requires non-local operations, or non-classical communication, or both. In such a scenario, the N-mode quantum state contains quantum correlations and it cannot be expressed as a product state [10].
The density matrix of a multimode state $\hat{\boldsymbol{\rho}}^{(N)} \in \mathcal{H}^{\otimes N} = \mathcal{H}_A \otimes \mathcal{H}_B$, $\mathrm{Dim}\left[\mathcal{H}_A\right] + \mathrm{Dim}\left[\mathcal{H}_B\right] = N$, can be reduced to describe a subset of the whole system by tracing out the degrees of freedom corresponding to the remaining modes:

$$\hat{\boldsymbol{\rho}}^{(A)} = \mathrm{Tr}_{\mathcal{H}_B}\left[\hat{\boldsymbol{\rho}}^{(N)}\right] \,. \tag{2.4}$$

Moreover, if $\hat{A}$ is an operator acting on the subset $\mathcal{H}_A \subseteq \mathcal{H}^{\otimes N}$ of the system's Hilbert space, the density matrix can be used to calculate the expectation value for $\hat{A}$ according to the trace rule

$$\langle\hat{A}\rangle_{\mathcal{H}_A} = \mathrm{Tr}_{\mathcal{H}^{\otimes N}}\left[\hat{\boldsymbol{\rho}}^{(N)}\,\hat{A}\right] . \tag{2.5}$$

Finally the density matrix can be used to compute the *purity* of a state as

$$\mu(\hat{\boldsymbol{\rho}}) = \mathrm{Tr}\left[\hat{\boldsymbol{\rho}}^2\right] , \tag{2.6}$$

in fact if the state is pure then it is a projector, $\hat{\boldsymbol{\rho}}^2 = \hat{\boldsymbol{\rho}}$, and its purity is $\mu = 1$.

2.2 Phase-space representation

The bosonic field operators are not Hermitian, therefore they are not observables of the system. A Cartesian decomposition of the bosonic field operators leads to the definition of the generalized quadrature operator

$$\hat{q}_i^{\phi} = \hat{a}_i \mathrm{e}^{\imath\phi} + \hat{a}_i^{\dagger} \mathrm{e}^{-\imath\phi}, \tag{2.7}$$

where we used the natural units convention by setting $\hbar = 2$ and the variance of the vacuum fluctuations (shot noise, SN) to unity. The generalized quadrature can be used to define a position-like operator and its conjugate momentum-like operator, accordingly to the quantum harmonic oscillator treatment, as

$$\hat{q}_i^{\phi=0} =: \hat{x}_i = \hat{a}_i + \hat{a}_i^{\dagger}, \qquad \hat{q}_i^{\phi=\frac{\pi}{2}} =: \hat{p}_i = \imath(\hat{a}_i^{\dagger} - \hat{a}_i), \tag{2.8}$$

which obey the commutation relation

$$[\hat{x}_i, \hat{p}_j] = 2\imath\delta_{i,j}\,, \tag{2.9}$$

from which we obtain the Heisenberg uncertainty relation

$$\mathrm{Var}\,[\hat{x}_i]\,\mathrm{Var}\,[\hat{p}_i] \geq 1\,. \tag{2.10}$$

By grouping together the quadrature operators as $\hat{\boldsymbol{R}} = (\hat{x}_1, \hat{p}_1, \cdots, \hat{x}_N, \hat{p}_N)^{\mathrm{T}}$, $\mathrm{Dim}\left[\hat{\boldsymbol{R}}\right] = 2N$, we can rewrite the commutation relation in a more compact form as

$$[\hat{R}_i, \hat{R}_j] = 2\imath\Omega_{i,j}\,, \tag{2.11}$$

where $\Omega_{i,j}$ are elements of the $2N \times 2N$ symplectic matrix

$$\boldsymbol{\Omega} = \bigoplus_{i=1}^{N} \boldsymbol{\omega}, \qquad \boldsymbol{\omega} = \begin{pmatrix} 0 & 1 \\ -1 & 0 \end{pmatrix}. \tag{2.12}$$

Unlike $\hat{a}_i$ and $\hat{a}_i^{\dagger}$, the two quadrature operators in Eq.(2.8) are Hermitian observables of the system with continuous spectra, and their eigenvalues can be used to describe the N-modes bosonic system by introducing the phase-space representation. In particular, by introducing the Weyl displacement operator in terms of the canonical operator vector $\hat{\boldsymbol{R}}$ and of a displacement vector $\boldsymbol{\xi}$

$$\hat{D}_{\boldsymbol{\xi}} = \mathrm{Exp}\left[\imath\hat{\boldsymbol{R}}^{\mathrm{T}}\boldsymbol{\Omega}\boldsymbol{\xi}\right], \quad \boldsymbol{\xi} \in \mathbb{R}^{2N}\,, \tag{2.13}$$

the complete description of any N-mode state $\hat{\boldsymbol{\rho}}^{(N)}$ can be obtained through one of the *s-ordered characteristic functions* [11]

$$\chi_s[\hat{\boldsymbol{\rho}}^{(N)}](\boldsymbol{\xi}) = \mathrm{Tr}\left[\hat{\boldsymbol{\rho}}^{(N)}\,\hat{D}_{\boldsymbol{\xi}}\right]\mathrm{Exp}\left[s||\boldsymbol{\xi}||^2/2\right] \tag{2.14}$$

where the vector $\boldsymbol{\xi}$ belongs to the *phase space* $\Gamma = (\mathbb{R}^{2N}, \boldsymbol{\Omega})$. It is noteworthy that the tensor product structure of the Hilbert space associated with the N-mode system is translated to a direct sum structure in the real symplectic phase space, $\Gamma = \bigoplus_i \Gamma^{(i)}$, with $\Gamma^{(i)} = (\mathbb{R}^2, \boldsymbol{\omega})$ being the local phase space associated to the *i-th* mode. A complex Fourier transform of each member of the s-ordered characteristic functions class yields a *quasi-probability distribution* W_s

$$W_s[\hat{\boldsymbol{\rho}}^{(N)}](\boldsymbol{\xi}) = \frac{1}{\pi^2}\int_{\mathbb{R}^{2N}} \chi_s[\hat{\boldsymbol{\rho}}^{(N)}](\boldsymbol{\zeta})\mathrm{e}^{\imath\boldsymbol{\zeta}^{\mathrm{T}}\boldsymbol{\Omega}\boldsymbol{\xi}}\mathrm{d}^{2N}\boldsymbol{\zeta}\,. \tag{2.15}$$

The values $s = -1$ and $s = 1$ correspond respectively to the Husimi Q-function $W_{-1}(\boldsymbol{\xi})$ (antinormal ordering of the operators) and the Glauber-Sudarshan P-function $W_{+1}(\boldsymbol{\xi})$ (normal order of the operators). Of greater interest for the present work is the Wigner function, corresponding to the choice $s = 0$ (symmetrical order of the operators). For such a choice the characteristic and the Wigner functions read

$$\begin{aligned}\chi[\hat{\boldsymbol{\rho}}^{(N)}](\boldsymbol{\xi}) &= \mathrm{Tr}\left[\hat{\boldsymbol{\rho}}^{(N)}\,\hat{D}_{\boldsymbol{\xi}}\right]\,,\\ W[\hat{\boldsymbol{\rho}}^{(N)}](\boldsymbol{R}) &= \frac{1}{(2\pi)^{2N}}\int_{\mathbb{R}^{2N}}\mathrm{Exp}\left[-\imath\boldsymbol{R}^{\mathrm{T}}\boldsymbol{\Omega}\boldsymbol{\xi}\right]\chi[\hat{\boldsymbol{\rho}}^{(N)}](\boldsymbol{\xi})\mathrm{d}^{2N}\boldsymbol{\xi}\,,\end{aligned} \tag{2.16}$$

where $\boldsymbol{R} \in \mathbb{R}^{2N}$ is the vector of the eigenvalues of the quadrature operators arranged in the previously defined $\hat{\boldsymbol{R}}$ operator-array. An equivalent definition of the Wigner function which highlights its univocal correspondence with the density matrix can be obtained by writing it in terms of the eigenvectors of the quadrature operators as

$$W[\hat{\boldsymbol{\rho}}^{(N)}](\boldsymbol{x},\boldsymbol{p}) = \frac{1}{(2\pi)^N}\int_{\mathbb{R}^N}\langle\boldsymbol{x}+\boldsymbol{y}|\,\hat{\boldsymbol{\rho}}\,|\boldsymbol{x}-\boldsymbol{y}\rangle\mathrm{Exp}\left[2\imath\boldsymbol{y}\cdot\boldsymbol{p}\right]\mathrm{d}^N\boldsymbol{y}. \tag{2.17}$$

Although the Wigner function is in general non-positive, it is bounded and regular and therefore it is a well behaved function for any quantum state. The Wigner function representation of a quantum state results advantageous in that it allows to compute expectation values and other important quantities as integrals in the phase-space. For instance, the Wigner function's marginal distributions yield the

quadrature operators probability distributions:

$$P(\boldsymbol{x}) = \int_{\mathbb{R}^N} W[\hat{\boldsymbol{\rho}}^{(N)}](\boldsymbol{x},\boldsymbol{p})\mathrm{d}^N\boldsymbol{p}$$
$$P(\boldsymbol{p}) = \int_{\mathbb{R}^N} W[\hat{\boldsymbol{\rho}}^{(N)}](\boldsymbol{x},\boldsymbol{p})\mathrm{d}^N\boldsymbol{x}\,. \tag{2.18}$$

Also the trace rule of Eq.(2.5) has an analogous formulation in the phase-space in terms of Wigner functions as

$$\mathrm{Tr}\left[\hat{\boldsymbol{\rho}}^{(N)}\,\hat{A}\right] = (2\pi)^{2N}\int_{\mathbb{R}^{2N}} W[\hat{\boldsymbol{\rho}}^{(N)}](\boldsymbol{R})W[\hat{A}](\boldsymbol{R})\mathrm{d}^{2N}\boldsymbol{R}\,. \tag{2.19}$$

The advantage of this mathematical formulation will become obvious in the case of Gaussian states, as explained in Sec.2.3.
Given a quantum state, both the characteristic and the Wigner function can be expressed in terms of its statistical moments [12]. The first moment of the state, also called *displacement vector*, is defined as the mean value of the field quadrature array

$$\boldsymbol{\delta} = \langle\hat{\boldsymbol{R}}\rangle = \mathrm{Tr}\left[\hat{\boldsymbol{R}}\,\hat{\boldsymbol{\rho}}\right]\,, \tag{2.20}$$

while the second moment, known as *covariance matrix*, is composed of the matrix elements

$$\sigma_{ij} = \frac{1}{2}\mathrm{Tr}\left[\hat{\boldsymbol{\rho}}\{\hat{R}_i,\hat{R}_j\}\right] - \mathrm{Tr}\left[\hat{\boldsymbol{\rho}}\,\hat{R}_j\right]\mathrm{Tr}\left[\hat{\boldsymbol{\rho}}\,\hat{R}_i\right]\,, \tag{2.21}$$

where $\{\cdot,\cdot\}$ denotes the anticommutator. The covariance matrix is a $2N\times 2N$ real and symmetric matrix which contains the variances of the field quadratures in its diagonal terms, the correlations between different quadratures in the diagonal block matrices and the correlations between modes in the antidiagonal block matrices. The uncertainty relations for the canonical operators in Eq.(2.10) impose a constraint on the covariance matrix in the form of the following inequality

$$\hat{\boldsymbol{\sigma}} + \imath\boldsymbol{\Omega} \geq 0\,, \tag{2.22}$$

which also expresses the requirement of positive-definiteness of the density matrix [13].

2.3 Gaussian states and operations

Gaussian states are commonly considered essentialfor CV quantum information tasks, due to the fact that the fundamental vacuum state of the radiation field is

Gaussian itself. Moreover, most quantum transformations are defined by Hamiltonians at most bilinear in the field modes, which preserve the Gaussian character of the quantum states undergoing such transformations. Finally, also partial trace operations, used to compute expectation values as in Eq.(2.5) or reduced density operators as in Eq.(2.4), preserve the Gaussianity of the state.
A Gaussian state is defined as any quantum state which can be expressed in terms of Gaussian characteristic and Wigner functions [8]

$$\chi[\hat{\boldsymbol{\sigma}}](\boldsymbol{\xi}) = \mathrm{Exp}\left[-\frac{1}{2}\boldsymbol{\xi}^{\mathrm{T}}(\boldsymbol{\Omega}\,\hat{\boldsymbol{\sigma}}\,\boldsymbol{\Omega}^{\mathrm{T}})\boldsymbol{\xi} - \imath(\boldsymbol{\Omega}\boldsymbol{\delta})^{\mathrm{T}}\boldsymbol{\xi}\right] ,$$
$$W[\hat{\boldsymbol{\sigma}}](\boldsymbol{R}) = \frac{\mathrm{Exp}\left[-\frac{1}{2}(\boldsymbol{R}-\boldsymbol{\delta})^{\mathrm{T}}\,\hat{\boldsymbol{\sigma}}^{-1}(\boldsymbol{R}-\boldsymbol{\delta})\right]}{(2\pi)^{\mathrm{N}}\sqrt{\mathrm{Det}\,[\hat{\boldsymbol{\sigma}}]}} . \tag{2.23}$$

Given that the first moment of a state can be arbitrarily changed by phase-space translations, which are local unitary operations and therefore don't affect informational quantities such as entanglement or entropy, in the following we will consider $\boldsymbol{\delta} = 0$, unless otherwise stated. This implies that the covariance matrix, despite being finite-dimensional, is enough to fully determine the state of a CV system supported by an infinite-dimensional Hilbert space.
A remarkable property of Gaussian states is found in the Hudson theorem [14], which states a necessary and sufficient condition for a quantum state to be Gaussian is that the state is pure and its Wigner function positive. Therefore all pure states with a positive Wigner function are Gaussian states. This result was later extended to mixed states in [15], where upper and lower bounds on the non-Gaussianity of mixed states were found. It is easy to characterize the purity of a Gaussian state by applying the trace rule in phase space of Eq.(2.19) to the definition of state purity in Eq.(2.6):

$$\mu(\hat{\boldsymbol{\rho}}) = (2\pi)^{2N}\int_{\mathbb{R}^{2N}} W[\hat{\boldsymbol{\sigma}}]^2(\boldsymbol{R})\mathrm{d}^{2N}\boldsymbol{R} = \frac{1}{\sqrt{\mathrm{Det}\,[\hat{\boldsymbol{\sigma}}]}} . \tag{2.24}$$

Therefore a Gaussian state is pure if and only if $\mathrm{Det}\,[\hat{\boldsymbol{\sigma}}] = 1$, always in the natural units $\hbar = 2$.
Let's now focus on quantum optical transformations that are commonly used in CV Gaussian quantum information processing, *i.e.* linear optical transformations. A quantum operation is a completely positive linear map $\mathcal{E} : \hat{\boldsymbol{\rho}} \to \mathcal{E}(\hat{\boldsymbol{\rho}})$ that is in general trace-decreasing, $0 \leq \mathrm{Tr}\,[\mathcal{E}(\hat{\boldsymbol{\rho}})] \leq 1$. In the case in which the map is trace preserving, $\mathrm{Tr}\,[\mathcal{E}(\hat{\boldsymbol{\rho}})] = 1$, the operation is called a *quantum channel*. Moreover, if such quantum channel is reversible, it can be represented by a unitary transformation $\hat{\boldsymbol{\rho}} \to U\,\hat{\boldsymbol{\rho}}\,U^{\dagger}$, with $U^{-1} = U^{\dagger}$. We define Gaussian unitaries the reversible

quantum channels which transform Gaussian states in Gaussian states. In order for a unitary transformation to preserve the Gaussian character of a quantum state, the Hamiltonian that generates it is required to be at most quadratic in the mode operators, therefore affecting only the first and second moments of the state [12]. The most general N-mode Hamiltonian generating a Gaussian unitary can therefore be written as

$$H = \sum_{i=1}^{N} g_i^{(1)} \hat{a}_i^\dagger + \sum_{i>j=1}^{N} g_{ij}^{(2)} \hat{a}_i^\dagger \hat{a}_j + \sum_{i,j=1}^{N} g_{ij}^{(3)} \hat{a}_i^\dagger \hat{a}_j^\dagger + h.c. \,. \tag{2.25}$$

Mode transformations induced by such Hamiltonians are mapped to real symplectic transformations on the first and second moments according to

$$\begin{aligned} \boldsymbol{R}' &= \hat{\boldsymbol{S}} \boldsymbol{R} + \boldsymbol{\delta} \\ \hat{\boldsymbol{\sigma}}' &= \hat{\boldsymbol{S}}\, \hat{\boldsymbol{\sigma}}\, \hat{\boldsymbol{S}}^{\mathrm{T}} \,, \end{aligned} \tag{2.26}$$

where $\hat{\boldsymbol{S}}$ is a symplectic matrix, satisfying $\hat{\boldsymbol{S}} \boldsymbol{\Omega} \hat{\boldsymbol{S}}^\dagger = \boldsymbol{\Omega}$, and $\boldsymbol{\delta}$ is the displacement vector. In turn, symplectic transformations of the form in Eq.2.26 are generated by unitary transformations imposed by Hamiltonian operators of the form in Eq.(2.25) [16].
In the following, to study the Gaussian states and unitary transformations of interest, we will consider only single-mode and two-mode states and transformations.

2.3.1 Single-mode states and operations

The fundamental quantum optical state is the ground state of the radiation field, called *vacuum state*, usually indicated as $|0\rangle$ or with the density operator $\hat{\boldsymbol{\rho}}_0 = |0\rangle\langle 0|$. The vacuum state is the eigenstate of the annihilation operator, $\hat{a}|0\rangle = 0$, and it is an eigenvector of the state energy, therefore it is part of the Fock basis. Its mean energy and energy fluctuations are both zero

$$\begin{aligned} \langle \hat{n} \rangle_0 &= \mathrm{Tr}\left[\hat{n}\, \hat{\boldsymbol{\rho}}_0\right] = 0 \,, \\ (\Delta \hat{n}^2)_0 &= \mathrm{Tr}\left[\hat{n}^2\, \hat{\boldsymbol{\rho}}_0\right] - \mathrm{Tr}\left[\hat{n}\, \hat{\boldsymbol{\rho}}_0\right]^2 = 0 \,. \end{aligned} \tag{2.27}$$

In the phase space picture, the vacuum state is centered on the position and momentum axes origin, in fact the mean value of both $\hat{x}$ and $\hat{p}$ are zero, while their fluctuations are subject to the Heisenberg uncertainty of Eq.2.10, therefore

$$\begin{aligned} \langle \hat{x} \rangle_0 &= \langle \hat{p} \rangle_0 = 0 \,, \\ (\Delta \hat{x}^2)_0 &= (\Delta \hat{p}^2)_0 = 1 \,. \end{aligned} \tag{2.28}$$

Indeed, by setting $\hbar = 2$ we fixed the vacuum fluctuations at unity, therefore normalizing them at the Shot Noise level. As a consequence, the covariance matrix of the single-mode vacuum state is simply the 2-dimensional identity matrix, $\hat{\boldsymbol{\sigma}}_0 = \mathbb{I}$, expressing the idea that the vacuum state is a *minimum uncertainty* state. Finally, the Wigner function is easily calculated as in Eq.(2.23) with $\boldsymbol{\delta} = 0$:

$$W[\hat{\boldsymbol{\rho}}_0](x,p) = \frac{1}{2\pi}\mathrm{Exp}\left[-\frac{x^2+p^2}{2}\right] . \tag{2.29}$$

Another fundamental single mode state of the quantized optical field is the thermal state, which is the state of the field emitted by an ideal black body at temperature T. Its density matrix reads

$$\hat{\boldsymbol{\rho}}_{\mathrm{th}} = \sum_{n=0}^{\infty} \nu_n |n\rangle\langle n| , \qquad \nu_n = \frac{\mathrm{n_{th}}^n}{(\mathrm{n_{th}}+1)^{n+1}} , \tag{2.30}$$

where $\mathrm{n_{th}}$ is the mean energy of the state, which is related to the black body temperature T according to $\mathrm{n_{th}} = (\mathrm{Exp}\left[\frac{\hbar\omega}{k_\mathrm{B}T}\right]-1)^{-1}$, whith ω being the frequency of the radiation mode, and k_B the Boltzmann's constant. The mean state energy and its fluctuations are once again calculated using the trace rule:

$$\begin{aligned} \langle\hat{n}\rangle_{\hat{\boldsymbol{\rho}}_{\mathrm{th}}} &= \mathrm{Tr}\left[\hat{n}\,\hat{\boldsymbol{\rho}}_{\mathrm{th}}\right] = \mathrm{n_{th}} , \\ (\Delta\hat{n}^2)_{\hat{\boldsymbol{\rho}}_{\mathrm{th}}} &= \mathrm{Tr}\left[\hat{n}^2\,\hat{\boldsymbol{\rho}}_{\mathrm{th}}\right] - \mathrm{Tr}\left[\hat{n}\,\hat{\boldsymbol{\rho}}_0\right]^2 = \mathrm{n_{th}} + \mathrm{n_{th}}^2 . \end{aligned} \tag{2.31}$$

Just like a vacuum state, the thermal state in the phase space representation is centered on the origin of the position and momentum axes, but the fluctuations of the quadratures are not minimum anymore:

$$\begin{aligned} \langle\hat{x}\rangle_{\hat{\boldsymbol{\rho}}_{\mathrm{th}}} &= \langle\hat{p}\rangle_{\hat{\boldsymbol{\rho}}_{\mathrm{th}}} = 0 , \\ (\Delta\hat{x}^2)_{\hat{\boldsymbol{\rho}}_{\mathrm{th}}} &= (\Delta\hat{p}^2)_{\hat{\boldsymbol{\rho}}_{\mathrm{th}}} = 2\,\mathrm{n_{th}}+1 , \end{aligned} \tag{2.32}$$

in fact thermalization can be regarded as an homogeneous expansion of the phase space by a factor $2\,\mathrm{n_{th}}+1$. As a consequence, the covariance matrix of a thermal state is simply the covariance matrix of the vacuum rescaled by the thermal variance, $\hat{\boldsymbol{\sigma}}_{\mathrm{th}} = (2\,\mathrm{n_{th}}+1)\,\mathbb{I}$. Finally, from the covariance matrix we can calculate the Wigner function,

$$W[\hat{\boldsymbol{\rho}}_{\mathrm{th}}](x,p) = \frac{1}{2(2\,\mathrm{n_{th}}+1)\pi}\mathrm{Exp}\left[-\frac{x^2+p^2}{2(2\,\mathrm{n_{th}}+1)}\right] . \tag{2.33}$$

The vacuum and the thermal states are the fundamental Gaussian states of the optical field. By applying Gaussian unitaries imposed by the Eq.(2.25) Hamiltonian to such states we can build the whole class of Gaussian states.

Let's now study in detail the Gaussian unitaries defined by each component of the Hamiltonian in Eq.(2.25) and the states that derive from them.
The first component of the Hamiltonian in Eq.(2.25), $H \propto g^{(1)}\hat{a}^\dagger + h.c.$, is linear in the field modes and it generates the unitary *displacement* operator, which can be obtained from the Weyl displacement operator of Eq.(2.13) by setting $\boldsymbol{\xi} = (\mathfrak{Re}\,[\alpha]\,, \mathfrak{Im}\,[\alpha])$, with $\alpha \in \mathbb{C}$ being the displacement's complex amplitude:

$$\hat{D}(\alpha) = \mathrm{Exp}\left[\alpha\hat{a}^\dagger - \alpha^*\hat{a}\right] \ . \tag{2.34}$$

Such operator can be used to define the important family of *coherent* states [17] by displacing the vacuum state as in $\hat{D}(\alpha)|0\rangle = |\alpha\rangle$. Equivalently, coherent states can be defined as the eigenstates of the annihilation operator, $\hat{a}|\alpha\rangle = \alpha|\alpha\rangle$. The displacement operator applied to the field modes gives the mode evolution

$$\begin{aligned} \hat{D}(\alpha)\hat{a}\hat{D}^\dagger(\alpha) &= \hat{a} - \alpha\,, \\ \hat{D}(\alpha)\hat{a}^\dagger\hat{D}^\dagger(\alpha) &= \hat{a}^\dagger - \alpha^* \ . \end{aligned} \tag{2.35}$$

The expansion in the number basis of a coherent states is given by

$$|\alpha\rangle = \mathrm{e}^{-\frac{|\alpha|^2}{2}} \sum_{n=0}^{\infty} \frac{\alpha^n}{\sqrt{n!}}|n\rangle\,, \tag{2.36}$$

and it can be used to easily compute the mean energy of the state and its fluctuations:

$$\begin{aligned} \langle\hat{n}\rangle_{\hat{\boldsymbol{\rho}}_\alpha} &= \mathrm{Tr}\left[\hat{n}|\alpha\rangle\langle\alpha|\right] = |\alpha|^2\,, \\ (\Delta\hat{n}^2)_{\hat{\boldsymbol{\rho}}_\alpha} &= \mathrm{Tr}\left[\hat{n}^2|\alpha\rangle\langle\alpha|\right] - \mathrm{Tr}\left[\hat{n}|\alpha\rangle\langle\alpha|\right]^2 = |\alpha|^2\,, \end{aligned} \tag{2.37}$$

from which becomes apparent the Poissonian character of the photon number distribution. Coherent states are often called *classical* states due to their properties which are similar to the ones of a classical harmonic oscillator. Indeed, since their noise profile does not depend on their energy, a coherent state with a large amplitude is a good approximation of a classical state, in which the noise is negligible with respect to the amplitude. Since the Hamiltonian that generates the displacement transformation is linear in the field modes it only affects the first moments of the state, hence the corresponding symplectic form of $\hat{D}(\alpha)$ is the identity matrix $\hat{D}_\alpha^\Gamma = \mathbb{I}_2$. As a consequence, coherent states preserve the minimum uncertainty properties of the vacuum and are described by the same covariance matrix, the 2-dimensional identity matrix, while the mean values of the quadrature operators are related to the displacement amplitude as $\langle\hat{x}\rangle_{\hat{\boldsymbol{\rho}}_\alpha} = \alpha + \alpha^* = 2\mathfrak{Re}\,[\alpha]$ and

$\langle\hat{p}\rangle_{\hat{\boldsymbol{\rho}}_\alpha} = i(\alpha^* - \alpha) = 2\mathfrak{Im}\,[\alpha]$. Overall, such properties indicate that the Wigner function of a coherent state is the Wigner function of a vacuum state displaced by the complex value α, which can be obtained from Eq.(2.23) by setting the displacement vector to $\boldsymbol{\delta} = (\langle\hat{x}\rangle_{\hat{\boldsymbol{\rho}}_\alpha}, \langle\hat{p}\rangle_{\hat{\boldsymbol{\rho}}_\alpha})^{\mathrm{T}}$:

$$W[\hat{\boldsymbol{\rho}}_\alpha](x,p) = \frac{1}{2\pi}\mathrm{Exp}\left[-\frac{(x-\langle\hat{x}\rangle_{\hat{\boldsymbol{\rho}}_\alpha})^2 + (p-\langle\hat{p}\rangle_{\hat{\boldsymbol{\rho}}_\alpha})^2}{2}\right] . \tag{2.38}$$

A remarkable property of coherent states is that they constitute an overcomplete basis of the Hilbert space, *i.e.* they are a complete basis of non-orthogonal states:

$$\begin{aligned} &\frac{1}{\pi}\int_{\mathbb{C}} |\alpha\rangle\langle\alpha|\mathrm{d}^2\alpha = 1\,, \\ &\langle\alpha|\beta\rangle = \mathrm{e}^{-\frac{1}{2}(|\alpha|^2+|\beta|^2-2\alpha^*\beta)}\,, \end{aligned} \tag{2.39}$$

therefore they can be used to expand density operators on the Hilbert space:

$$\hat{\boldsymbol{\rho}} = \int_{\mathbb{C}} P(\alpha)|\alpha\rangle\langle\alpha|\mathrm{d}^2\alpha \tag{2.40}$$

where $P(\alpha)$ is the Glauber-Sudarsahan P-function, obtained from Eq.(2.15) with $s = +1$.

The second component of the Hamiltonian of Eq.(2.25), $H \propto g^{(2)}\hat{a}^\dagger\hat{b} + h.c.$, describes a free evolution of the modes when the mode operators $\hat{a}$ and $\hat{b}$ refer both to the same mode, *i.e.*, $H \propto g^{(2)}\hat{a}^\dagger\hat{a} + h.c.$. Such Hamiltonian generates the unitary *phase-shift* operator:

$$\hat{U}(\phi) = \mathrm{Exp}\left[-\imath\phi\hat{a}^\dagger\hat{a}\right] \tag{2.41}$$

where ϕ is the phase parameter. The corresponding symplectic transformation in the real basis is given by

$$\hat{U}^\Gamma_\phi = \begin{pmatrix} \cos(\phi) & \sin(\phi) \\ -\sin(\phi) & \cos(\phi) \end{pmatrix} . \tag{2.42}$$

A more detailed description of the phase operator will be given in Sec.3.1.

Finally, the third component of the Eq.(2.25) Hamiltonian, $H \propto g^{(3)}(\hat{a}^\dagger)^2 + h.c.$, represents the bilinear evolution of a single-mode field, corresponding to the dynamics of a degenerate parametric amplifier, which is an active optical transformation. Such Hamiltonian generates the unitary single-mode *squeezing* operator

$$\hat{S}(z) = \mathrm{Exp}\left[\frac{1}{2}(z^*(\hat{a})^2 - z(\hat{a}^\dagger)^2)\right] , \qquad z = r\mathrm{e}^{2\imath\psi} \tag{2.43}$$

where r is the squeezing strength and ψ the squeezing phase. Applying the squeezing operator to a vacuum state results in the *squeezed vacuum state*, which can be expressed in the number basis as the superposition of even number states

$$\hat{S}(z)|0\rangle = |0,z\rangle = \frac{1}{\sqrt{\cosh(r)}}\sum_{n=0}^{\infty}\frac{\sqrt{(2n)!}}{n!}\left(\frac{\mathrm{e}^{2\imath\psi}\sinh(r)}{2\cosh(r)}\right)^{n}|2n\rangle\ . \tag{2.44}$$

Squeezed states were introduced theoretically by Stoler in 1970 [18] as states in which one of the quadratures presents sub-vacuum noise and the conjugate quadrature has super-vacuum noise, the overall state being a minimum uncertainty state. The mode evolution corresponding to the squeezing operator in Eq.(2.43) is given by

$$\begin{aligned}\hat{S}(z)\hat{a}\hat{S}^{\dagger}(z) &= \cosh(r)\hat{a} + \mathrm{e}^{2\imath\psi}\sinh(r)\hat{a}^{\dagger}\,,\\ \hat{S}(z)\hat{a}^{\dagger}\hat{S}^{\dagger}(z) &= \cosh(r)\hat{a}^{\dagger} + \mathrm{e}^{-2\imath\psi}\sinh(r)\hat{a}\,,\end{aligned} \tag{2.45}$$

which can be used, together with the cyclic property of the trace, to calculate squeezed vacuum energy and its fluctuations as

$$\begin{aligned}\langle\hat{n}\rangle_{\hat{\boldsymbol{\rho}}_z} &= \mathrm{Tr}\left[\hat{n}\hat{S}(z)|0\rangle\langle 0|\hat{S}^{\dagger}(z)\right] = \sinh^2(r)\,,\\ (\Delta\hat{n}^2)_{\hat{\boldsymbol{\rho}}_z} &= \mathrm{Tr}\left[\hat{n}^2\hat{S}(z)|0\rangle\langle 0|\hat{S}^{\dagger}(z)\right] - \mathrm{Tr}\left[\hat{n}\hat{S}(z)|0\rangle\langle 0|\hat{S}^{\dagger}(z)\right]^2 =\\ &= 2\cosh^2(r)\sinh^2(r)\ ,\end{aligned} \tag{2.46}$$

indicating a nonzero mean number of photons and a sub-Poissonian statistics. The symplectic form of the squeezing operator reads

$$\hat{S}_z^{\Gamma} = \begin{pmatrix}\cosh(r)-\cos(2\psi)\sinh(r) & \sin(2\psi)\sinh(r)\\ \sin(2\psi)\sinh(r) & \cosh(r)+\cos(2\psi)\sinh(r)\end{pmatrix}\ , \tag{2.47}$$

and it can be used to calculate the squeezed vacuum covariance matrix using the symplectic transformation in Eq.(2.26). Two cases are especially important, namely *amplitude-squeezing*, for which the squeezed vacuum covariance matrix reads $(\hat{\boldsymbol{\sigma}}_z)|_{\psi=0} = \mathrm{Diag}\,[\mathrm{e}^{-2r},\mathrm{e}^{2r}]$, and *phase-squeezing*, for which $(\hat{\boldsymbol{\sigma}}_z)|_{\psi=\pi/2} = \mathrm{Diag}\,[\mathrm{e}^{2r},\mathrm{e}^{-2r}]$. It is easy to see from both these cases that the product of the quadrature variances are equal to the vacuum noise, which is the unity in natural units, therefore saturating the Heisenberg uncertainty and thus classifying themselves as minimum uncertainty states. Using Eq.(2.23) makes possible to express the Wigner function for an amplitude squeezed vacuum state as

$$W[\hat{\boldsymbol{\rho}}_z](x,p) = \frac{1}{2\pi}\mathrm{Exp}\left[-\frac{1}{2}\left(\mathrm{e}^{-2r}p^2+\mathrm{e}^{2r}x^2\right)\right]\ , \tag{2.48}$$

while for a phase squeezed state the exponential factors for x^2 and p^2 are swapped. Fig.2.1 illustrates the density matrices and Wigner functions of the four above mentioned Gaussian states.

2.3.2 Two-mode states and operations

One of the most essential passive linear optical element is the *beam splitter* (BS), which is in general composed of glass prisms separated by a dielectric medium that reflects part of the incoming radiation and transmits the rest. The beam splitter interaction is based on the linear mixing of two input optical modes, described by the second component of the Eq.(2.25) Hamiltonian when we consider two modes of the radiation, $H \propto g^{(2)}\hat{a}^\dagger\hat{b} + h.c.$. It follows that in the quantum description a beam splitter always has two input and two output modes. The unitary operator that defines the beam-splitter interaction of modes $\hat{a}$ and $\hat{b}$ is given by (cfr. Fig.2.2)

$$\hat{B}_\kappa = \mathrm{Exp}\left[\kappa\hat{a}^\dagger\hat{b} - \kappa^*\hat{a}\hat{b}^\dagger\right] , \qquad \kappa = \phi e^{\imath\theta} \in \mathbb{C} , \tag{2.49}$$

where the coupling κ depends in general on the interaction time and the linear susceptibility of the medium. It is quite informative to derive the evolution of the two input modes, which can be obtained from the unitary operator of Eq.(2.49) through the Baker-Campbell-Hausdorff formula [19] as

$$\begin{aligned} \begin{pmatrix} \hat{a}' \\ \hat{b}' \end{pmatrix} &= \hat{B}_\kappa \begin{pmatrix} \hat{a} \\ \hat{b} \end{pmatrix} \hat{B}_\kappa^\dagger = \hat{B}_\kappa^{\mathcal{H}} \begin{pmatrix} \hat{a} \\ \hat{b} \end{pmatrix} \\ \hat{B}_\kappa^{\mathcal{H}} &= \begin{pmatrix} \sqrt{\tau} & e^{\imath\theta}\sqrt{1-\tau} \\ -e^{-\imath\theta}\sqrt{1-\tau} & \sqrt{\tau} \end{pmatrix} , \end{aligned} \tag{2.50}$$

where $\hat{B}_\kappa^{\mathcal{H}}$ is the matrix that defines the transformation of the modes, and $\tau = \cos^2(\phi)$ is the *transmittivity* of the beam-splitter. In most applications one has either $\theta = \pi/2$ and $\tau = 1/2$, which corresponds to a balanced beam splitter where the reflected beam has an additional $\pi/2$ phase. In the following we will take $\theta = \pi/2$ but we will keep the splitting ratio undefined, since non-balanced beam splitters are extremely useful to model optical attenuation and in various experimental applications.

The symplectic operation associated to a $\pi/2$ phase beam splitter reads:

$$\hat{B}_\kappa^{\Gamma} = \begin{pmatrix} \sqrt{\tau} & 0 & 0 & -\sqrt{1-\tau} \\ 0 & \sqrt{\tau} & \sqrt{1-\tau} & 0 \\ 0 & -\sqrt{1-\tau} & \sqrt{\tau} & 0 \\ \sqrt{1-\tau} & 0 & 0 & \sqrt{\tau} \end{pmatrix} . \tag{2.51}$$

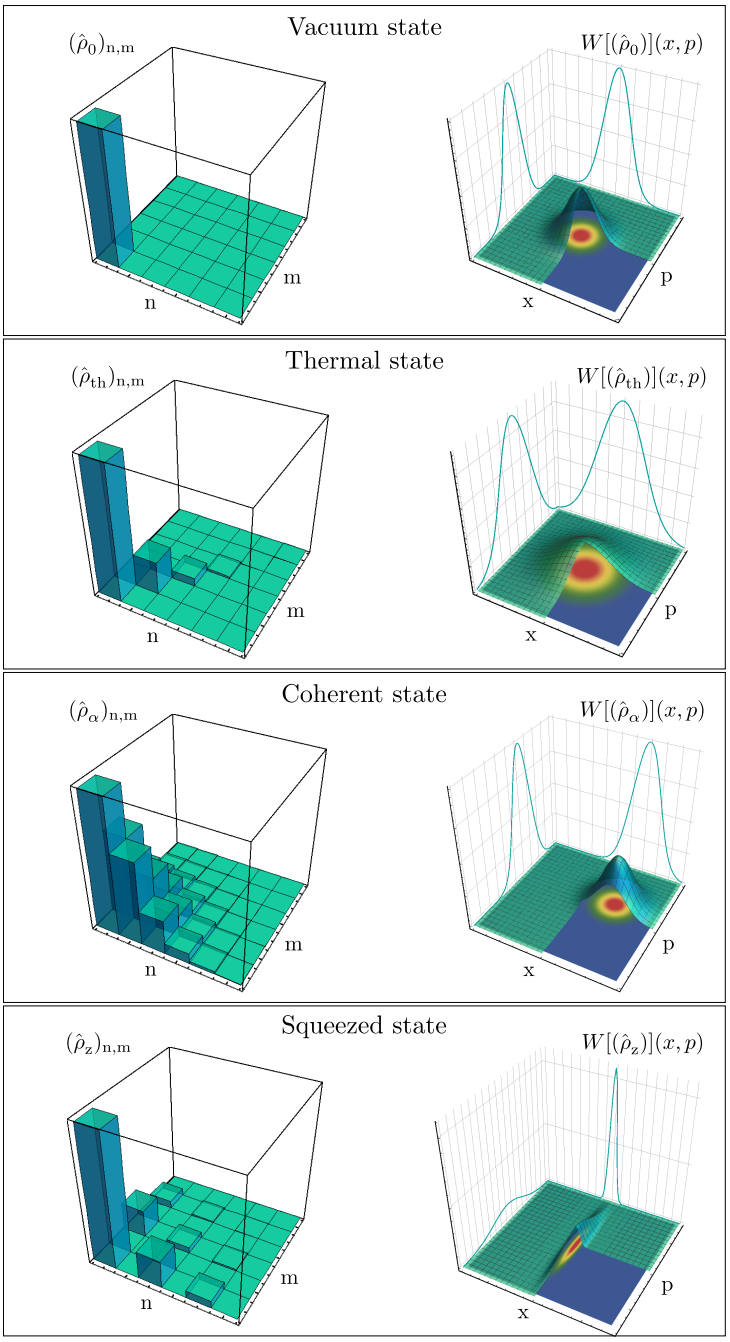

Figure 2.1: **Fundamental CV Gaussian quantum states.** Density matrices (left column) and Wigner functions (right column) of a vacuum state (top), thermal state (middle top) with $n_{\mathrm{th}} = 1$, coherent state (middle bottom) with $\alpha = 1 + \imath/2$ and single-mode amplitude-squeezed state (bottom) with $r = 1$ and $\psi = 0$. The density matrices elements are displayed in a truncated finite-dimensional Hilbert space in the number (Fock) basis. The Wigner functions are plotted in the phase space, with the contour displayed underneath and the x and p marginal distributions on the side faces.

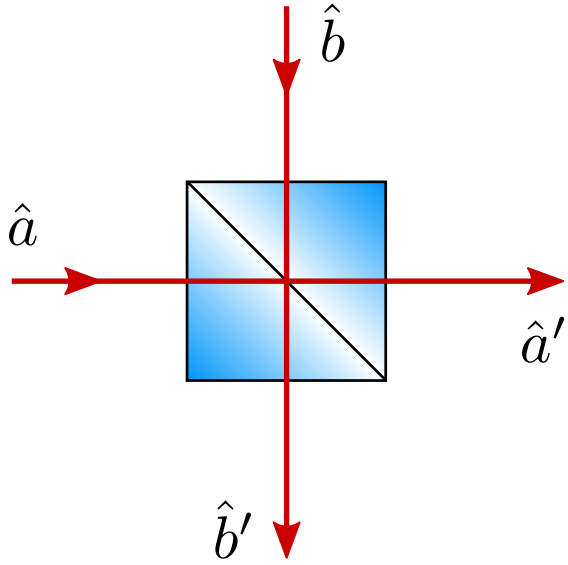

Figure 2.2: **Beam splitter.** The quantum description of a beam splitter requires two input modes $\hat{a}$, $\hat{b}$ and two output modes $\hat{a}'$, $\hat{b}'$.

Beam splitters may be polarization-dependent, in which case are called *polarizing beam splitters* (PBS). Such devices transmit or reflect the input modes depending on their polarization state, therefore their description requires a four-mode formalism, which takes into account the superposed vertical and horizontal polarization modes in each of the spatial input modes. Since it depends on the ratio between the amplitude of the vertical and horizontal polarization modes in the input modes, a PBS's transmittivity can be tuned by a preceding wave-plate. In the same way, half-wave plates (HWP) and quarter-wave plates (QWP) can be modeled in the same way a PBS is modeled, but with only one spatial input mode. In particular, a HWP is a PBS in which one input port is for the horizontal and the other (spatially superposed) is for the vertical polarization, with the transmittivity being set by the angle between the fast and the slow axis. A QWP is a HWP with an additional phase difference between the two polarization modes.
Finally, we introduce a last two-mode transformation which is used to generate CV entangled states, namely the two-mode squeezing transformation. Such operation involves bilinear mixing of modes and it is generated by the third component of the Eq.(2.25) Hamiltonian, $H \propto g^{(3)}\hat{a}^\dagger\hat{b}^\dagger + h.c.$, corresponding to nondegenerate parametric amplifier dynamics. The evolution operator for the two-mode squeezing interaction reads

$$\hat{S}_2(z) = \mathrm{Exp}\left[z\hat{a}^\dagger\hat{b}^\dagger - z^*\hat{a}\hat{b}\right] , \qquad z = r\mathrm{e}^{2\imath\psi} , \tag{2.52}$$

where r and ψ bear the same meaning as in the single-mode squeezing case, Eq.(2.43). When two-mode squeezing is applied to a two-mode vacuum state $|0\rangle|0\rangle$ the resulting state is commonly known as *two-mode squeezed vacuum*, or equivalently *twin-beam state* (TWB), which can be expressed in the two-mode number basis as

$$\hat{S}_2(z)|0\rangle|0\rangle = \frac{1}{\sqrt{\cosh(r)}} \sum_{n=0}^{\infty} \left(\frac{\mathrm{e}^{2\imath\psi} \sinh(r)}{\cosh(r)} \right)^n |n\rangle|n\rangle \ . \tag{2.53}$$

Being two-mode squeezing an active operation, the photon number in the composite state is not conserved. Yet, it is possible to show that the TWB is an eigenstate of the photon number difference in the tho modes, which is in turn a constant of motion: $\langle \hat{a}^\dagger \hat{a} - \hat{b}^\dagger \hat{b} \rangle_{\hat{\boldsymbol{\rho}}_{2z}} = \langle \hat{a}^\dagger \hat{a} - \hat{b}^\dagger \hat{b} \rangle_{\hat{\boldsymbol{\rho}}_0}$, with $\hat{\boldsymbol{\rho}}_{2z} = \hat{S}_2(z)\, \hat{\boldsymbol{\rho}}_0\, \hat{S}_2^\dagger(z)$.
The entanglement properties of the TWB are easily deduced from its covariance matrix. The symplectic form associated with the unitary operator of Eq.(2.52) reads

$$\hat{S}_{2,z}^{\Gamma} = \begin{pmatrix} \cosh(r) & 0 & -\cos(2\psi)\sinh(r) & \sin(2\psi)\sinh(r) \\ 0 & \cosh(r) & \sin(2\psi)\sinh(r) & \cos(2\psi)\sinh(r) \\ -\cos(2\psi)\sinh(r) & \sin(2\psi)\sinh(r) & \cosh(r) & 0 \\ \sin(2\psi)\sinh(r) & \cos(2\psi)\sinh(r) & 0 & \cosh(r) \end{pmatrix} . \tag{2.54}$$

By applying it to a vacuum covariance matrix as in Eq.(2.26) we obtain the two-mode squeezed vacuum covariance matrix

$$\hat{\boldsymbol{\sigma}}_{2,z} = \begin{pmatrix} \cosh(2r) & 0 & -\sinh(2r) & 0 \\ 0 & \cosh(2r) & 0 & \sinh(2r) \\ -\sinh(2r) & 0 & \cosh(2r) & 0 \\ 0 & \sinh(2r) & 0 & \cosh(2r) \end{pmatrix} . \tag{2.55}$$

The presence of off-diagonal elements suggests the presence of quantum correlations between the two modes. A common property of entangled states is that even though they are overall pure, their subsystems are mixed states when considered separately. Indeed, if one computes the density matrix of the TWB and traces out one of the two modes, the resulting state will be a thermal state with mean photon number $\sinh^2(r)$. This is due to the fact that rather than reducing/amplifying the variance of each quadrature in each of the modes, the two-mode squeezer produces a state in which the variance amplification/reduction is applied to the quadrature combinations $\hat{x}_a \pm \hat{x}_b$ and $\hat{p}_a \pm \hat{p}_b$, where the pedices indicate the mode. More specifically,

$$\mathrm{Var}\left[\hat{x}_b \mp \hat{x}_b\right] = \mathrm{Var}\left[\hat{p}_b \pm \hat{p}_b\right] = \mathrm{e}^{\mp 2r} \ . \tag{2.56}$$

An operational interpretation of the two-mode squeezing operation can be obtained [20] by considering a balanced beam splitter, described by the evolution operator in

Eq.(2.49) with $\kappa = \imath\pi/4$. Applying such transformation to the two-mode squeezed operator leads to

$$\hat{B}_{\imath\pi/4}\hat{S}_2^{\Gamma}(z)\hat{B}_{\imath\pi/4}^{\dagger} = \hat{S}(\frac{\imath\pi}{2}z) \otimes \hat{S}(-\frac{\imath\pi}{2}z) \,, \tag{2.57}$$

where the $\hat{S}(z)$ are single-mode squeezing operators acting on the output modes of the beam splitter. What Eq.(2.57) implies is that a two-mode squeezed state entering a balanced beam splitter is transformed in a factorized state of two single-mode squeezed vacuum states with opposite squeezing phase, and viceversa, two squeezed vacuum states with opposite squeezing phases can be mixed in a balanced beam splitter to produce a TWB entangled state. Indeed, such operation is commonly used to produce CV entanglement, as in [21] and [22].

2.4 Generalized measurements

In order to gain information about a quantum state $\hat{\boldsymbol{\rho}}$, one has to measure some physical quantity that describes it. The most basic quantum mechanical measurement approach is the so-called *projective measurement* (also known as Von Neumann measurement), in which the physical quantity of interest is described by an *observable* $\hat{O}$, which is a Hermitian operator on the Hilbert space of the system under study. The spectral decomposition of $\hat{O}$ reads

$$\hat{O} = \sum_n \lambda_n \hat{P}_n \,, \tag{2.58}$$

where $\hat{P}_n = |\lambda_n\rangle\langle\lambda_n|$ is the projector on the eigenspace associated with the eigenvalue λ_n, which in turn represent the n-th possible outcome of the measurement. The conditions a family of operators $\{\hat{P}_n\}$ must satisfy to be defined as a projector family are

$$\begin{aligned} \hat{P}_n\hat{P}_m &= \delta_{nm}\hat{P}_n \,, \\ \sum_n \hat{P}_n &= \mathbb{I} \,, \\ \hat{P}_n^{\dagger} &= \hat{P}_n \,. \end{aligned} \tag{2.59}$$

Such a family constitutes a *projector valued measure* (PVM), which maps the state $\hat{\boldsymbol{\rho}}$ into the post-measurement state

$$\hat{\boldsymbol{\rho}}_n = \frac{\hat{P}_n\,\hat{\boldsymbol{\rho}}\,\hat{P}_n}{\mathrm{Tr}\left[\hat{P}_n\,\hat{\boldsymbol{\rho}}\,\hat{P}_n\right]} \,, \tag{2.60}$$

associated to the outcome λ_n with probability given by the Born rule

$$P(\lambda_n) = \mathrm{Tr}\left[\hat{P}_n\,\hat{\boldsymbol{\rho}}\,\hat{P}_n\right] . \tag{2.61}$$

A more general approach to the problem of measurement consists in expressing the measurement not as a PVM, but as a *Positive Operator Valued Measure* (POVM) [23, 24]. A POVM is a collection of Hilbert space operators $\{\hat{\Pi}_n\}$ which satisfy the less restrictive conditions

$$\begin{aligned} \sum_n \hat{\Pi}_n &= \mathbb{I}\,, \\ \hat{\Pi}_n &\geq 0\,. \end{aligned} \tag{2.62}$$

A POVM therefore is a map that associates an element of $\{\hat{\Pi}_n\}$ to every possible outcome of the measurement, just as in the PVM formalism one associates to each eigenvalue of an Hermitian operator a projector on the eigenspace. Just like in the PVM formalism, we can define the probability of obtaining the outcome λ_n as

$$P(\lambda_n) = \mathrm{Tr}\left[\hat{\boldsymbol{\rho}}\,\hat{\Pi}_n\right] . \tag{2.63}$$

The relationship between PVMs and POVMs becomes clear through Neumark's theorem [12], which states that a POVM can always be realized by extending the Hilbert space to a larger space and performing a projective measurement on the latter. While quantum mechanic postulates are valid as far as the system is isolated, the projectors invoked in such postulates are defined on Hilbert spaces bigger than those of the actual physical system, because they include the measurement apparatus too. When we trace out the degrees of freedom of the measurement apparatus, thus considering only its preparation, the mathematical object describing the measurement statistics in therms of the physical state under measurement is in general a POVM.

Chapter 3

Quantum metrology

In this chapter we introduce the framework of quantum metrology, which is the field of physics that studies how quantum technologies can be used to improve the performances of classical metrological tasks [2]. We start by introducing the problem of the phase operator, which is the reason one has to resort to estimation strategies. We then move to the theory of quantum parameter estimation, which provides the framework to design parameter estimation experiments which are inherently optimal. Afterwards, we introduce a proposal for an *ab initio*, deterministic, real-time adaptive phase estimation protocol based on squeezed probes, homodyne detection and Bayesian estimation. We show how the optimality of such protocol is reduced in the case of unavoidable thermal noise in the probe states, and we derive the expected scaling of the estimation variance. We describe the experimental implementation of the estimation protocol focusing on both the experimental apparatus, the procedure and the data processing, concluding with a survey of the results.

3.1 The quantum phase operator

Since the groundbreaking work of Dirac on quantum electrodynamics [25], the measurement of a phase shift has been a widely debated subject in quantum mechanics. In the quantum world a phase measurement cannot be described properly, as no proper quantum observable can be associated to the classical one. Indeed, one might be tempted to just assume the existence of a phase observable $\hat{\phi}$ canonically conjugate to the number operator $\hat{n}$. Unfortunately in such case the canonical

commutation relation $[\hat{n}, \hat{\phi}] = \imath\hbar$ would lead to a contradiction when expanded in the Fock basis, as

$$\langle n'|[\hat{n}, \hat{\phi}]|n\rangle = \imath\hbar\delta_{n,n'} \Rightarrow (n' - n)\langle n'|\hat{\phi}|n\rangle = \imath\hbar\delta_{n,n'} \,, \tag{3.1}$$

yielding $\imath\hbar = 0$ when $n = n'$ [26]. The same line of argument could be applied to position and momentum operators, but the difference here is that while the quadrature operators have a continuous and unbounded spectrum, the phase angle has a 2π periodicity and the number operator has a discrete and bounded-from-below spectrum. These properties of the quantum phase and the number operator are precisely the reason why it's not possible to define an Hermitian phase operator by simple translation from the classical world to the quantum domain [27, 28]. Since the seminal work of Dirac numerous attempts to redefine a phase operator have been made. Among these, a special place is occupied by the exponential phase operator proposed by Susskind and Glogower [29], which takes the form $\hat{e^{\imath\phi}} = \sum_{n=0}^{\infty} |n\rangle\langle n+1|$. Such operator is not unitary, it doesn't explicitly involve a phase operator $\hat{\phi}$, and the solution to the eigenvalue problem $\hat{e^{\imath\phi}}|\phi\rangle = e^{\imath\phi}|\phi\rangle$ leads to canonical phase distributions which don't represent a properly defined probability for a phase observable. Nevertheless, such phase distributions can be measured experimentally [30]. Another noteworthy approach is the one based on the definition of an Hermitian phase operators by Barnett and Pegg, obtained from Susskind and Glogower's exponential phase operator by extending the Fock eigenbasis to negative, unphysical number states [31].

If it was possible to perform a canonical phase measurement, its sensitivity would only be limited by the intrinsic quantum uncertainty of the phase [32], which is non-zero for any quantum state of finite energy. Given the absence of such a measurement, the most commonly adopted strategy for extracting phase information from a physical process is to consider the quantum phase an evolution parameter, thereby separating the measurement operators from the estimator function, and use the results provided by quantum estimation theory (QET, cfr. Sec.3.3) to devise a proper estimation scheme depending on the probe states and the detection strategy. This approach automatically adds another layer of uncertainty to the intrinsic phase undeterminacy of the probe states, due to the finite sensitivity of the detection apparatus. Eventually, one last layer of uncertainty is introduced in a realistic phase estimation strategy, in which the probe states and the detection apparatus are subject to various noise sources.

3.2 Estimating the quantum phase

The value of a phase shift is a relative quantity, *i.e.* it depends on a reference phase. Depending on the range of variation of the phase with respect to the reference two different scenarios can be identified: *phase sensing* and *ab initio* phase estimation. Both problems are naturally associated with interferometric devices. An interferometer accumulates a phase difference between its arms which is related to one or more physical parameters of interest. At the classical level, such accumulated phase can be deduced from the intensity fringes at the output of the interferometer. The precision of such deduction is in general dependent on the visibility of the interference fringes (*i.e.* contrast), which in turn depends on the coherence properties and the matching (*i.e.* overlap) of the interfering light modes, but from a purely classical point of view the light intensity can be measured with arbitrary precision, therefore no fundamental uncertainty on the phase estimate can be derived. To deduce fundamental limitations on the precision of phase estimation one has to consider a semi-classical approach, in which the detection process is quantized and the absorption of the individual photons in the detector is described as a stochastic process depending on the noise properties of detected photons. As showed in Eq.(2.37) coherent states follow a Poissonian statistic, therefore they provide a phase uncertainty $\Delta\phi \propto \Delta N/\langle N\rangle = 1/\sqrt{N}$, or equivalently an estimation variance

$$\mathrm{Var}\,[\phi] \propto \frac{1}{N}\,, \tag{3.2}$$

where N is the number of resources used in the estimation, or more generally the number of interactions between the probe and the system to be measured. Such scaling is known as the *standard quantum limit* (SQL) or *shot noise limit* (SN), and it is the same scaling that one obtains when averaging the results of N independent measurements as a consequence of the central limit theorem. Indeed, the two scalings are deeply connected since they are both the result of classical statistical correlations between the N resources. The SQL is also known as a *classical limit*, *i.e.* , the minimum uncertainty scaling that is achievable using only classical resources.

Such limit can be achieved in phase sensing applications by performing an intensity measurement on coherent states locked mid-fringe (*i.e.* where the intensity curve is steepest), since that corresponds to measuring on the high sensitivity region. If the expected phase shift is small the resulting estimation sensitivity will be limited by the standard quantum limit. In order to beat such scaling one might

consider using probe states characterized by Sub-Poissonian statistics, as is the case of single-mode squeezed states, as we showed in Eq.(2.46). As initially proposed by Caves [33], when single-mode squeezed vacuum states are used at one of the input port of a Mach-Zehnder interferometer in juction with coherent states on the other input port, one might beat the SQL and achieve a sub-SQL scaling of the order $\Delta\phi \propto 1/N^{2/3}$. This kind of strategy is used, for instance, in the LIGO gravitational wave detector [34, 35]. Scalings of the order $\Delta\phi \propto 1/N^{3/4}$ [36], or even $\Delta\phi \propto 1/N$ [37] (the so-called *Heisenberg limit*, HL) are also possible using the same probe states but optimizing the measurement strategy and the chosen estimator. Another common approach for sub-SQL sensitivity in phase sensing calls for the use of entangled states [38, 39], ranging from the exotic NOON states [40, 41] which may allow Heisenberg scaling, to two-mode squeezed states [42]. The achievability of the above mentioned scalings however is often conditioned on the detection scheme and to the actual value of the parameter to be estimated.

Ab initio phase estimation can be considered as a general problem of which phase sensing is a special case. Indeed, if no assumptions can be made on the deviation of the phase from the reference, measuring with optimal sensitivity is not possible. Dyne techniques are historically considered the standard strategies in this case [11]. Dyne techniques are based on either double-quadrature (heterodyne) or single-quadrature (homodyne) measurement. In particular heterodyning [43] occupies a special place in phase detection and the so called *heterodyne limit* has been traditionally considered the standard benchmark for *ab initio* phase estimation. However, while heterodyne sensitivity does not depend on the value of the phase [44], thus not requiring *a priori* knowledge of the magnitude of the phase shift, it does suffer from the additional noise introduced by the joint measurement of the conjugate quadratures [45]. On the other hand, homodyning is known for its ability to approach the standard quantum limit for pure states [46] when used in an adaptive fashion. As a matter of fact, a feedback strategy is conceptually required when using homodyne detection, since its sensitivity depends on the actual value of the phase [47, 48, 49, 50].

As we will see in Sec.3.3, quantum estimation theory provides the means to calculate quantitative ultimate bounds on the precision of phase estimation which are completely general and only depend on the probing resource, while no assumptions are required on the detection strategy or the required estimator.

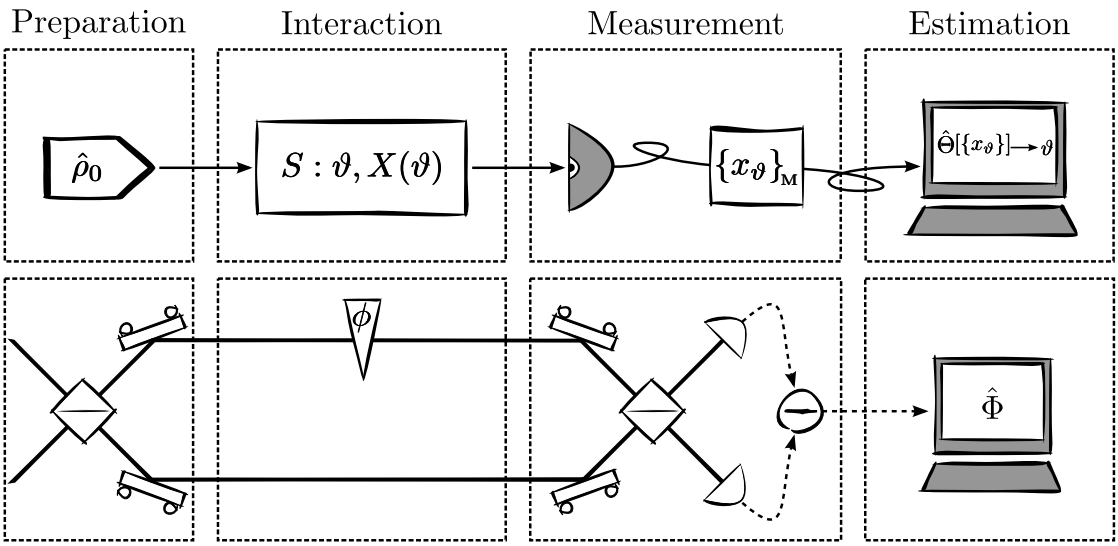

Figure 3.1: **Schematic representation of an estimation procedure.** Top: generic parameter estimation procedure. Bottom: application to a interferometric strategy for the estimation of a phase shift.

3.3 Quantum estimation theory

Some times direct measurement of a physical quantity is not possible, either because of experimental issues or because of theoretical restrictions, as is the case with the amplitude of an electromagnetic field or with the quantum phase. Let's suppose, for instance, that we need to know the value ϑ of a quantity that describes a physical system or a dynamical process S, but we have no means of measuring it directly. In such case we shall find another quantity, this time accessible for direct measurement, that depends on the value of our parameter of interest, let's say $X(\vartheta)$. This allows us to *estimate* the value ϑ from measurement of X. Any estimation process can be divided in four distinct stages (see Fig.3.1): a probe is prepared in a known state $\hat{\boldsymbol{\rho}}_0$; the probe evolves into $\hat{\boldsymbol{\rho}}_\vartheta$ through interaction with the system S; the quantity $X(\vartheta)$ is measured on the evolved probe, yielding the outcome x_ϑ; the value of the parameter ϑ is inferred through an estimator $\hat{\Theta}[\{x_\vartheta\}]$. In general such process is afflicted by statistical or systematic errors, and the common strategy to reduce the former is to repeat the measurement on a large number M of independent probe states. An estimator is defined as a mapping $\hat{\Theta} = \hat{\Theta}[\{x_\vartheta\}_{\mathrm{M}}]$ from the space of measurement outcomes into the space of parameters (possible values of ϑ). An estimator is called unbiased if its expectation values

satisfies

$$\mathcal{E}_\vartheta[\hat{\Theta}] = \int \hat{\Theta}(x) P(x|\vartheta) \mathrm{d}x = \vartheta \,, \tag{3.3}$$

where $P(x|\vartheta)$ is the conditional probability of finding the outcome x when the value of the parameter is ϑ. An example of unbiased estimator is the mean value of a distribution, while the mode of a distribution is an example of a biased estimator. An important result of classical estimation theory [51] is the so-called Cramér-Rao inequality (CCR), which poses a lower bound on the variance of any unbiased estimator as

$$\mathrm{Var}\left[\hat{\Theta}\right] \geq \frac{1}{MF(\vartheta)} \,, \tag{3.4}$$

where $F(\vartheta)$ is the *Fisher Information* (FI), defined as

$$F(\vartheta) = \int P(x|\vartheta) \left(\frac{\partial \log\left[P(x|\vartheta)\right]}{\partial \vartheta} \right)^2 . \tag{3.5}$$

The fact that the FI depends on the value of the parameter itself can be understood in terms of the signal-to-noise ratio (SNR), in that a FI not dependent on ϑ would require a detection strategy in which the signal to noise ratio is constant. In order to obtain a quantum version of the Cramér-Rao bound and of the Fisher information, let us consider a family of quantum states $\hat{\boldsymbol{\rho}}_\vartheta$ labeled by a parameter ϑ we need to estimate. From the postulates of quantum mechanics we know that the Born rule holds, $P(x|\vartheta) = \mathrm{Tr}\left[\hat{\boldsymbol{\rho}}_\vartheta \hat{\Pi}_x\right]$, where $\hat{\Pi}_x$ are the elements of a general POVM describing the measurement of $\hat{\boldsymbol{\rho}}_\vartheta$. We introduce the *Symmetric Logarithmic Derivative* (SLD), a noncommutative self-adjoint operator defined by

$$\frac{1}{2}\left(\hat{\Lambda}_\vartheta \hat{\boldsymbol{\rho}}_\vartheta + \hat{\boldsymbol{\rho}}_\vartheta \hat{\Lambda}_\vartheta\right) = \partial_\vartheta \hat{\boldsymbol{\rho}}_\vartheta \,. \tag{3.6}$$

Using the SLD and the Born rule we can rewrite the FI in Eq.(3.5) as

$$F(\vartheta) = \int \frac{\mathfrak{Re}\left[\mathrm{Tr}\left[\hat{\boldsymbol{\rho}}_\vartheta \hat{\Pi}_x \hat{\Lambda}_\vartheta\right]\right]^2}{\mathrm{Tr}\left[\hat{\boldsymbol{\rho}}_\vartheta \hat{\Pi}_x\right]} \mathrm{d}x \,. \tag{3.7}$$

It can be shown [52] that the following chain of inequalities holds:

$$F(\vartheta) \leq \int \left| \frac{\mathrm{Tr}\left[\hat{\boldsymbol{\rho}}_\vartheta \hat{\Pi}_x \hat{\Lambda}_\vartheta\right]}{\sqrt{\mathrm{Tr}\left[\hat{\boldsymbol{\rho}}_\vartheta \hat{\Pi}_x\right]}} \right|^2 \mathrm{d}x \leq \int \mathrm{Tr}\left[\hat{\Pi}_x \hat{\Lambda}_\vartheta \hat{\boldsymbol{\rho}}_\vartheta \hat{\Lambda}_\vartheta\right] \mathrm{d}x = \tag{3.8}$$

$$= \mathrm{Tr}\left[\hat{\boldsymbol{\rho}}_\vartheta \hat{\Lambda}_\vartheta^2\right] = H(\vartheta) \,, \tag{3.9}$$

resulting in a bound for the Fisher information of any quantum measurement, defined by the *quantum Fisher information* (QFI)

$$H(\vartheta) = \mathrm{Tr}\left[\hat{\boldsymbol{\rho}}_\vartheta \, \hat{\Lambda}_\vartheta^2\right] . \tag{3.10}$$

A comparison of the definition of the QFI with the FI suggests the important difference between the two quantities: while the latter quantifies the amount of information on ϑ that one can extract from the state $\hat{\boldsymbol{\rho}}_\vartheta$ by means of a certain POVM, the former represents the overall amount of information on ϑ carried by $\hat{\boldsymbol{\rho}}_\vartheta$, regardless of the measurement strategy we adopt to extract such information. The QFI allows to derive a stricter bound on the variance of an unbiased estimator,

$$\mathrm{Var}\left[\hat{\Theta}\right] \geq \frac{1}{MH(\vartheta)} , \tag{3.11}$$

known as the *quantum Cramér-Rao bound* (QCR), which provides the ultimate limit imposed by quantum mechanics on the variance of any unbiased estimator. It's worth noting that the QCR holds for all possible POVMs and it only depends on the measured quantum state, *i.e.* on the geometrical structure of the quantum statistical model of the physical system under study. Moreover, in the asymptotic limit of a large number of independent probe states $M \gg 1$, the QCR bound is always achievable by means of local measurements and adaptive estimators, which means LOCC strategies are enough and one doesn't need entanglement at the measurement stage [53].
We will deal with the application of the Cramér-Rao bounds and the Fisher information formalism to the specific case of phase estimation in Sec.3.4.1 and Sec.3.4.2.

3.4 Deterministic squeezing-enhanced phase estimation using real-time feedback

In this section we present our experimental investigation of an adaptive phase estimation protocol which delivers a real-time, *ab initio*, deterministic estimation of a phase shift under the realistic assumption of thermalization of the probe states. The protocol we refer to [46, 54] uses squeezed vacuum probes and adaptive homodyne detection with Bayesian inference to estimate an unknown phase in the $[0, \pi/2)$ range. A proposal to extend the available estimation range to $[0, \pi)$ will be given with the concluding remarks. The estimation scheme is tailored to saturate

the Cramér-Rao and the quantum Cramér-Rao bounds, therefore the achievable estimation variance is fully and quantitatively determined.

3.4.1 Pure state scenario

As explained in Sec.3.3, any estimation scheme revolves around four main stages: the preparation of a probe state, its interaction with the system, the measurement, and finally the estimation. As we will show in the following, each one of these stages can be optimized in order to saturate the Cramér-Rao bounds, apart from the interaction stage, which is somewhat fixed once we choose an measuring device. We start by following the line of argument found in references [46, 54], where the authors devise a phase estimation scheme that uses pure squeezed states, homodyne detection and Bayesian inference to achieve the quantum Cramér-Rao limit. Afterwards, we will drop the assumption of purity of the probe states to consider a realistic implementation where we assume unavoidable thermalization of the probe states.
We start by reprising the Cramér-Rao chain of inequalities, Eq.(3.4) and Eq.(3.11), which we will update as we proceed with the optimization procedure

$$\mathrm{Var}\left[\hat{\phi}\right] \overset{CCR}{\geq} \frac{1}{MF(\phi)} \overset{QCR}{\geq} \frac{1}{MH}\,. \tag{3.12}$$

As a first step, we restrict our search for the optimal probe state in the class of Gaussian states. As we briefly mentioned in Sec.2.3, Gaussian states are a favourite class in quantum optical applications due to their simple generation and handling, their relative robustness against noise and their simple mathematical description. The squeezing angle doesn't play much of a role in the following, since it can always be changed by applying another unitary phase transformation. To keep the treatment simple, in the following we will consider amplitude-squeezed states, therefore setting $\psi = 0$. The most general pure Gaussian state is a displaced squeezed state, described by the density matrix $\hat{\boldsymbol{\rho}}_{\alpha,z} = \hat{D}(\alpha)\hat{S}(z)|0\rangle\langle 0|\hat{S}(z)^\dagger\hat{D}(\alpha)^\dagger$, where $\hat{D}(\alpha)$ is the displacement operator from Eq.(2.34) and $\hat{S}(z)$ is the squeezing operator, Eq.(2.43). For a pure state evolving under a unitary transformation in a closed system, the quantum Fisher information can be explicitly calculated as [55] (cfr. Appendix A)

$$H_{\text{pure}} = 4\Delta\hat{G}^2\,, \tag{3.13}$$

where G is the generator of the unitary transformation and $\Delta G^2 = \langle G^2 \rangle - \langle G \rangle^2$ its fluctuations. In the specific case of a displaced, squeezed state undergoing a unitary phase shift described by the generator $G = \hat{n}$ we obtain

$$H_{\alpha,z} = 4\left(|\alpha|^2(\mu^2 + |\nu|^2) + \alpha^2\mu\nu^* + \alpha^{*2}\mu\nu + 2\mu^2|\nu|^2\right) , \tag{3.14}$$

where $\mu = \cosh(r)$ and $\nu = \mathrm{e}^{2\imath\psi}\sinh(r)$. The probe state that can carry the most phase information is the one with maximum QFI, for which the quantum Cramér-Rao bound is minimized. The QFI could be maximized by just increasing the displacement or the squeezing parameter at will, but the most efficient approach here is to use a Lagrange multipliers technique to maximixe the QFI for varying displacement and squeezing strength with the constraint of constant probe state energy, which in the case of a displaced, squeezed state is $\langle \hat{n} \rangle_{\alpha,z} = |\alpha|^2 + \sinh^2(r)$. In this way we find which resource gives the highest probe energy to fluctuations ratio, finding that the optimal probe state is a squeezed vacuum for which the QFI reads

$$H_{0,z} = 2\sinh^2(2r) = 8\langle n \rangle_{0,z} + 8\langle n \rangle_{0,z}^2 , \tag{3.15}$$

where $\langle n \rangle_{0,z} = \sinh^2(r)$ is the mean number of squeezed photons in a squeezed vacuum state, as in Eq.(2.46). The Cramér-Rao inequalities of Eq.(3.12) now read

$$\mathrm{Var}\left[\hat{\phi}\right] \overset{CCR}{\geq} \frac{1}{MF(\phi)} \overset{QCR}{\geq} \frac{1}{MH_{0,z}} . \tag{3.16}$$

As a second step in the optimization we may choose a detection strategy. Among all detection schemes aiming at phase estimation, homodyne detection has been shown to achieve the Cramér-Rao bound using coherent states [56] and to achieve the quantum Cramér-Rao bound using squeezed vacuum probes [46]. Homodyning on a certain quadrature in phase space yields samples distributed according to the state's Wigner function marginal distribution along the same direction. In the case of a pure, phase shifted amplitude-squeezed state, the homodyne probability distribution for the x quadrature can be calculated by integrating the Wigner function along the p direction. The Wigner function can be calculated from Eq.(2.23) using the covariance matrix of a general phase shifted amplitude-squeezed vacuum state

$$W[\hat{\boldsymbol{\rho}}_{0,z}](x,p) = \frac{1}{2\pi}\mathrm{e}^{\frac{1}{2}\left[-(x^2+p^2)\cosh(2r)+\left((p^2-x^2)\cos(2\phi)+2px\sin(2\phi)\right)\sinh(2r)\right]} , \tag{3.17}$$

where ϕ is the applied phase shift. The probability distribution for homodyning along the x direction on such state is therefore

$$\begin{aligned} P(x|\phi) &= \int_{\mathbb{R}} W\left[\hat{\boldsymbol{\rho}}_{0,z}\right](x,p)\mathrm{d}p = \\ &= \frac{1}{2\pi}\mathrm{Exp}\left[-\frac{1}{2}(\cos(2\phi)\sinh(2r)+\cosh(2r))x^2\right]\cdot \\ &\cdot\int_{\mathbb{R}}\mathrm{Exp}\left[\frac{1}{2}(\cos(2\phi)\sinh(2r)-\cosh(2r))p^2+px\sin(2\phi)\sinh(2r)\right]\mathrm{d}p = \\ &= \frac{1}{\sqrt{2\pi\sigma_{0,z}}}\mathrm{Exp}\left[-\frac{x^2}{2\sigma_{0,z}}\right], \end{aligned} \tag{3.18}$$

where $\sigma_{0,z} = \left(\mathrm{e}^{-2r}\cos^2(\phi)+\mathrm{e}^{2r}\sin^2(\phi)\right)$ is the first diagonal element of the state's covariance matrix. It is noteworthy that the marginal distribution for a squeezed vacuum state have a π periodicity and are symmetric around $\phi = \pi/2$. As a consequence, homodyne detection of squeezed vacuum states cannot discriminate between the four quadrants in phase space. For this reason we have to restrict the range of input phases in the $[0,\pi/2)$ window.
Calculation of the Fisher information for homodyne detection on squeezed vacuum probes can be performed explicitly (see Appendix B), yielding the expression

$$F_{0,z}(\phi) = \frac{2\sinh^2(2r)\sin^2(2\phi)}{\left(\mathrm{e}^{-2r}\cos^2(\phi)+\mathrm{e}^{2r}\sin^2(\phi)\right)^2}\,. \tag{3.19}$$

Since the FI represents the amount of phase information we can extract from our squeezed vacuum probes by means of homodyning, the optimization of the detection strategy can be accomplished by maximizing the FI. This procedure leads to two equivalent expressions:

$$\begin{aligned} \phi_{\mathrm{opt}}^{\mathrm{th}} &= \frac{1}{2}\arccos(\tanh(2r))\,, \\ r_{\mathrm{opt}}^{\mathrm{th}} &= -\frac{1}{2}\log\left[\tan(\phi)\right]\,. \end{aligned} \tag{3.20}$$

Remarkably, such optimality curves not only define the maximum Fisher information, but actually define the values of r and ϕ that solve the equation $F_{0,z}(\phi) = H_{0,z}$, therefore saturating the quantum Cramér-Rao inequality (see Fig.3.2). The fact that we may be able to maximize the homodyning sensitivity upon a specific choice of the squeezing strength (dependent on the value of the phase to be estimated) or of the phase to be estimated (dependent on the squeezing strength) suggest that an adaptive strategy may be implemented. Both approaches would

require a first, rough homodyning in order to either tune the homodyning phase or the squeezing strength to match the first or the second expression in Eq.(3.20), respectively. As a matter of fact, tuning the squeezing strength in an real-time fashion might be a challenging task, therefore we will focus on the first approach. The Cramér-Rao inequalities of Eq.(3.16) therefore become

$$\mathrm{Var}\left[\hat{\phi}\right] \overset{CCR}{\geq} \frac{1}{MF_{0,z}(\phi^{\mathrm{th}}_{\mathrm{opt}})} \overset{QCR}{=} \frac{1}{MH_{0,z}}\,, \tag{3.21}$$

where the last inequality is now saturated, provided a successful implementation of the aforementioned adaptive detection strategy.

We are now left with the task of saturating the first Cramér-Rao inequality by choosing an appropriate estimator. Among the possible choices, the maximum likelihood and the Bayes estimators occupy a special place due to their asymptotic properties [24]. In particular, we focus on the Bayes estimator, that has been shown to asymptotically saturate the Cramér-Rao inequality in Eq.(3.4) [57]. Bayesian estimation exploits the Bayes theorem to infer the value of a quantity from the probability that such value is obtained, conditioned to the measured data set [24]. In the case of interest, in which we want to infer the value of a phase shift ϕ given the measured homodyne data, the Bayes theorem can be used to derive an expression for the *posterior* probability distribution (PPD) of the phase ϕ conditioned to the observed data set $\{x\}_{\mathrm{M}}$:

$$P(\{x\}_{\mathrm{M}}|\phi)P(\phi) = P(\phi|\{x\}_{\mathrm{M}})P(\{x\}_{\mathrm{M}}) \rightarrow P(\phi|\{x\}_{\mathrm{M}}) = \frac{1}{\mathcal{N}}\prod_{k=1}^{M} P(x_k|\phi)\,, \tag{3.22}$$

where the assumption of no *a priori* information on the value of ϕ was made, thus setting $P(\phi) = 2/\pi$, and $\mathcal{N} = \int_0^{\pi/2} P(\phi|\{x\}_{\mathrm{M}})\mathrm{d}\phi$ is a normalization factor. Substitution of the conditional probability in the above expression with the homodyne probability distribution in Eq.(3.18), and the assumption of a large number of samples, $M \gg 1$ [54], lead to the final expression (detailed calculation is provided in Appendix C):

$$P(\phi|\{x\}_{\mathrm{M}}) = \frac{1}{\mathcal{N}}\frac{1}{(2\pi\sigma_{0,z}(\phi))^{M/2}}\mathrm{Exp}\left[-\frac{M\sigma_{0,z}(\phi^*)}{2\sigma_{0,z}(\phi)}\right]\,, \tag{3.23}$$

where $\sigma_{0,z}(\phi)$ is the variance of the $\hat{x}$ quadrature for a squeezed vacuum state, derived from the application of the phase shift symplectic transformation of Eq.(2.42) to the amplitude-squeezed vacuum covariance matrix, and ϕ^* is the actual, unknown value of the phase shift. As it is apparent from Fig.3.3, where we simulate

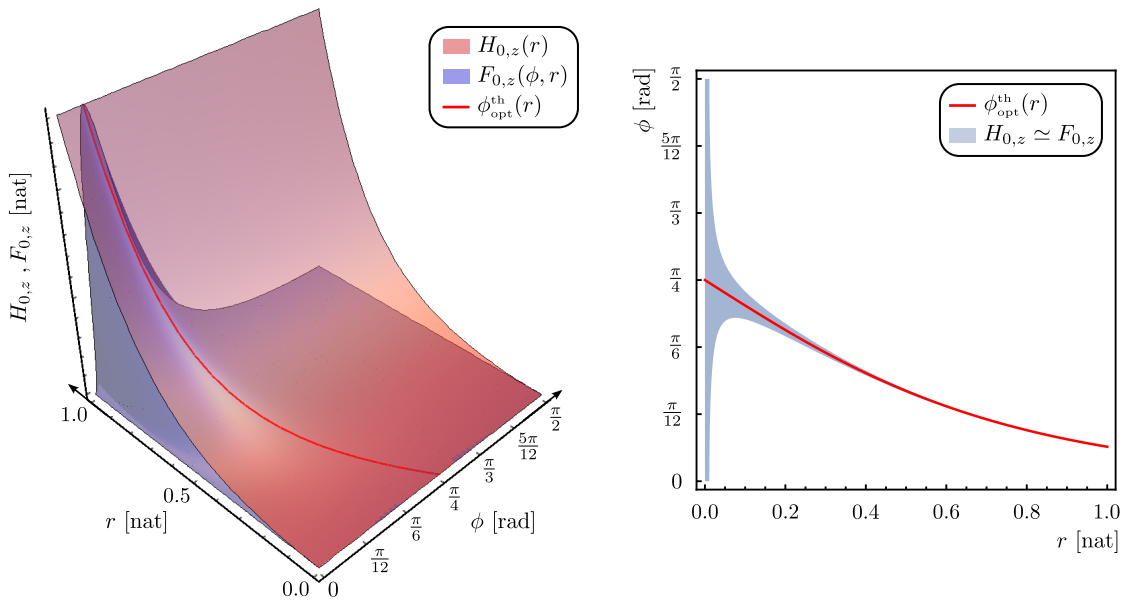

Figure 3.2: **Maximizing the Fisher information.** Left: Here we show the FI (blue) and the QFI (red) surfaces versus the input phase and the squeezing parameter for a pure squeezed vacuum state. The region in which $H_{0,z} = F_{0,z}$ is highligthed as a red curve which is defined by the optimal values in Eq.(3.20). Right: Here we plot the optimal phase of Eq.(3.20) as a function of the squeezing parameter (red curve). It is noteworthy that, as the squeezing parameter decreases, the optimal phase loses significance, an effect exemplified by the expansion of the shaded area (which represents $H_{0,z} - F_{0,z} \leq 10^{-3}$) to cover the whole phase domain as r goes to 0.

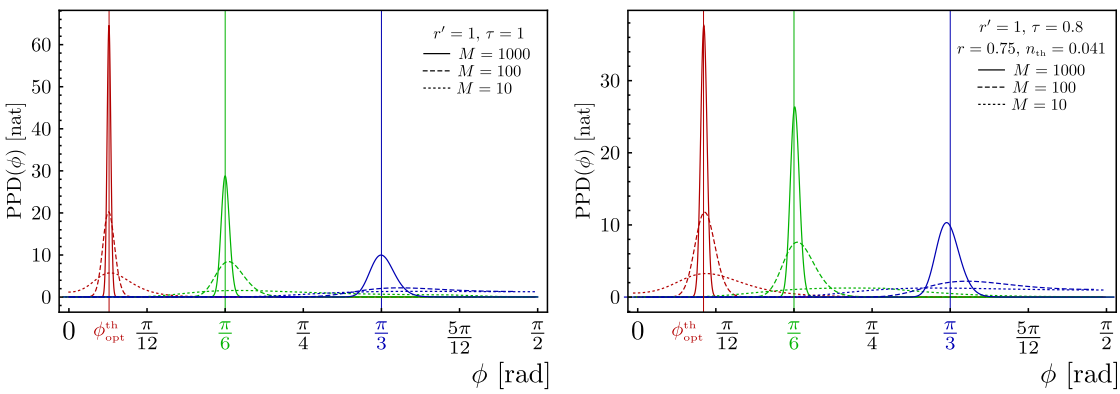

Figure 3.3: **Posterior probability distributions.** Here we show PPDs for different input phases and different number of homodyne samples. The homodyne samples are simulated by drawing M samples from a normal distribution centered on 0 (since we are dealing with squeezed vacuum/thermal probes) and with variance given by the first diagonal element of the squeezed thermal state covariance matrix, Eq.(3.36).
Left: pure probe scenario, with the original squeezing parameter $r' = 1$ and no losses, $\tau = 1$ (therefore $r = 1$ and $\mathrm{n_{th}} = 0$). Right: thermal scenario, with the original state described by a squeezing parameter $r' = 1$ and beam splitter transmissivity $\tau = 0.8$, which imply a probe state with an efficient squeezing strength $r \simeq 0.75$ and thermalization $\mathrm{n_{th}} \simeq 0.041$ (see Sec.3.4.2).
In both scenarios we simulate the homodyne samples around three input phases: the optimal phase $\phi^* = \phi^{\mathrm{th}}_{\mathrm{opt}}$ (red), $\phi^* = \pi/6$ (green) and $\phi^* = \pi/3$ (blue).
Two effects can be noticed: the PPDs obtained with small numbers of samples are fairly asymmetric, therefore the estimation may be obtained as their mode. As the number of samples increases, the resulting PPDs become more peaked, with the mode converging to the mean value, as expected in a Gaussian distribution. As a second effect we can notice that as the input phase goes further away from the optimal phase, the resulting PPDs become less and less peaked, as expected from the fact that the range of validity of the Gaussian approximation decreases as the distance between ϕ^* and $\phi^{\mathrm{th}}_{\mathrm{opt}}$ increases [54]. Thermalization (losses) in the probe state also contibutes to the decrease of the PPD variances and the validity of the Gaussian approximation.

posterior probability distributions for different values of M, r and ϕ^*, for small values of M the distributions are highly asymmetric, therefore the most effective estimator for ϕ^* may be given by the maximum of the PPDs, *i.e.* their mode. Nevertheless, as the number of measurement increases, the mode converges to the mean value, and we can approximate Eq.(3.23) with a Gaussian distribution centered on ϕ^* and with a variance that, remarkably, takes the form [58]

$$\sigma_G = \frac{1}{MF_{0,z}(\phi^*)}\,, \tag{3.24}$$

which is exactly the Cramér-Rao variance of Eq.(3.4). The asymptotic normality of the PPD [59] therefore guarantees that the Bayes estimator is asymptotically unbiased and efficient, therefore saturating the first Cramér-Rao inequality.

In conclusion, the choice of squeezed vacuum states ensures that the maximum phase information is encoded into the probe states (maximum QFI, $H_{0,z}$), adaptive homodyne detection provides the highest homodyning sensitivity (maximum FI, $F_{0,z}(\phi^{\text{th}}_{\text{opt}})$), and Bayesian estimation guarantees a final PPD that delivers the estimation of the true phase ϕ^* with Cramér-Rao variance. Overall, the Cramér-Rao inequalities chain becomes

$$\text{Var}\left[\hat{\phi}\right] \overset{CCR}{=} \frac{1}{MF_{0,z}(\phi^{\text{th}}_{\text{opt}})} \overset{QCR}{=} \frac{1}{MH_{0,z}}\,, \tag{3.25}$$

where we can see that the ultimate limit on the variance of the estimation is achieved.

3.4.2 Thermal state scenario

We may now proceed by dropping the assumption of purity of the probe states. Since most sources of noise in quantum optical experiments can be cast in terms of linear losses, we can model our mixed squeezed probes as the transmitted output of a beam splitter of transmissivity τ whose inputs are a squeezed vacuum and a vacuum state. Such state can be described by the density matrix transformation $\hat{\boldsymbol{\rho}}_{0,z'} \otimes \hat{\boldsymbol{\rho}}_0 \to \hat{B}^{\mathcal{H}}_{\kappa}\, \hat{\boldsymbol{\rho}}_{0,z'} \otimes \hat{\boldsymbol{\rho}}_0\, \hat{B}^{\mathcal{H}\dagger}_{\kappa}$, where the beam splitter transformation was given in Eq.(2.50). Equivalently, in the symplectic formalism the output modes of the

beam splitter are described by the covariance matrix:

$$\hat{\boldsymbol{\sigma}}_{\tau,z'} = \hat{B}^{\Gamma}_{\kappa}\,\hat{\boldsymbol{\sigma}}_{0,z'} \oplus \hat{\boldsymbol{\sigma}}_{0}\,\hat{B}^{\Gamma T}_{\kappa} = \\ = \begin{pmatrix} \tau \mathrm{e}^{-2r'}+\rho & 0 & 0 & -2\sqrt{\tau\rho}\sinh(r')\mathrm{e}^{-r'} \\ 0 & \tau \mathrm{e}^{2r'}+\rho & \sqrt{\tau\rho}(1-\mathrm{e}^{2r'}) & 0 \\ 0 & \sqrt{\tau\rho}(1-\mathrm{e}^{2r'}) & \rho \mathrm{e}^{2r'}+\tau & 0 \\ -2\sqrt{\tau\rho}\sinh(r')\mathrm{e}^{-r'} & 0 & 0 & \rho \mathrm{e}^{-2r'}+\tau \end{pmatrix}, \tag{3.26}$$

where τ is the beam splitter's transmissivity, $\rho = 1-\tau$ its reflectivity and the symplectic form of the beam splitter transformation was given in Eq.(2.51). We may now trace out the reflected mode, obtaining our model covariance matrix for the lossy squeezed vacuum probe:

$$\hat{\boldsymbol{\sigma}}_{\mathrm{loss},z'} = \begin{pmatrix} \tau \mathrm{e}^{-2r'}+\rho & 0 \\ 0 & \tau \mathrm{e}^{2r'}+\rho \end{pmatrix}. \tag{3.27}$$

In turn, such state can be remodeled as a thermal squeezed state defined by the parameters:

$$\mathrm{n}_{\mathrm{th}} = \frac{\sqrt{\tau^2+2\tau\rho\cosh 2r'+\rho^2}-1}{2} \\ r = \frac{1}{4}\log\left[\frac{\mathrm{e}^{2r'}\tau+\rho}{\mathrm{e}^{-2r'}\tau+\rho}\right]. \tag{3.28}$$

Therefore we will proceed in the treatment assuming our probe states as phase shifted thermal squeezed states, described by the density matrix

$$\hat{\boldsymbol{\rho}}_{\mathrm{th},z,\alpha} = \sum_n \nu_n \hat{U}(\phi)\hat{S}(z)|n\rangle\langle n|\hat{S}(z)^{\dagger}\hat{U}(\phi)^{\dagger} \tag{3.29}$$

or, equivalently by the covariance matrix

$$\hat{\boldsymbol{\sigma}}_{\mathrm{th},z,\phi} = \hat{U}^{\Gamma}_{\phi}\hat{S}^{\Gamma}_{z}\,\hat{\boldsymbol{\sigma}}_{\mathrm{th}}(\hat{S}^{\Gamma}_{z})^{T}(\hat{U}^{\Gamma}_{\phi})^{T} = \\ = (2\,\mathrm{n}_{\mathrm{th}}+1)\begin{pmatrix} e^{-2r}\cos^2(\phi)+e^{2r}\sin^2(\phi) & \sin(2\phi)\sinh(2r) \\ \sin(2\phi)\sinh(2r) & e^{2r}\cos^2(\phi)+e^{-2r}\sin^2(\phi) \end{pmatrix}. \tag{3.30}$$

Since such state is mixed, we cannot use the result in Eq.(3.13) to obtain an expression for the quantum Fisher information, which has to be calculated from the definition in Eq.(3.10). The derivation of the QFI (the complete derivation can be found in Appendix A) yields

$$H_{\mathrm{th},z}(r,\mathrm{n}_{\mathrm{th}}) = \frac{(2\,\mathrm{n}_{\mathrm{th}}+1)^2}{2\,\mathrm{n}_{\mathrm{th}}(\mathrm{n}_{\mathrm{th}}+1)+1}2\sinh^2(2r), \tag{3.31}$$

while for the Fisher information (the derivation can be found in Appendix B) we obtain

$$F_{\mathrm{th},z}(\phi, r, \mathrm{n}_{\mathrm{th}}) = \frac{2\sin^2(2\phi)\sinh^2(2r)}{\left(\mathrm{e}^{-2r}\cos^2(\phi) + \mathrm{e}^{2r}\sin^2(\phi)\right)^2}\,. \tag{3.32}$$

Curiously, it appears that $F_{\mathrm{th},z}(\phi) = F_{0,z}(\phi)$. This is due to the coupling of r and n_{th} in the thermal form. It is convenient here to rewrite both expressions in the beam splitter model form, by replacing r and n_{th} with the expressions in Eq.(3.28):

$$H_{\mathrm{th},z}(r', \tau) = \frac{\mathrm{e}^{-2r'}(\mathrm{e}^{4r'} - 1)^2\tau^2(2\tau\rho(\cosh(r') - 1) - 1)}{2(\mathrm{e}^{2r'}\rho + \tau)(\mathrm{e}^{2r'}\tau + \rho)(\tau\rho(\cosh(r') - 1) - 1)} \tag{3.33}$$

$$F_{\mathrm{th},z}(\phi, r', \tau) = \frac{(\mathrm{e}^{4r'} - 1)^2\tau^2\sin^2(2\phi)}{2\left(\mathrm{e}^{2r'}\rho + \mathrm{e}^{2r'}\tau(\mathrm{e}^{-2r'}\cos^2(\phi) + \mathrm{e}^{2r'}\sin^2(\phi))\right)^2}\,. \tag{3.34}$$

As shown in Fig.3.4 and Fig.3.5, in the thermal case the Fisher information is still maximized by the expressions in Eq.(3.20), but such maximization does not saturate the quantum Cramér-Rao bound anymore [60]. It's noteworthy that for increasing transmissivity, that is for decreasing losses, the distance between the QFI and the FI increases up to a certain point, after which the two become closer until $\tau = 1$, for which there are no losses and the pure case is recovered, as shown in the Fig.3.5 (left).

In conclusion, losses in the squeezed vacuum probes cause an unequal variation of the Fisher and the quantum Fisher information, which prevent the achievement of their equality and in turn push the quantum Cramér-Rao bound beyond attainability. However, the optimal phase of Eq.(3.20) still maximizes the Fisher infrormation, therefore the implementation of an adaptive phase estimation protocol is still possible, but the expected bound on the variance will be suboptimal, as apparent from the chain of Cramér-Rao inequalities in the thermal case:

$$\mathrm{Var}\left[\hat{\phi}\right] \overset{CCR}{=} \frac{1}{MF_{\mathrm{th},z}(\phi^{\mathrm{th}}_{\mathrm{opt}})} \overset{QCR}{\geq} \frac{1}{MH_{\mathrm{th},z}}\,, \tag{3.35}$$

which is the ultimate bound on the variance that we expect to achieve in the experimental testing of the estimation protocol. We define such bound the optimal Cramér-Rao bound (OCR). A summary of the optimization steps is shown in Fig.3.6.

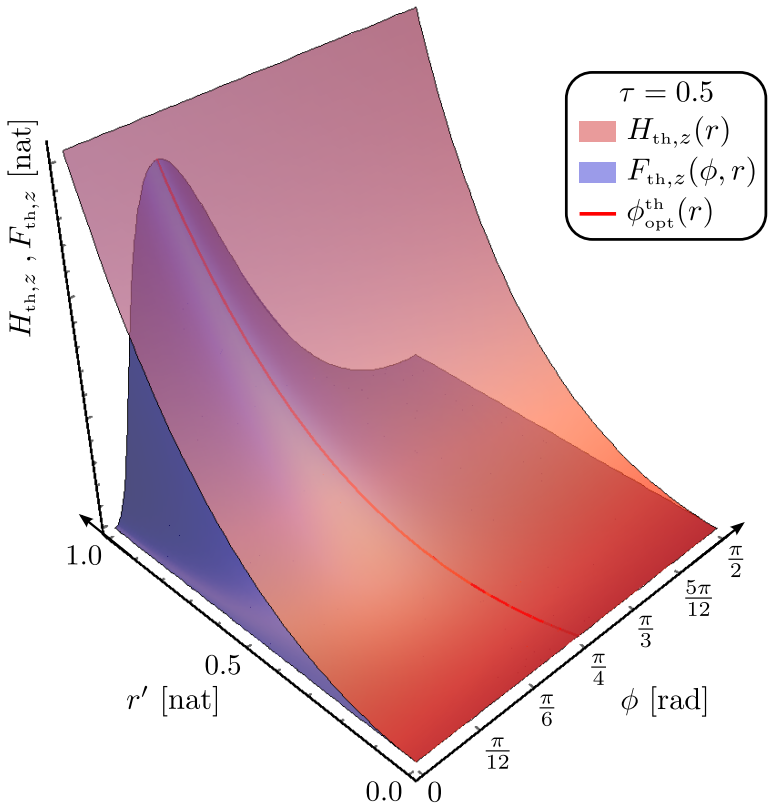

Figure 3.4: **Thermal Fisher and quantum Fisher information.** FI (blue) and QFI (red) surfaces in the lossy (thermal) case versus the input phase and the original squeezing parameter, with the loss modeled by a beam splitter with transmissivity $\tau = 0.5$. In this case the two surfaces have no contact anymore, *i.e.* there are no solutions to $H_{\mathrm{th},z} = F_{\mathrm{th},z}$. Highligthed as a red curve is the optimal phase of Eq.(3.20), which still identifies the maximum of the FI.

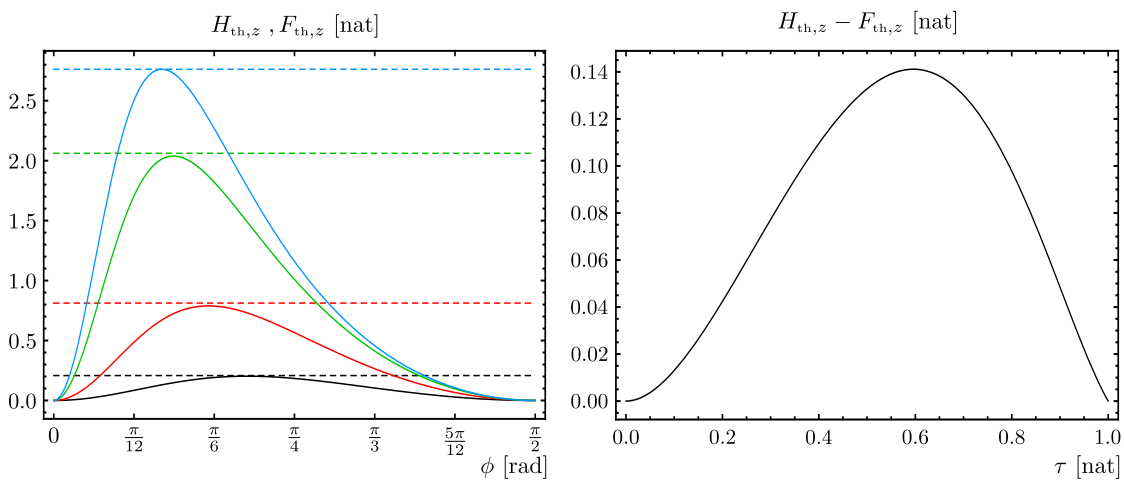

Figure 3.5: **Thermal Fisher and quantum Fisher information.** Right: FI (solid curves) and QFI (dashed lines) versus the input phase for different for different transmissivities of the loss beam splitter. Each of the curves is calculated from an original squeezed vacuum characterized by a squeezing parameter $r' = 0.5$. After the introduction of losses through the beam splitter, the resulting squeezed thermal state is defined by a new squeezing strength r and a thermalization $\mathrm{n_{th}}$. Specifically: $\tau = 1$, $r = 0.5$, $\mathrm{n_{th}} = 0$ (pure case, blue); $\tau = 0.9$, $r = 0.444$, $\mathrm{n_{th}} = 0.006$ (green); $\tau = 0.6$, $r = 0.296$, $\mathrm{n_{th}} = 0.015$ (red); $\tau = 0.3$, $r = 0.157$, $\mathrm{n_{th}} = 0.013$ (black). Left: Difference between the QFI and the FI, calculated at the maximum of the Fisher information, *i.e.* in $F_{\mathrm{th},z}(\phi^{\mathrm{th}}_{\mathrm{opt}})$, versus the transmissivity of the beam splitter.

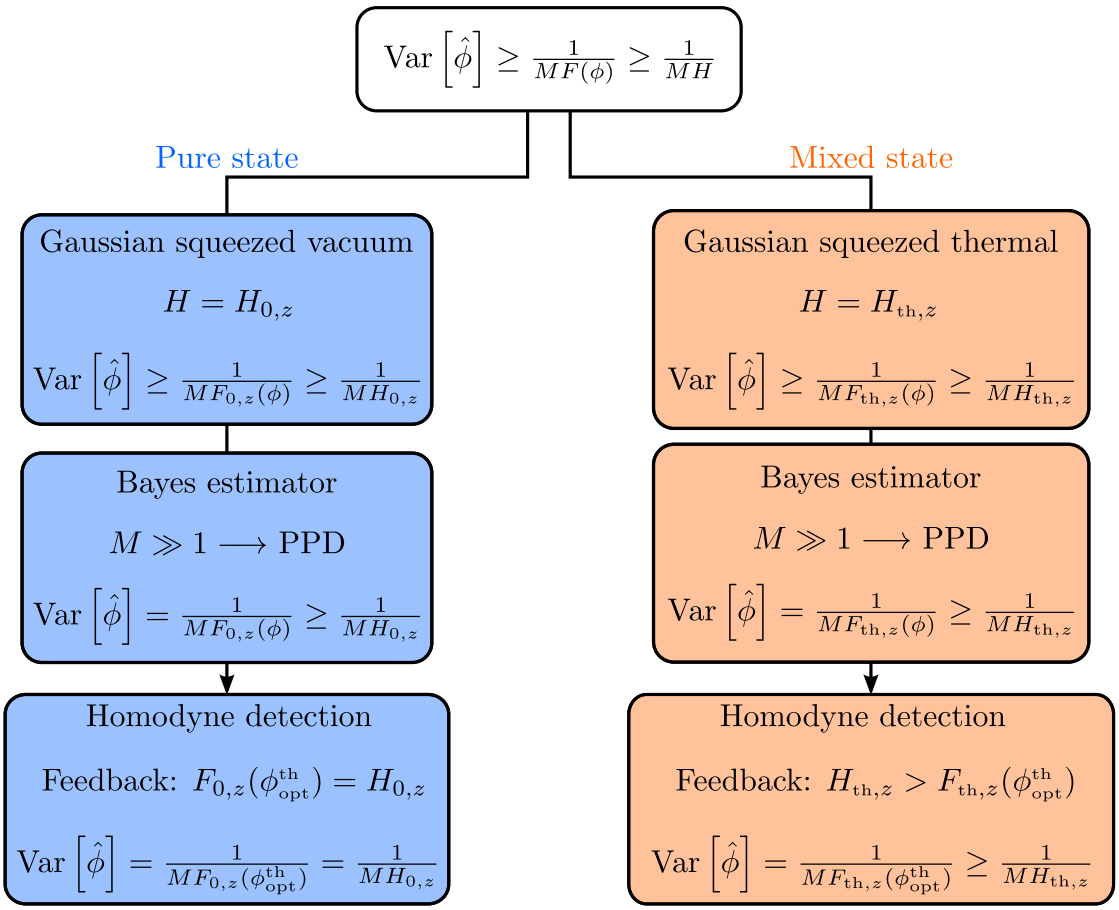

Figure 3.6: **Estimation scheme engineering.** Here we show the sequence of optimizations that, starting from the most general chain of Cramér-Rao inequalities (top), lead through the choice of a probe state, an estimator, a detection strategy. On the left (blue shade) the pure probe case, on the right (red shade) the thermal case. In each step is shown the expected variance bound.

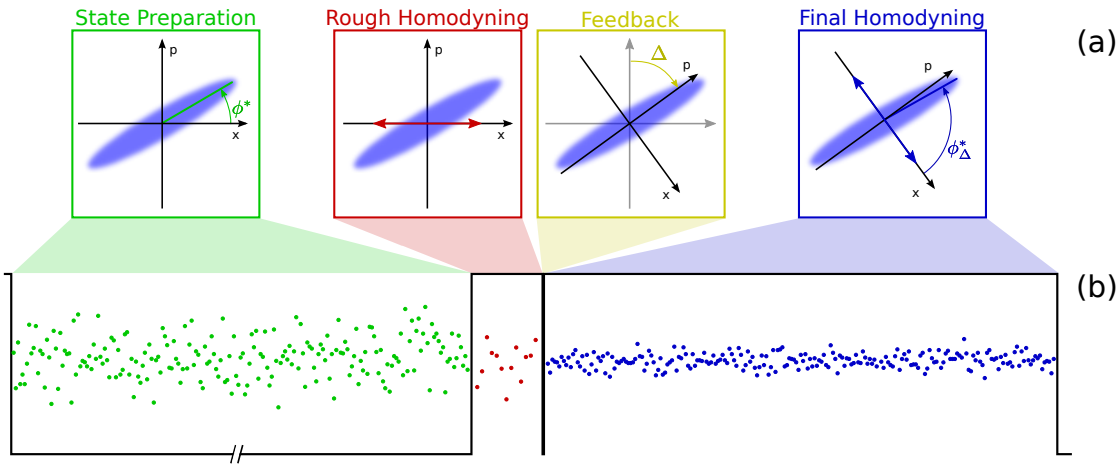

Figure 3.7: **Working principle of the phase estimation protocol. (a)**: Phase space representation. The protocol starts with state preparation (green), in which a known squeezed thermal state goes through an unknown phase shift ϕ^* in the $(0, \pi/2]$ range. A first detection stage (red) consists of M_R homodyne samples which are used to obtain a rough estimation of the phase shift via Bayesian inference, $\overline{\phi}_R$. The rough estimation result is used to compute the matching phase shift, Δ, which is applied to the local oscillator to change the relative phase to the theoretical optimal phase ϕ^{th}_{opt} (yellow). A second detection stage follows, in which $M_F \gg M_R$ homodyne samples are collected to obtain the final estimation $\mathrm{Est}[\phi^*]$ (blue). **(b)**: Experimental signals. The picture shows how the FPGA trigger (black) is tailored on the protocol stages sequence. The demodulated homodyne AC samples are shown.

3.5 Experimental implementation

In this Section we present the experimental implementation of the adaptive phase estimation protocol previously introduced. The experiment was carried out at the Max Plack Institute for gravitational physics, in the Leibnitz University of Hannover (Germany). We start with a description of the working principle of the adaptive scheme. Afterwards, we focus on the sources of the squeezed light and local oscillator. We then present some details of the optical and electronical experimental setup. Afterwards we explain the implementation of the real-time feedback strategy. We proceed giving some details on the experimental procedure, focusing on the calibrations required for an effective implementation of the protocol and on the data processing. We finally present the results of the experiment and give some concluding remarks.

3.5.1 Working principle

The working principle of the adaptive phase estimation scheme is illustrated in Fig.3.7 and Fig.3.8. It is composed of four steps: state preparation, rough estimation, adaptive feedback and final estimation.
During the first stage we prepare the input state locking it to an input phase shift ϕ^*, to be estimated.
The second stage is the rough estimation, which is necessary to compute the feedback signal required to shift the relative phase between the LO and the probe state towards the theoretical optimal phase, $\phi^{\text{th}}_{\text{opt}}$, permitting the final estimation to be performed with enhanced sensitivity. The rough homodyning produces a list of M_{R} quadrature data samples, each of which are associated with a marginal probability distribution, as in Eq.3.37. The resulting M_{R} marginals are used to compute the rough posterior probability distribution, according to Eq.(3.22). The maximum of such distribution gives the rough estimate of the input phase, $\overline{\phi}_{\text{R}} = \phi^* + \delta\phi_{\text{R}}$ with an estimation error $\delta\phi_{\text{R}}$ given by its width.
The estimation is carried out in real-time with a field-programmable-gate-array (FPGA) during the third stage, and the result is used by the FPGA to compute the matching phase shift $\Delta = \overline{\phi}_{\text{R}} - \phi^{\text{th}}_{\text{opt}}$, which is applied to the local oscillator using a fast waveguide phase modulator, thereby shifting the phase to $\phi^* \longrightarrow \phi^* - \Delta = \phi^{\text{th}}_{\text{opt}} - \delta\phi_{\text{R}} = \phi^{\text{exp}}_{\text{opt}}$. It is important to observe that the feedback phase shift Δ calculation is based on the rough estimation, but is applied on the actual input phase ϕ^*, thereby imposing a difference between the theoretical optimal phase and the measured one (which we call experimental optimal phase, $\phi^{\text{exp}}_{\text{opt}}$).
In the fourth and final stage the final homodyning is performed, which delivers $M_{\text{F}} \gg M_{\text{R}}$ quadrature data samples to obtain an estimation of the experimental optimal phase $\overline{\phi}_{\text{opt}} = \phi^{\text{exp}}_{\text{opt}} + \delta\phi_{\text{F}} = \phi^{\text{th}}_{\text{opt}} - \delta\phi_{\text{R}} + \delta\phi_{\text{F}}$. Thanks to the larger number of samples in the final homodyning and the enhanced homodyne sensitivity due to the proximity of the optimal phase, we get $\delta\phi_{\text{F}} \ll \delta\phi_{\text{R}}$. To obtain the final estimate we shift $\overline{\phi}_{\text{opt}}$ by an amount Δ: $\text{Est}\,[\phi^*] = \overline{\phi}_{\text{opt}} + \Delta = \phi^* + \delta\phi_{\text{F}}$, where ϕ^* constitute the final phase estimate with an error $\delta\phi_{\text{F}}$.

3.5.2 Probe states generation and control

Our light source was a telecom laser which emitted 1 W at 1550 nm. The output light was prepared by an impedance-matched triangular ring mode-cleaning cavity with a finesse of ~ 300, which filtered the TEM00 spatial mode and low-passed high frequency noise. A digital synthesizer was used to generate the 115 MHz

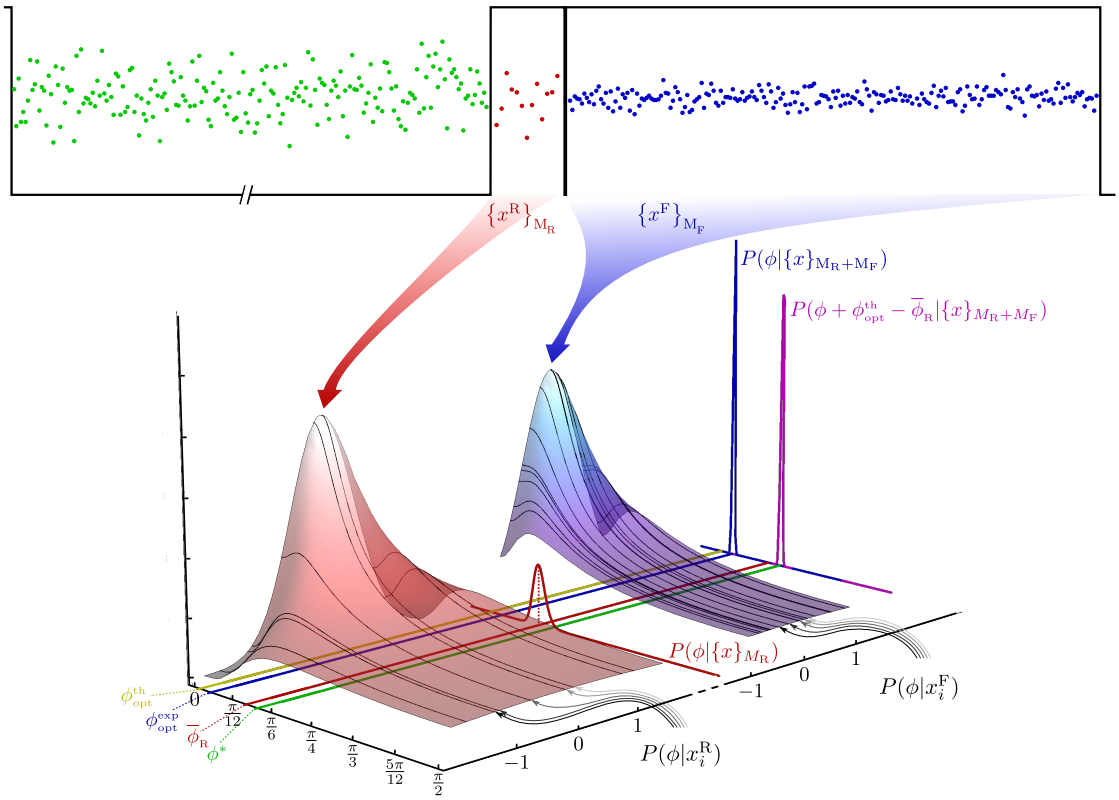

Figure 3.8: **Working principle of the phase estimation protocol.** Example of an instance of computation of the posterior probability distributions. Each homodyne sample x_i collected during the estimation stages is used to compute a marginal phase distribution $P(\phi|x_i)$. The marginal distributions are multiplied according to Eq.(3.38) to obtain the posterior probability distribution $P(\phi|\{x\}_{\mathrm{M}})$ for the rough (left) and the final (right) estimation. The input phase ϕ^*, rough estimation $\overline{\phi}_{\mathrm{R}}$, theoretical optimal phase $\phi^{\mathrm{th}}_{\mathrm{opt}}$ and experimental optimal phase $\phi^{\mathrm{exp}}_{\mathrm{opt}}$ are shown. We show the resulting PPDs versus phase for a single application of the protocol.

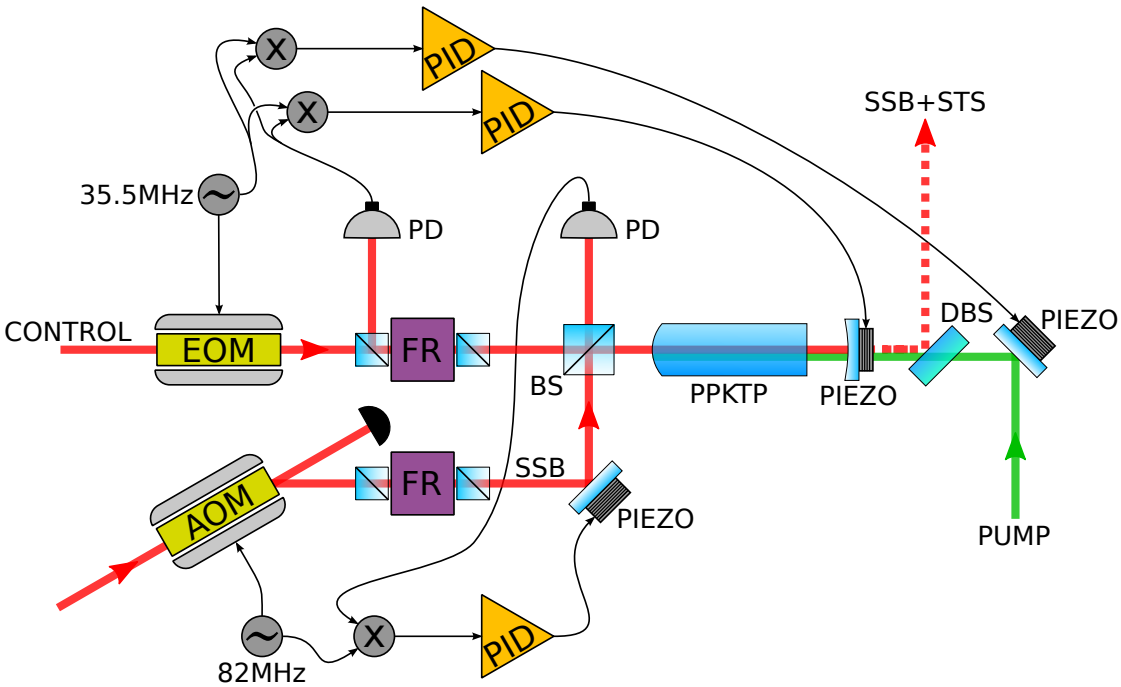

Figure 3.9: **Squeezing generation setup.** We used a PPKTP crystal for degenerate parametric down-conversion in a linear cavity. The cavity was kept on resonance using a PDH locking scheme. The generation of amplitude squeezing was ensured by locking the relative phase between the pump and the control beam. A single sideband locking scheme was used to set the squeezing phase relative to the local oscillator, for the experiment state preparation. EOM: Electro Optical Modulator. AOM: Acousto Optical Modulator. FR: Faraday Rotator. SSB: Single Sideband. PID: servo controller. PD: Resonant Photo Detector. STS: Squeezed Thermal States. DBS: Dichroic Beam Splitter. BS: 50 50 Beam Splitter.

local oscillator used to drive an electro optical modulator for PDH locking [61] of the mode-cleaning cavity on resonance. The signal produced by detecting the light reflected off the mode cleaner's incoupling mirror with a resonant photo detector was demodulated using the electronic local oscillator, generating an error signal that a servo controller used to drive a piezo mounted mirror in the mode-cleaning cavity [62]. The light was then split using wave plates and polarizing beam splitters to reach different parts of the optical table as a local oscillator for homodyne detection, as a pump for second harmonic generation, and as a control beam for the generation of squeezed light.

To generate the pump beam to drive the squeezer we used a second harmonic generation (SHG) setup, in which a nonlinear periodically poled potassium titanyl phosphate (PPKTP) crystal was used for parametric up conversion of the 1550 nm light field to 775 nm. The PPKTP crystal was 9.3 mm long with a curved face (radius: 12 mm) coated for high reflectivity at both the fundamental and the up-converted wavelengths. The plane face of the crystal was in turn anti-reflective coated for both wavelengths. A piezo-mounted curved coupling mirror with 25 mm radius of curvature, 90% reflective coating for 1550 nm and a small residual reflectivity for 775 nm faced the plane side of the crystal, forming, together with the curved end of the crystal, a linear cavity to enhance the conversion efficiency to 85%. Phase matching conditions in the linear cavity were ensured by careful tuning and stabilization of the crystal's temperature, actuated by a Peltier element. Again, a PDH scheme was implemented to keep the cavity on resonance. The output light at 775 nm was then split from the input 1550 nm pump by a dichroic beam splitter and sent to the squeezer cavity as a pump beam. For a detailed description of the mode-cleaning and SHG setups, see [63].

Squeezed light was produced by degenerate parametric down-conversion in a linear cavity similar to the one used for the SHG process, the only differences being the coupling mirror reflectivity which was 90% for the fundamental harmonic (1550 nm) and 20% for the pump beam (775 nm), see Fig.3.9 for reference. A control beam, phase modulated at 35.5 MHz, entered the cavity from the curved face of the PPKTP crystal. The reflected light went back into a PBS and Faraday rotator system which diverted it into a resonant photo detector. The signal from this detector was demodulated with an electronic local oscillator and fed into a servo controller to drive the piezo mounted coupling mirror and to lock the cavity on resonance. The pump beam was coupled into the cavity through the piezo mounted coupling mirror. The relative phase between the pump and the control beam was locked by mixing the signal from the resonant photo detector with a $\pi/2$

shifted electronic local oscillator and feeding the resulting error signal to a servo which controlled a piezo mounted mirror used for directing the pump beam on the cavity coupling mirror. The pump beam was locked on amplitude squeezing, thus deamplifying the amplitude noise in the control beam.

The relative phase between the probe states and the local oscillator was set using a single sideband locking scheme: the single sideband (SSB) was generated by an acousto-optical modulator (AOM) at 82 MHz. The SSB was mixed with the squeezer's control beam at a 50 50 beam splitter, and the output was detected by a resonant photo detector. The signal was then demodulated and used as an error signal for locking the relative phase between the SSB and the control beam. Another Faraday rotator in the path of the SSB prevented the build-up of parasitic cavities. This locking scheme allowed us to set the probe states to any phase between squeezing and anti-squeezing for the experiment state preparation. The squeezed light output and the SSB were separated from the pump beam by a dichroic beam splitter and directed to the phase estimation setup, described in the next section.

3.5.3 Experimental setup

The experimental setup is shown in Fig.3.10. The experiment required the preparation of an initial state as a phase shifted squeezed thermal state (STS), with the phase in the range $[0, \pi/2)$ which is the parameter we wanted to estimate. State preparation was accomplished by using the single sideband lock to set the relative phase between the LO and the probe STS, as explained in Sec.3.5.2. The LO, coming from the mode-cleaning cavity, went through a waveguide phase modulator (WGM) which was used to actuate the feedback, matching the optimal phase. The LO and the STS interfered on a 50 50 beam splitter and the output ports were detected in a balanced homodyning setup with visibility 90% and quantum efficiency of 99%. The SSB light provided the modulation for locking the homodyning phase.

The homodyne AC signal was split in two parts, one of which was used for the SSB lock. The other homodyne AC part, used for carrying the phase information, was mixed down to DC using a double balanced mixer, with mixing frequency 9 MHz. After the mixer the signal was low-pass filtered at 1.9 MHz, before reaching a preamplifier set to low-pass filter at 300 kHz, with a roll-off of 12 dB per octave and gain 100. The preamplifier output was once again attenuated by a variable attenuator, and was then fed in a custom offset amplifier which was set to gain 3

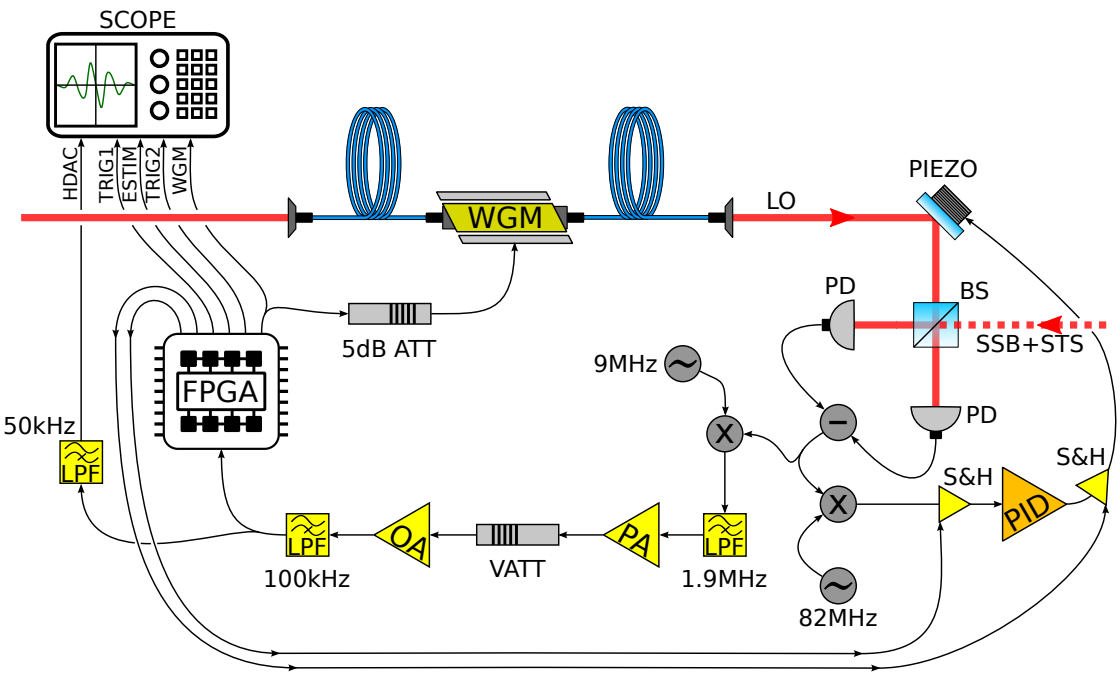

Figure 3.10: **Experimental setup.** We performed balanced homodyne detection on the squeezed thermal probe states. The AC output of the homodyne detector was split in two parts: one was used for locking the homodyning phase using the SSB modulation, and the second part was demodulated at 9 MHz, low-pass filtered, amplified and used as analog input for the FPGA. The FPGA computed the variance of the AC input and used the result to drive a waveguide modulator into matching the optimal relative phase between STS and LO. The other outputs of the FPGA and part of the homodyne AC signal were sampled by an oscilloscope and saved for data processing. LO: Local Oscillator. WGM: Waveguide Modulator. PIEZO: Piezoelectric mounted mirror. STS: Squeezed Thermal States. SSB: Single Sideband. PID: servo controller. PA: Pre-Amplifier. OA: Offset Amplifier. FPGA: Fast Programmable Gate Array. ATT: Attenuator. VATT: Variable Attenuator. LPF: Low-Pass Filter. PD: Photo Detector. BS: Beam Splitter. S&H: Sample and Hold circuit. The oscilloscope inputs: HDAC: Demodulated Homodyne AC. TRIG1: Protocol Trigger. ESTIM: Estimation output. TRIG2: Sampling Trigger. WGM: Feedback signal.

and also added a 875 mV DC offset to match the middle of the FPGA (Fast Programmable Gate Array, a Xilinx Spartan 3E) analog input range. A final low-pass filter set the input state's bandwidth at 100 kHz. Afterwards, this signal was split, with one part being again low-pass filtered at 50 kHz and sampled at 100 kHz by an oscilloscope, and the other end feeding the analog input of the FPGA with a sampling rate of 57 kHz.

The WGM was operated by one of the FPGA analog outputs, which was attenuated by 5 dB to match the WGM half-wave voltage. Before attenuation, the FPGA output feedback signal was split, and part of it was sent to the oscilloscope for control. A second analog output of the FPGA containing the estimation result was sampled by the oscilloscope as well.

Four digital outputs of the FPGA were used as triggers for different processes: a first trigger defining the protocol sequence (cfr. Fig.3.7) was sampled by the oscilloscope as a reference trigger for the data processing (cfr. Sec.3.5.7). A second digital output was used to trigger the oscilloscope sampling. Finally, the last two digital outputs were used to trigger two sample and hold circuits (S&H) which were added to the input and the output of the SSB lock servo controller to prevent it from correcting the feedback action of the WGM. In particular, the input S&H was used to hold the input error signal on the last locking point (initial phase) and the output S&H to hold the actuation signal from the servo to keep the piezo in position. Both S&Hs were activated just before the feedback action of the WGM and turned off right after the WGM went back at the reference level, at the end of the final estimation.

3.5.4 FPGA operations

The main purpose of the FPGA is to compute a real-time rough estimation of the input phase from the data gathered in the first homodyning stage, and derive the required matching phase shift Δ to drive the WGM. As explained in Sec.3.5.1, the estimation on the input phase is derived from the posterior probability distribution. The PPD itself is computed using the sampled homodyne data, and the estimation of the input phase is found as the mode of the distribution, which converges to the mean value as the number of homodyne samples increases, as explained in Sec.3.4.1. The PPD formalism relies on the assumption that an univocal correspondence between the sampled variance Σ^2 and the input phase ϕ can be constructed from the probe state covariance matrix of Eq.3.30, in particular

from the first diagonal element for amplitude-squeezing, as

$$\Sigma^2 \leftrightarrow \sigma^2 \leftrightarrow \phi\,,$$
$$\sigma^2 = (\hat{\boldsymbol{\sigma}}_{\mathrm{th},z})_{1,1} = (2\,\mathrm{n}_{\mathrm{th}} + 1)\left[\mathrm{e}^{-2r}\cos^2(\phi) + \mathrm{e}^{2r}\sin^2(\phi)\right]\,. \tag{3.36}$$

This allows us to define the phase-space probability distribution as the Gaussian distribution

$$p(\phi|q) = \frac{1}{\sqrt{2\pi\sigma^2}}\mathrm{Exp}\left[-\frac{q^2}{2\sigma^2}\right], \tag{3.37}$$

which in turn defines the phase marginal distribution when a sampled quadrature is given. The PPD is obtained as a normalization of the product of all the marginal distributions built using the M sampled quadratures $\{x\}_{\mathrm{M}}$, as in Eq.(3.22),

$$P(\phi|\,\{x\}) = \frac{1}{\mathfrak{N}}\prod_i p(x_i|\phi), \tag{3.38}$$

where $\mathfrak{N}$ is a normalization factor. The phase estimate is then found as the maximum the PPD, that is, by finding the most likely phase given the observed quadrature set $\{x\}_{\mathrm{M}}$.

In the context of a real-time feedback, the computation of the PPD for the rough estimation is time consuming and requires advanced mathematical operations which can't be efficiently implemented within the FPGA architecture, therefore we need to resort to a different strategy. A simpler way of estimating the phase from the observed quadrature set would be to solve the inverse of the phase-variance relation of Eq.(3.36) as $\Phi(\Sigma^2) = [\sigma^2]^{-1}(\Sigma^2)$. Since the phase range is limited to $[0, \pi/2)$, the associated theoretical variance range is similarly restricted in $[\sigma^2(0), \sigma^2(\pi/2))$. This means that when the sampled variance exceeds the theoretical variance domain boundaries no solution can be found with the latter approach. The PPD formalism solves this problem by clamping the distribution on the phase domain edges whenever the sampled variance exceeds the theoretical variance domain, and we can model this property by redefining the inverse phase-variance relation to deal with the extra-domain sampled variances

$$\Phi(\Sigma^2) = \begin{cases} \pi/2 & \forall \quad \Sigma^2 \geq \sigma^2(\pi/2) \\ [\sigma^2]^{-1}(\Sigma^2) & \forall \quad \sigma^2(0) \leq \Sigma^2 \leq \sigma^2(\pi/2) \\ 0 & \forall \quad \Sigma^2 \leq \sigma^2(0) \end{cases} \tag{3.39}$$

Such expression represents an equivalent formulation of the PPD formalism, as shown in Fig.3.11, and the most convenient way to implement it on the FPGA is by using a lookup table (LUT) generated by means of a proper calibration, which

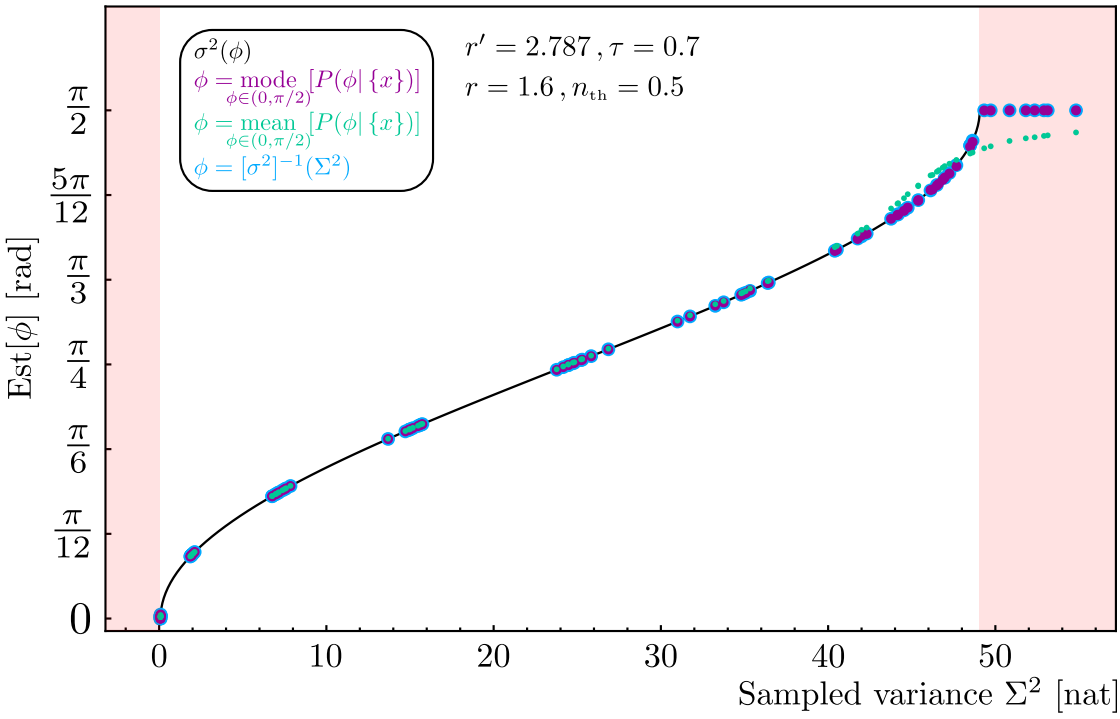

Figure 3.11: **Univocal correspondence between the sampled variance and the estimated phase.** We simulate a probe state with original squeezing strength $r' = 2.787$ and losses determined by a beam splitter of transmissivity $\tau = 0.7$, which corresponds to a squeezed thermal probe with $r = 1.6$ and $\mathrm{n_{th}} = 0.5$. We generate 1000 homodyne data points for 9 different initial phases. We compute the variance of the samples and the PPD for each of the 9 sets. We extract the mean value and the mode from each PPD, and we recover the estimated phase from the inverse variance-phase relation given by Eq.(3.39). We repeat the process 10 times. It is worth noticing how the $\sigma^2(\phi)$ function (black curve) is not defined beyond the true variance domain boundary (the white background region), therefore if the sampled variance exceeds the $\left[\sigma^2\right]^{-1}$ domain, no solutions can be found and the estimation fails. Instead in the same regions both the PPD mode (purple dots) and the extended $\Phi(\Sigma^2)$ function (light blue dots) successfully deliver a phase estimation. We also show the mean value of the PPD (green dots), which deviates from its mode as the Gaussian approximation fails, *i.e.* as the input phase moves further away from the optimal phase.

will be explained thoroughly in Sec.3.5.5.

Since the estimation protocol we tested relied on real-time feedback, the variance of the homodyne signal in the FPGA had to be calculated in an online fashion. This was possible using the following iterative algorithm:

$$\mathrm{Var}\left[\{x\}_M\right] \Longrightarrow \begin{cases} \delta_i = x_i - \langle x \rangle_{i-1} \\ \langle x \rangle_i = \langle x \rangle_{i-1} + \frac{\delta_i}{i} \cdot \mathfrak{N}_1 \\ m_i^2 = m_{i-1}^2 + \delta_i \cdot (x_i - \langle x \rangle_i) \cdot \mathfrak{N}_2 \\ \mathrm{Var}\left[\{x_\psi\}_{1\cdots i}\right] = m_i^2 \end{cases} \tag{3.40}$$

where x_i is the i-th homodyne sample digitized into a 14 bit value and $\mathfrak{N}_1$ and $\mathfrak{N}_2$ are binary normalization factors whose purpose is to prevent overshooting, in other words to make sure the final digital value of the estimated variance is inside the digital range $[0, 2^{14}]$.

3.5.5 Calibrations and lookup tables

In the following section we describe the calibrations that are required for effective implementation of the estimation protocol. We test the protocol for four different total number of homodyne samples to test the scaling of the estimation variance against the Cramér-Rao benchmarks of Eq.(3.35). Some calibrations are required before each of the four tests, while others need to be performed only once.

System parameters estimation

Estimation of the squeezing strength r and the mean number of thermal photons $\mathrm{n_{th}}$ in the probe states was needed beforehand to compute the optimal phase and the state energy. We extracted an estimation for such parameters from a squeezing trace measurement. We indicate amplitude and phase variances respectively with Σ_{sqz} and Σ_{asqz}. They can be expressed as the first and second diagonal elements of the state's covariance matrix of Eq.(3.30), with $\phi = 0$ (because we generate amplitude-squeezing):

$$\begin{cases} \Sigma_{sqz} & = (2\,\mathrm{n_{th}} + 1)e^{-2r}\,, \\ \Sigma_{asqz} & = (2\,\mathrm{n_{th}} + 1)e^{2r}\,. \end{cases} \tag{3.41}$$

Solving the system above straightforwardly leads to the expressions we need to estimate r and $\mathrm{n_{th}}$ from the homodyne measurement:

$$\begin{cases} r &= \frac{1}{2}\log\left[\frac{\Sigma_{asqz}}{\sqrt{\Sigma_{sqz}\Sigma_{asqz}}}\right], \\ \mathrm{n_{th}} &= \frac{\sqrt{\Sigma_{sqz}\Sigma_{asqz}}-1}{2}. \end{cases} \tag{3.42}$$

The measurement of Σ_{sqz} and Σ_{asqz} was performed by homodyning the squeezed and antisqueezed quadratures with a zero-span measurement at 9 MHz of the homodyne AC traces with a spectrum analyzer set to a resolution bandwidth of 300 kHz, a video bandwidth 100 Hz and a sweeping time 200 ms. We also needed to measure the relative noise of the vacuum in our probe states for the data processing, which was easily obtained within the same measurement by blocking the pump beam to the squeezer. An example of such a measurement is illustrated in Fig.3.12, while the results are summarized in Table 3.1. We conducted the parameter estimation before each of the four tests of the protocol (each one relative to a different M_{tot}), since a variation in the squeezing strength leads to a variation in the optimal phase that had to be taken into account in the FPGA feedback calibration.

FPGA digital-to-analog converter calibration

The WGM rotates the local oscillator phase according to the feedback signal that it receives from the FPGA. The feedback signal itself is generated in the FPGA during the third stage of the protocol as a binary value in the range $[0, 4096) \equiv [0, 2^{12})$. The digital signal is converted to an analog voltage in the range $[0, 3.3)$ V. We expected this calibration function to be linear, and indeed we verified that by programming the FPGA to hold a number of specific digital outputs equally spaced in the digital output range, and measuring the corresponding analog output (see Fig.3.13). We could then fit the data to a function that converted from output bit value to output voltage. Since this calibration only depended on the FPGA digital-to-analog converter (DAC), we only needed to perform it once.

Variance estimation calibration

The purpose of this calibration procedure was dual: In primis, we needed calibration functions to convert from input homodyne AC variance to estimation output voltage and vice versa. These functions were then used for the feedback

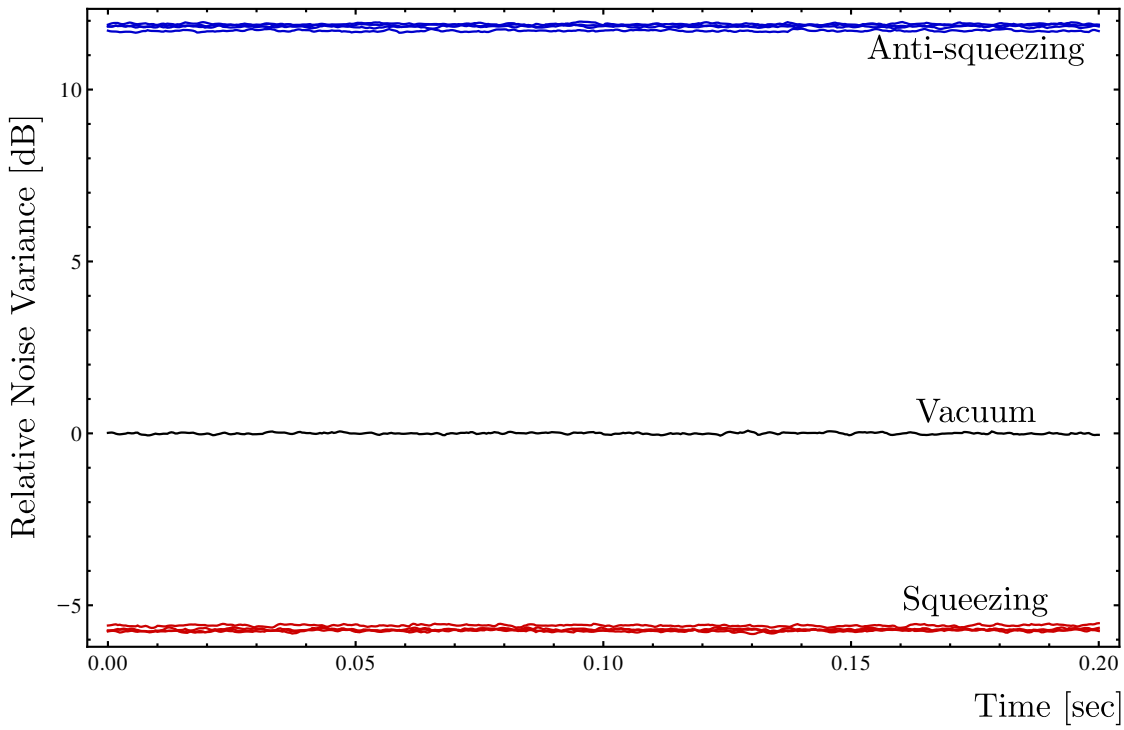

Figure 3.12: *System parameters estimation.* Noise traces on the spectrum analyzer during the system parameters estimation. The black line is our vacuum state, while the red and blue traces correspond to the squeezing and antisqueezing levels respectively. The results are relative to all the four instances of the experiments.

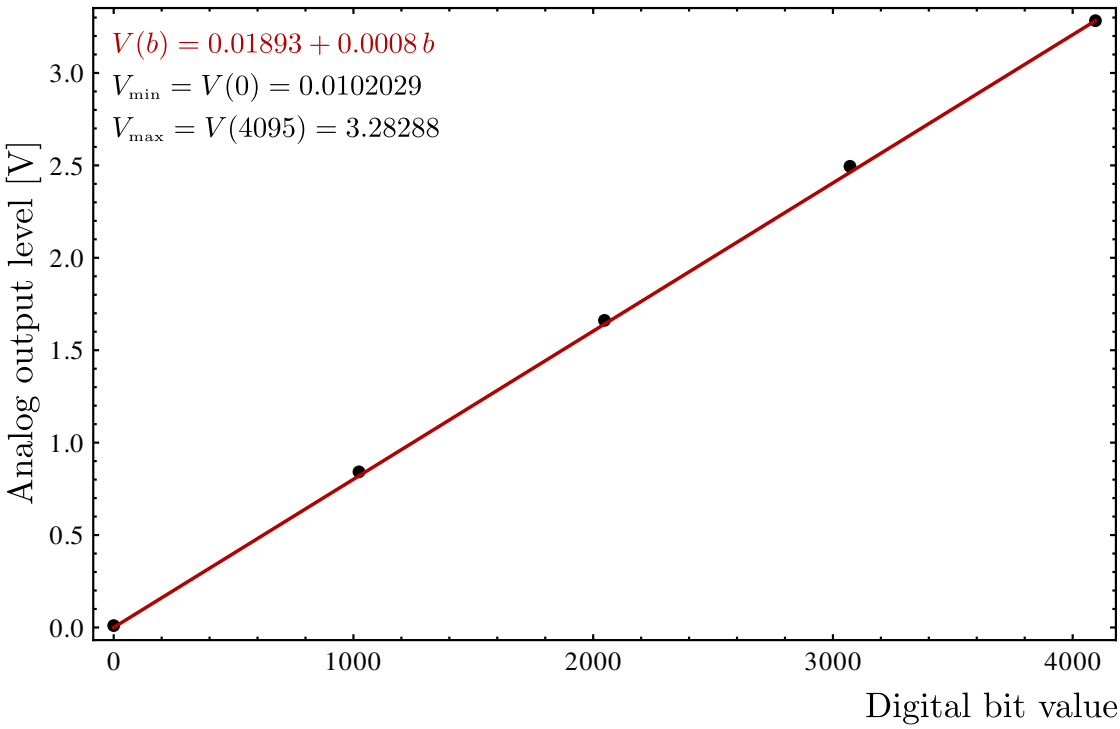

Figure 3.13: **FPGA digital-to-analog converter calibration.** We set the FPGA to hold four digital outputs equally spaced in the $[0, 4096)$ range. We then measured the voltage outputs of the digital-to-analog converter (black dots) and we fitted the results (red line). The fit function is provided in the top left corner (red). The minimum and maximum voltage outputs are also indicated.

calibration as well as for the data processing. The calibration procedure required the WGM to be offline, and it was performed by feeding the FPGA analog input with the demodulated homodyne AC relative to several different input phases and measuring the correspondent voltage output level in the rough and in the final estimation. This was accomplished by locking the STS probe state to several relative phases between 0 (squeezing sampled variance) and $\pi/2$ (anti-squeezing sampled variance). For each one of these initial states we performed a repeated run of the protocol (with no feedback), registering the homodyne AC signal as well as the rough estimation output, the final estimation output, and the protocol trigger from the FPGA. We used the homodyne AC data to compute the input variance, and we fitted it to the estimation output voltage.

Since the rough estimation is required to estimate initial phases in the whole $[0, \pi/2)$ radians range, all the sampled variances between the squeezing and the anti-squeezing variance were used to compute the rough estimation calibration function (CalREst). On the other hand, the final estimation is designed to estimate phases in the proximity of the optimal phase, which corresponds to an input variance lying between the squeezing and the vacuum ones. Therefore only the input variances between squeezing and vacuum were needed to compute the final estimation calibration function (CalFEst). Fig.3.14 shows the result of one such calibration.

As a second purpose, this procedure was useful for setting the value of the scaling factor which defines the rescaling of the digital estimation result to efficiently use the whole FPGA analog output range. The values of r and $\mathrm{n_{th}}$ imply a minimum and a maximum variance of the homodyne AC signal as $(2\,\mathrm{n_{th}}+1)e^{-2r}\cdot\mathrm{Var}\,[\mathrm{vacuum}]$ and $(2\,\mathrm{n_{th}}+1)e^{+2r}\cdot\mathrm{Var}\,[\mathrm{vacuum}]$, respectively. This defines a minimum and a maximum estimation output voltage, according to the FPGA DAC calibration. To use the analog output range efficiently we defined a scaling factor for the rough estimation stage and one for the final estimation stage, and since these factors depend on the r and $\mathrm{n_{th}}$ parameters, this calibration procedure had to be repeated before each of the four experimental tests.

Calibration of waveguide phase modulator

The waveguide modulator applies a phase shift to the local oscillator to match the optimal phase. Depending on the actual value of the true phase, such phase shift varies between a minimum Δ_{min} (applied when the true phase is $\phi^* = 0$) and a maximum Δ_{max} (applied when the true phase is $\phi^* = \pi/2$). The purpose of this

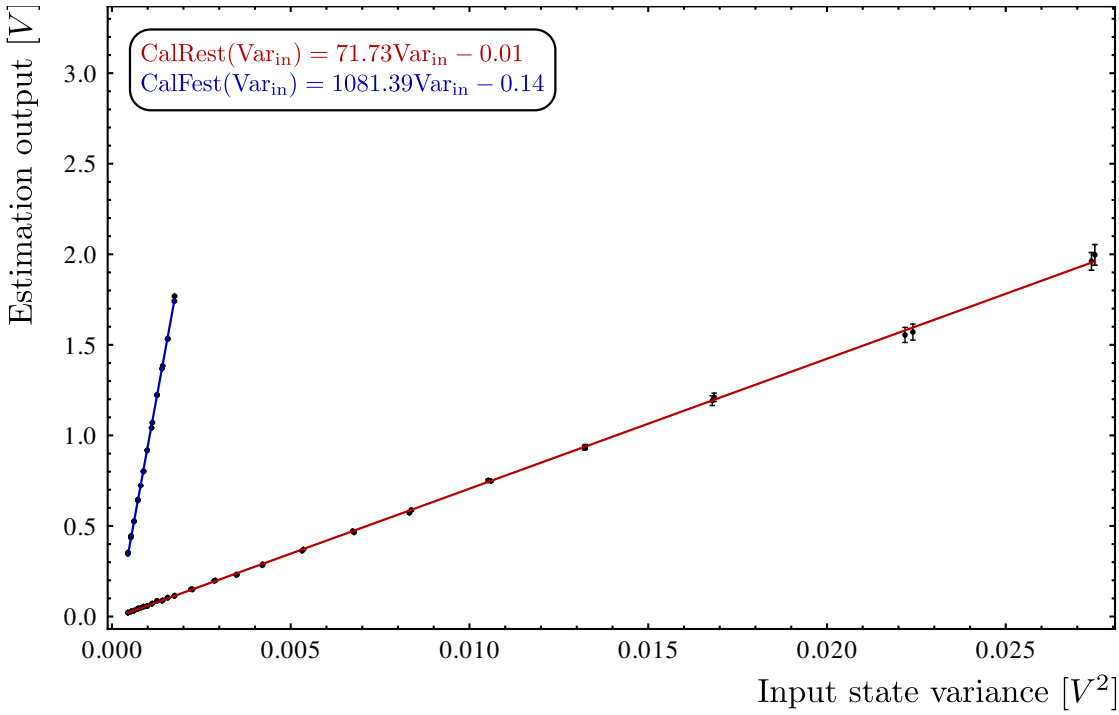

Figure 3.14: **Variance estimation calibration function.** For the rough estimation calibration function (red) we measured a number of input variances between the squeezing and the anti-squeezing variance, corresponding to input phases in the whole $[0, \pi/2)$ [rad] range. For the final estimation calibration function (blue) we measured a number of input variances between the squeezing and the vacuum variance, corresponding to input phases in proximity of the optimal phase.

calibration was to find a $\Delta(V)$ voltage-to-phase shift relation to drive the WGM in the whole needed phase range $[\Delta_{\min}, \Delta_{\max}]$. Moreover, we wanted the WGM to apply a vanishing phase shift when the feedback voltage was 0 V.
To calibrate the WGM response we performed homodyne detection on a bright field while scanning the WGM. We detected the homodyne DC signal and we fitted its amplitude to the scan amplitude, using a cosine function as initial guess for the fit function: $DC\,(V) = A\cos(\omega_1 V + \omega_0) + B$. This fit function converts from input voltage to homodyne DC amplitude, as shown in Fig.3.15. We needed to convert the homodyne DC amplitude into a phase shift, to obtain the WGM input voltage to phase shift calibration function. To do this, we can simply build the phase function as the argument of the cosine: $\Delta\,(V) = \omega_1 V + \omega_0$.

The initial phase is in the range $[0, \pi/2)$ radians, while the optimal phase only depends on the squeezing parameter according to Eq.(3.20). Since in the course of the four experimental tests we kept an approximately constant squeezing level corresponding to $r \simeq 1$, that is ~ -6 dB of relative noise in the squeezing quadrature, we had $\phi_{\text{opt}}^{\text{th}} \simeq 0.13$ radians, or $\simeq 7.6$ degrees. Therefore we needed the WGM to apply a maximum positive phase shift of $\pi/2 - \phi_{\text{opt}}^{\text{th}} \simeq 1.4385$ radians, or $\simeq 82$ degrees, and a minimum negative phase shift of $0 - \phi_{\text{opt}}^{\text{th}} \simeq -0.13$ radians, or $\simeq -7.6$ degrees. To encompass the whole needed phase range, we defined the maximum and minimum phase shifts as $\Delta_{\max} = +90$ deg and $\Delta_{\min} = -10$ deg.
Once the WGM calibration was complete, we could use the calibration functions to build a LUT to convert from the rough phase estimate to the necessary feedback voltage required to apply the correct matching phase shift, $\Delta = \bar{\phi}_{\text{R}} - \phi_{\text{opt}}^{\text{th}}$. Since the feedback lookup table required the definition of a scaling factor which depended on the system parameters r and n_{th}, the generation of a new calibrated lookup table was required before each of the four experimental tests to address the small changes in the squeezing strength.

3.5.6 Experimental procedure

We wanted to study the scaling of the estimation variance as a function of the total number of homodyne samples used for a single protocol run, while also investigating the performances of the estimation protocol for fixed number of samples and varying initial phase. To do this, we selected four total numbers of homodyne samples $M_{\text{tot}} = M_{\text{R}} + M_{\text{F}}$ to be investigated. For each of the four M_{tot} we selected a few initial phases to estimate, and we repeated the estimation protocol on each of these input phases 80 times to give the results statistical significance.

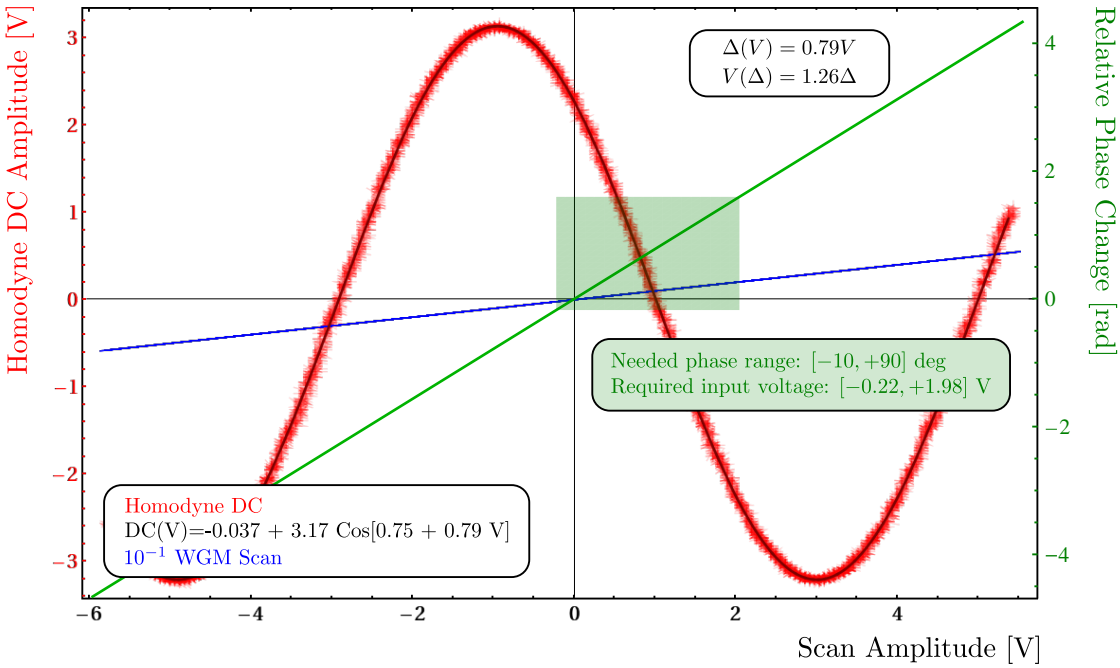

Figure 3.15: **Waveguide modulator calibration.** Left vertical axis: Homodyne DC signal fit versus WGM scan amplitude. The homodyne DC signal (red) was fitted to the scan amplitude (blue line, rescaled) in a calibration function (black curve, superposed to the DC signal). The fit function DC(V) is provided. Right vertical axis: normalized optical phase shift versus WGM scan amplitude. The calibration functions from WGM scan amplitude to phase ($\Delta(V)$) and vice versa ($V(\Delta)$) are plotted (green line) and their expression provided in the top right corner. The shaded green region identifies the voltage range $[-0.22, +1.98]$ V required to apply a phase shift in the needed range $[-10, +90]$ deg.

This measurements gave us information on the protocol performances for varying initial phase, while averaging all such results over the input phases gave us four data points to verify the scaling of the estimation variance versus M_{tot}.

The first operations we needed to perform were the FPGA digital-to-analog calibration and the WGM response calibration described in the previous Section, which only had to be done once. Before each of the four experimental tests we fixed the number of homodyne samples M_{tot} and the power of the pump beam at 105 mW. We then set the optical power of the LO at the reference value of 8.6 mW, locked the system and proceeded with the system parameters estimation. This provided an estimation of the squeezing strength r, of the thermalization n_{th}, and the variance of the vacuum.
Successively, we proceeded with the variance estimation calibration. From this calibration we obtained the calibration functions CalREst and CalFEst, which, together with the system parameters, the FPGA calibration function, and the WGM response calibration function, were used to generate the feedback LUT.
Once the feedback LUT was loaded in the FPGA we started with the experimental test, which was performed in a very similar fashion to the operations performed during the variance estimation calibration, the only difference being that in the latter the WGM was kept offline, while in the former it was used for the feedback to the optimal phase. We locked the probe state on an initial phase between the squeezing and the anti-squeezing phases, and performed a 10 seconds measurement with the oscilloscope, which included a number of repetitions of the estimation protocol, as illustrated in Fig.3.16. We repeated the experiment on a number of initial phases in the range $[0, \pi/2)$ radians.
Once enough initial phases were measured the experiment was complete. We then fixed a new M_{tot} and started again with the system parameter estimations, the variance estimation and feedback calibrations. Details on the parameters characterizing each experiment are given in Table 3.1.

3.5.7 Data processing

The data processing was performed using Wolfram Mathematica V.10. The data provided by a single run of the estimation protocol (see Fig.3.16) was structured as follows: each of the four oscilloscope channels were used during the data acquisition, as previously mentioned in Sec.3.5.3. The signal registered by each channel had to be processed differently, also depending on the time position of the data points with respect to the FPGA trigger.

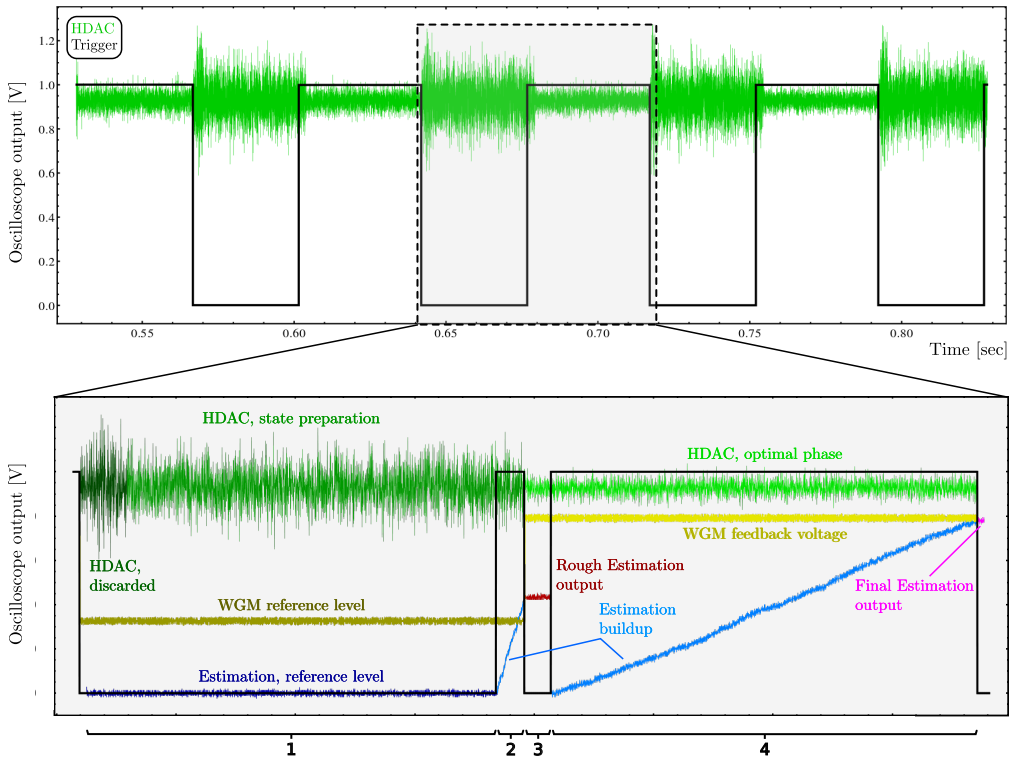

Figure 3.16: **Oscilloscope outputs.** Top: an example of a short section of a measurement in which a single input phase is being estimated. The estimation protocol (trigger up) is repeated on the same input phase (state preparation identified by the trigger down) to give the final results statistical significance. The demodulated homodyne AC data (HDAC) is also shown (green). Bottom: example of the oscilloscope signals during a single protocol run. The FPGA trigger (black) identifies the different protocol stages, which are also indexed by numbers at the very bottom. **(1)** state preparation: both the estimation voltage output and the WGM feedback are at reference level. The probe state is locked on ϕ^* and the lock is let stabilize (note the spikes in the HDAC data at the beginning of the stage). Part of the HDAC data is discarded because the lock hasn't stabilized yet. **(2)** rough estimation: The WGM is still at reference level, while the estimation output starts to increase as more and more HDAC data is sampled. **(3)** feedback: the FPGA sends the WGM the feedback signal, shifting the probe's phase on $\phi_{\text{opt}}^{\text{exp}}$. The feedback has a duration of 10 μs, but this stage was designed to be longer for control during the experiment, and to easily verify the rough estimation scaling factor (see variance calibration subsection).**(4)** final estimaton: this stage is completely equivalent to the rough estimation stage, the only difference being that now the relative phase between the state and the homodyning quadrature is $\phi_{\text{opt}}^{\text{exp}}$.

The WGM feedback signal data was used for control during the measurements. The signal voltage could be converted to a phase shift using the WGM response calibration function. In particular, only the data within the third and fourth protocol stages was used for this purpose, since the feedback signal was on the reference level in all other stages.
The demodulated homodyne AC signal was low-pass filtered at 50 kHz before being sampled by the oscilloscope at 100 kHz. This signal was divided in a state preparation section, included in the first two protocol stages, and an optimal phase section, included in the third and fourth stages. As for the state preparation, since it took a few milliseconds for the lock to stabilize, we discarded the first part of the signal, while the rest contained the information on ϕ^*. In fact, by computing the variance of such signal we could recover the initial phase by solving Eq.(3.39) for Var [HDAC]. Using the same approach we could verify that the phase measured in the second homodyning stage was indeed the optimal phase. The main purpose of the HDAC signal, however, was the computation of the PPD, which was of fundamental importance for verifying the estimation variance scaling.
The estimation output data was mainly used for control during the estimation calibrations to test for overshoots and tune the variance scaling factors. The data within the state preparation stage was not used at all, since it only contained the reference level voltage. The estimation voltage output data found in the output hold (third stage and right after the end of the final estimation) stages was corrected for eventual remaining overshoots in the preceding iterative variance computation, then converted back to input variance using the inverted CalREst and CalFEst calibration functions, and finally converted to an estimated phase by solving the aforementioned homodyne variance expression. This was useful for testing the correct functioning of the protocol.
The FPGA trigger data was fundamental for data processing since it was used to distinguish between the different stages of the protocol. All the previously described dissections of the signals relied on the FPGA trigger level and edge distances.

As previously mentioned, we wanted to study the scaling of the estimation variance versus the energy of the probe state. Since the estimation output signal only gave information about the input phase estimate, we needed to recover its variance via post-processing computation of the PPD. To compute a PPD which was compatible with the results of the estimation, we needed to choose the right number of homodyne AC data points to use. The demodulated homodyne AC signal was low-pass filtered at 100 kHz before being sampled by the FPGA at 57 kHz to avoid correlations in the data.

Since the feedback to the optimal phase relied entirely on the FPGA operations and it depended on the result of the rough estimation, for the rough PPD we extracted from the HDAC data in the rough estimation stage a number of data points equal to the number of samples the FPGA used. However, the HDAC data was sampled by the scope, which sampled at twice the bandwidth with respect to the input state bandwidth. That was not the case for the FPGA, which sampled at slightly more than half the bandwidth. This means that the oscilloscope data contained more data points than the number used by the FPGA. We compensated by randomly selecting the correct number of samples among the larger set of data points sampled by the oscilloscope. We then used these points to calculate the rough PPD.
In turn, we calculated the final PPD using all the available HDAC data points in the final estimation section, which were more than the data points sampled by the FPGA to compute the final estimation. Moreover, to make use of all the information in the rough PPD, we rigidly shifted it, centering it on the estimated optimal phase, and then we multiplied it by the final PPD (which was centered on the optimal phase by construction) before normalizing it. This operation ensured that the variance of the final PPD was derived using the whole number of homodyne samples M_{tot}, instead of just the ones sampled during the final estimation.
We performed the data processing on 80 repetitions of the protocol for each input phase, and we finally averaged the resulting estimations and estimation variances. In this way we obtained a mean estimation and a mean estimation variance per input phase for fixed M_{tot}. By considering all the results for the same M_{tot} we studied the estimation variance curve as a function of the input phase. Else, we could average the results over all the initial phases, thus obtaining data that could be used to investigate the scaling of the estimation variance as a function of the number of samples.

3.6 Results

The results of the estimation variance for varying input phase are shown in Fig.3.17, where we plot the results from the calculation of the final PPDs variances, averaged over the 80 repetitions on each input phase. We compare the experimental results with simulated curves, obtained by generating homodyne data characterized by the same experimental parameters r, n_{th}, M_{R} and M_{F}. In the same figure is also shown the expected benchmark, *i.e.* the optimal Cramér-Rao bound (OCR) of Eq.(3.35), $(M_{\text{tot}}F(\phi^{\text{th}}_{\text{opt}}))^{-1}$, and the classical Cramér-Rao (CCR) bound $(M_{\text{tot}}F(\phi))^{-1}$.

Experiment	1	2	3	4
Experiment details				
M_{R} [samples]	68	96	136	192
M_{F} [samples]	891	1783	3569	7141
No. of Input phases	7	6	7	6 (double)
System parameters				
Squeezing strength [nat]	1.012	1.003	1.005	1.014
Squeezing [dB]	-5.747	-5.709	-5.588	-5.715
Antisqueezing [dB]	11.829	11.709	11.869	11.907
Thermalization [nat]	0.507	0.498	0.530	0.520
Relevant phases				
Squeezing [rad]	0	0	0	0
Optimal [rad]	0.131	0.1342	0.133	0.131
Vacuum [rad]	0.223	0.226	0.221	0.221
Antisqueezing [rad]	$\pi/2$	$\pi/2$	$\pi/2$	$\pi/2$

Table 3.1: **Experimental parameters during the four tests.** Each of the four experimental tests (columns) was conducted for a different total number of homodyne samples M_{tot} and it included 80 repeated measurements on each one of a number of different input phases. The state parameters, r and n_{th} were kept approximately constant during the experiment.

As expected, the non-adpative protocol follows the CCR, therefore is only optimal when the input phase is in near proximity of the optimal phase. The experimental results show a deviation from the OCR as the input phase is further away from the optimal phase. This is due to the fact that as $|\phi^* - \phi^{\mathrm{th}}_{\mathrm{opt}}|$ grows larger, the homodyining sensitivity decreases, therefore the error on the rough estimation increases. In turn this causes an increasing error on the experimental optimal phase, $\phi^{\mathrm{exp}}_{\mathrm{opt}} = \phi^{\mathrm{th}}_{\mathrm{opt}} - \delta\phi_{\mathrm{R}}$, which means that the final estimation is performed in a suboptimal homodyne sensitivity region.
To provide an additional benchmark we also compare the results with the QCR bound for a pure and a thermal coherent state characterized by the same probe energy as our squeezed thermal states. Since the quantum Fisher information only depends on the state's properties, and not on the detection strategy, such benchmarks indicate the ultimate bound on the estimation variance for *any* coherent state based phase estimation protocol. It is apparent from Fig.3.17 that our protocol outperforms such limit, especially for increasing number of samples.
Such behavior is even clearer when we average the results of each of the four tests over the corresponding input phases to study the scaling of the variance versus the total number of homodyne samples. The resulting scaling, shown in Fig.3.18, shows the expected behavior of the variance, that tends to the optimal Cramér-Rao for increasingly large number of samples. While the thermal coherent states perform definitely worse than our estimation protocol, in the pure coherent case we observe a similar scaling, especially for small numbers of samples. This is due to the fact that for small number of samples, the rough estimation is performed with very few homodyne samples. This causes a larger error on the rough estimation, which in turn determines a larger deviation of the experimental optimal phase from the theoretical one, an effect analogous to the one observed for input phases that are far from the optimal phase. The two effects compound, thus determining the suboptimal scaling observed in the low M_{tot} regime. However, as M_{tot} increases, the former effect is reduced, and we can see the experimental results progressively deviating from the pure coherent quantum Cramér-Rao bound.

3.6.1 Conclusions

In summary, we considered ab adaptive phase estimation protocol designed to asymptotically saturate the quantum Cramér-Rao limit, and we experimentally verified the suboptimal scaling due to the thermal noise in a realistic laboratory setting. However, the observed scaling still outperforms the results obtained with both pure and thermalized coherent states, demonstrating the sub-SQL perfor-

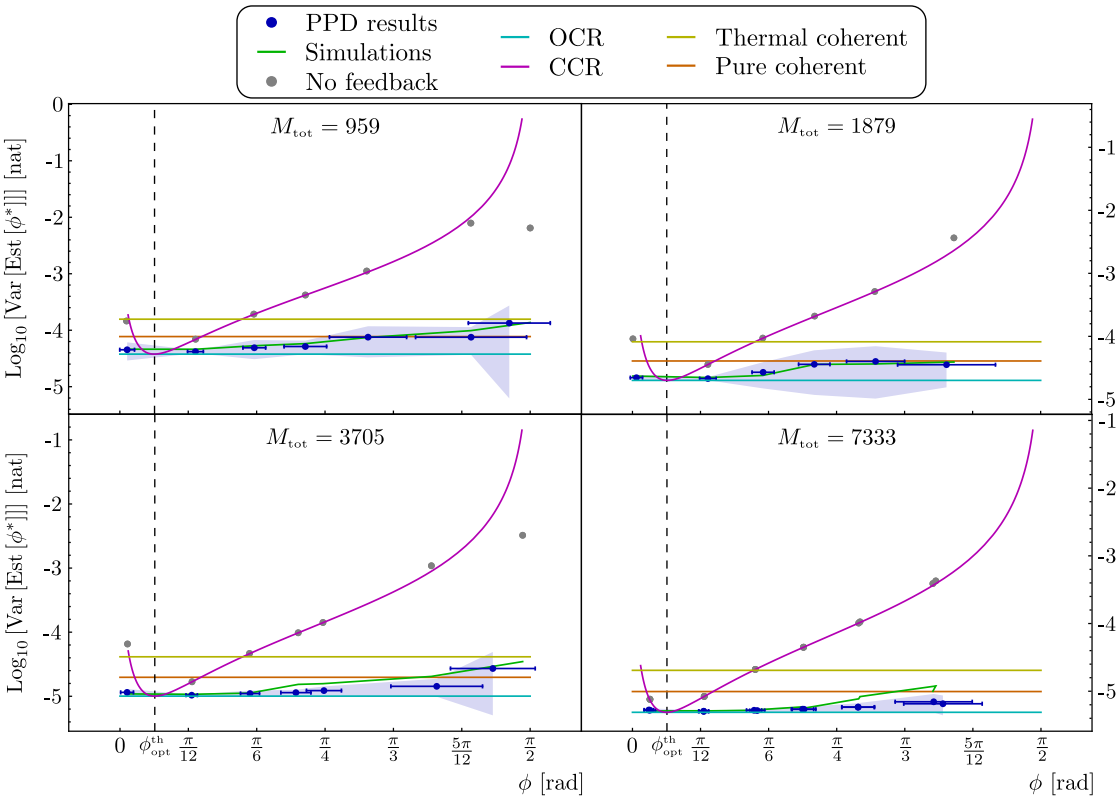

Figure 3.17: **Estimation variance versus input phase for fixed number of samples.** Each of the four figures corresponds to an experiment performed with a fixed number of samples (stated in the middle-top of each). The experimental results (blue dots) are shown, the shaded region corresponding to the standard deviation over the 80 repetitions and the horizontal error bars given by the standard deviation over the slightly varying input phases over the 80 repetitions. The results are compared with simulations for both an adaptive (green) and a non adaptive (gray dots) protocol with the same experimental parameters as the experiment. The classical Cramér-Rao bound (CCR, purple) and the optimal Cramér-Rao bound (OCR, azure) are shown. The quantum Cramér-Rao bound for a thermal (yellow) and a pure (orange) coherent states with same mean energy as our probe states are also shown. The optimal phase is indicated with a dashed vertical line.

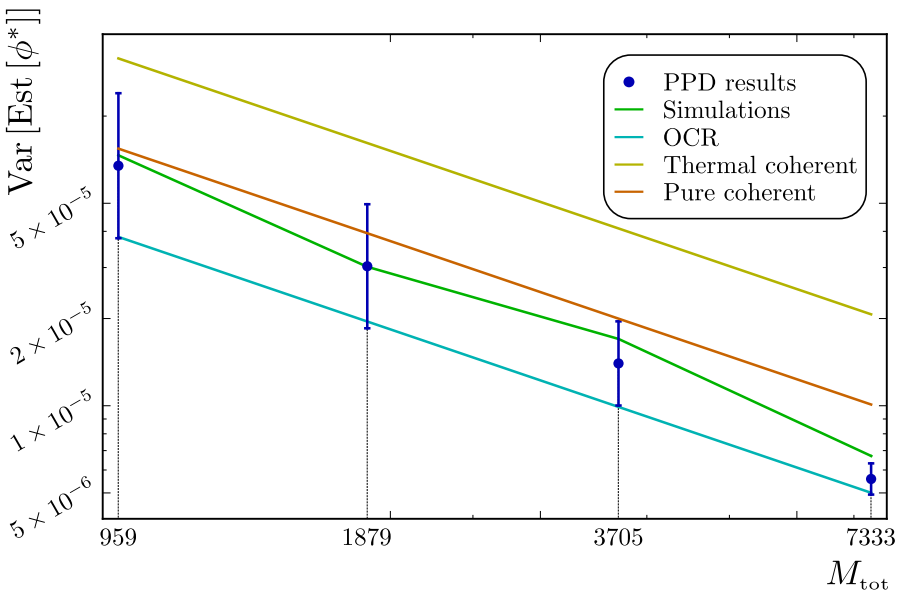

Figure 3.18: **Estimation variance versus the total number of homodyne samples.** The experimental results (blue dots) are obtained by averaging the results of each experiment over all the tested input phases. The error bars are given by the statistical error over the 80 repetitions per input phase, averaged over all the input phases in each experimental instance. We compare the results with our benchmark, the optimal Cramér-Rao bound (OCR, azure), and with a simulated experiment in which we use the same parameters that characterize the experimental test. The quantum Cramér-Rao bound for a thermal (yellow) and a pure (orange) coherent states with same mean energy as our probe states are also shown.

mance regime of the proposed phase estimation protocol. To the best of our knowledge, this is the first experimental demonstration of a phase estimation protocol which is *ab initio* and deterministic. This estimation strategy could be applied to a number of quantum metrological tasks, especially considering the recent advances in the generation of highly squeezed light. It is left to investigate how the protocol could be extended to the whole $(0, \pi]$ phase range. This could be accomplished by implementing an ulterior step to the protocol in which a small phase modulation is imposed on the state to discriminate between the two subranges $(0, \pi/2)\,, (\pi/2, \pi)$.

Chapter 4

Gaussian error correction in a correlated noisy channel

In this chapter we study noisy quantum channels, their detrimental effects on the transmission of quantum states, and ways around it. In particular, we propose an encoding/decoding strategy based on linear optical transformations which can protect arbitrary Gaussian states from Gaussian noise in correlated quantum channels [64]. We start by introducing the topic of quantum communication and motivating our investigation. Afterwards we give a general description of the problem of correction of correlated noise acting on Gaussian states, followed by its application to the case of interest. We then study two incoherent error correction strategies to use as benchmarks for the evaluation of our error correction protocol performance. We conclude with a description of our experimental test and the results we obtained for two classes of states most commonly used for quantum communication applications, *i.e.* coherent and entangled states.

4.1 Quantum communication

A communication channel is any media through which a party (a sender, commonly called Alice) can propagate physical states corresponding to predetermined symbols to a second party (the receiver, commonly called Bob). The complete set of symbols is usually referred to as an *alphabet*, and it allows for information transfer from one party to another over the communication channel. If the communication channel is suitable for supporting transmission of quantum states, then

it is called a quantum communication channel, and it can be used in junction with the quantum alphabet itself to enhance the information transfer between the communicating parties. Such enhancement can be for example the ability to securely transmit classical information from a sender to a receiver, a well known quantum information protocol known as *quantum key distribution* (QKD) [5]. A quantum communication channel might even be part of a larger quantum network [65], in which several channels connect different nodes which could be used for distributed quantum computing, or for teleporting quantum states between the nodes [66]. A quantum channel therefore allows for both direct communication by using classical coherent states, and teleportation-based communication by using entangled states. All real life implementations of quantum communication schemes need to deal with decoherence effects that arise due to the noise in the quantum channel. Noise is in general detrimental to the performance of quantum information protocols, leading to lower key rates in quantum key distribution and errors in the transmission of quantum states. Moreover, different noise sources will affect the transmission in different ways, and the combination of several strategies might be needed in order to effectively minimize decoherence in the channel. Examples of noise-reducing schemes range from noise-robust QKD protocols [67, 68, 69], to entanglement purification [70], to error correcting protocols [71, 4, 72, 73].
In particular, the protection of quantum states in a correlated noisy environment is of practical relevance. One imporant example is the non-Markovian noise introduced by a standard optical fiber as a result of guided acoustic wave Brillouin scattering (GAWBS) [74]. In such a scenario, the time scale of the noise is determined by the size of the fiber core, resulting commonly in a bandwidth around 1 GHz. In this case, for communication rates exceeding 1 GHz, consecutive pulses will contain correlated noise, which can be canceled using the error correction protocol we'll introduce in the next sections.

4.2 General treatment of Gaussian multi-channel error correction for correlated noise

While for non-Gaussian error models such as random attenuation or phase diffusion simple Gaussian operations are enough to perform error correction [75, 76, 77] or entanglement distillation [78] in CV systems, in the case of additive Gaussian noise acting on Gaussian states, it can be shown that neither entanglement distillation nor error correcting codes can be implemented by means of Gaussian operations [79, 80, 81]. In such case therefore non-Gaussian operations are required for en-

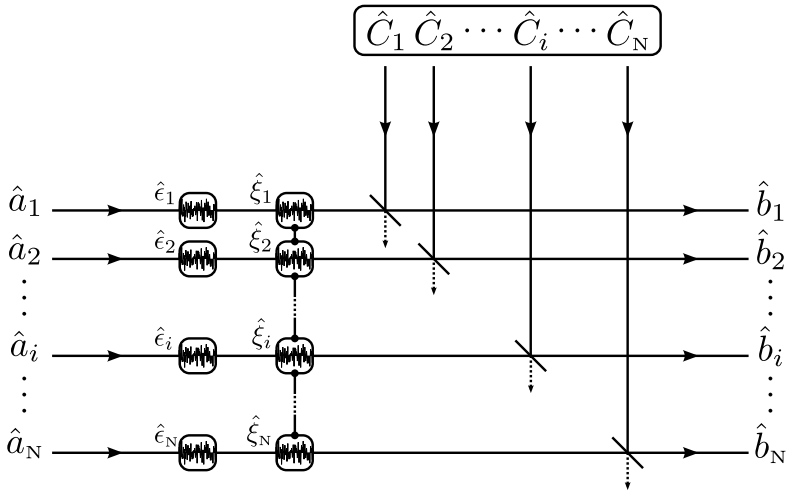

Figure 4.1: **Schematic representation of a set of N Gaussian channels.** The input modes for the i-th channel $\hat{a}_i$ are subject to uncorrelated noise $\hat{\epsilon}_i$, to correlated noise $\hat{\xi}_i$ and to classical interaction with correlated environmental modes $\hat{C}_i$, which is modeled as a beam splitter interaction that includes both additive environmental noise and losses in the channel.

abling fault-tolerant quantum communication [82, 83]. Interestingly, the no-go theorem that prevents Gaussian error correction of Gaussian noise, does not apply when the noise is correlated, an inevitable feature of most contemporary communication channels [84, 85]. Recent theoretical studies address correlated noise in bosonic channels using the decoherence-free-subspace framework [86, 87, 88].

We start by deriving a sufficient condition for the complete elimination of correlated Gaussian noise, which in turn does nott affect uncorrelated noise and attenuation in the channels.

Let us consider a set of N Gaussian phase-insensitive lossy channels connecting two communicating parties (cfr. Fig.4.1). To emphasize the universality of the error correcting scheme, we conduct the following derivation in the Heisenberg picture. In lossy and noisy Gaussian channels, the output annihilation operator $\hat{b}_i$ of the i-th channel is obtained as

$$\hat{b}_i = \sum_j G_{ij}\hat{a}_j + \hat{\epsilon}_i + \hat{\xi}_i, \tag{4.1}$$

where $\hat{a}_j$ is the input annihilation operator for the j-th channel and G_{ij} is a matrix describing the channel transmittances and the crosstalk between the channels. The $\hat{\epsilon}_i$ are operators representing completely uncorrelated noise in the i-th channel, which can be characterized by the mean values $\langle\hat{\epsilon}_i^\dagger\hat{\epsilon}_i\rangle$. The $\hat{\xi}_i$ are operators representing the ideally correlated noise of the channels. The mixture of correlated and uncorrelated noise corresponds to a partial correlation of environmental noise. The

channels are passively coupled to a collection of correlated environmental modes, C_i, and the transmittances of this coupling are included into G_{ij}. Coupling of the channels with the environmental modes can be modeled as a beam splitter interaction. If the environmental mode C_i is in the vacuum state, then the particular channel introduces only loss and uncorrelated noise. Any Gaussian multi-mode correlated classical noise can be written as $\hat{\xi}_i = \sum_k C_{ik}\hat{\xi}_k^0$, where C_{ik} represents a matrix of both orthogonal and symplectic transformations and $\hat{\xi}_k^0$ are the operators of uncorrelated noise in the factorized vacuum modes C_i^0. A mixture of the contributions of both the completely uncorrelated and ideally correlated noise models can be used to describe a variety of realistic Gaussian lossy and noisy channels.
As an example, we can take the first channel $\hat{b}_1 = G_{11}\hat{a}_1 + \hat{\epsilon}_1 + \hat{\xi}_1^0$ as the one with least uncorrelated noise. We want to eliminate the correlated noise without changing the transmission G_{11} and without increasing the uncorrelated noise contribution. We start by defining two unitary Gaussian multi-mode operations $\hat{U}$ and $\hat{V}$, acting on the channel's input and output modes, respectively. These operations may be described by the linear transformations

$$\begin{aligned} \hat{a}_i &= \sum_k U_{ik}\hat{a}_k \,, \\ \hat{b}_i &= \sum_k V_{ik}\hat{b}_k \,. \end{aligned} \tag{4.2}$$

After the application of $\hat{U}$ and $\hat{V}$ the transformation of Eq.(4.1) reads

$$\hat{b}_i = \sum_{j,k,l} V_{ij}G_{jk}U_{kl}\hat{a}_l + \sum_j V_{ij}\hat{\epsilon}_j + \sum_{j,m} V_{ij}C_{jm}\hat{\xi}_m^0 \,. \tag{4.3}$$

We notice that we can eliminate the correlated noise by setting the Gaussian transformation $\hat{V}$ as $V_{ij} = C_{jm}^{-1}$. Indeed, applying such transformation to the first channel leads to

$$\hat{b}_1 = \sum_{j,k,l} C_{1j}^{-1}G_{jk}U_{kl}\hat{a}_l + \sum_j C_{1j}^{-1}\hat{\epsilon}_j + \hat{\xi}_1^0 \,, \tag{4.4}$$

where the correlation process is noticeably fully reversed. Ideally, the remaining contribution from $\hat{\xi}_1^0$ only compensates a loss caused by the coupling to the environmental modes C_j. However, the transformation C_{1j}^{-1} mixes the channels in the first term and it also combines the operators $\hat{\epsilon}_j$ of uncorrelated noise in the second term. Both mixing effects can be detrimental and thus the resulting channel might actually be more noisy than the original one. Nevertheless, we can find a sufficient condition on the type of multi-mode channel for which both negative mixing effects do not occur. If the crosstalk is solely introduced by the unitary

Gaussian transformation, by optimizing U_{kl} to fulfill $\sum_{j,k} C_{1j}^{-1} G_{jk} U_{k1} = G_{11}$ we can eliminate both the unitary crosstalk and the correlated noise. For identical lossy channels without crosstalk, the transmittances are $G_{jk} = G\delta_{kj}$, where $0 \leq G \leq 1$ and $\langle \hat{\epsilon}_k^\dagger \hat{\epsilon}_j \rangle = \langle \hat{\epsilon}^\dagger \hat{\epsilon} \rangle \delta_{kj}$. In this case, by the setting $U_{kl} = C_{kl}$ for the input unitary encoding, we reach $\sum_{j,k} C_{ij}^{-1} (G\delta_{jk}) U_{kl} = G\delta_{il}$ and the transmissions are not changed by the error correcting scheme. On the other hand, to eliminate the negative contribution from the second term, we set conditions on the structure of the correlated noise described by the matrix C_{jm}. If C_{jm} corresponds to a common passive beam splitter type interaction of the environmental vacuum mode C_j^0, it satisfies $\sum_i C_{si}^{-1*} C_{im}^{-1} = \delta_{sm}$. In this case, the correlated noise produced by the channels is fully classical and it can be represented by a classical mixture of coherent states. It is a common case, since nonclassical states are not likely to survive in the environment. Since $\sum_{s,i,m} \langle \hat{\epsilon}_s^\dagger C_{si}^{-1*} C_{im}^{-1} \hat{\epsilon}_m \rangle = \sum_m \langle \hat{\epsilon}_m^\dagger \hat{\epsilon}_m \rangle$ for any mode m, where C_{si}^{-1*} is the Hermitian conjugate of C_{si}^{-1}, the amount of uncorrelated noise remains unchanged.
In summary, if all the couplings in the identical lossy and noisy Gaussian channels are of the unitary, passive beam-splitter type, it is possible to completely eliminate the correlated noise (including crosstalk) and thus reach the optimal single mode channel by the coherent error correction scheme.

4.2.1 Two-channel protocol

We may now apply the results of the previous section to a system composed of two identical channels with partially correlated noise, and show that such a system is sufficient for the complete elimination of the correlated noise without degradation of the transmitted quantum state. Applying Eq.(4.1) to this scenario yields

$$\begin{pmatrix} \hat{b}_1 \\ \hat{b}_2 \end{pmatrix} = \begin{pmatrix} \sqrt{\eta_1}\hat{a}_1 + \sqrt{\eta_{1\mathrm{N}}(1-\eta_1)}\hat{v}_1 + \sqrt{(1-\eta_1)(1-\eta_{1\mathrm{N}})}\left(\sqrt{g}\hat{v}_c - \sqrt{1-g}\hat{v}_0\right) \\ \sqrt{\eta_2}\hat{a}_2 + \sqrt{\eta_{2\mathrm{N}}(1-\eta_2)}\hat{v}_2 + \sqrt{(1-\eta_2)(1-\eta_{2\mathrm{N}})}\left(\sqrt{1-g}\hat{v}_c + \sqrt{g}\hat{v}_0\right) \end{pmatrix}. \tag{4.5}$$

Here the attenuation in each channel is modeled by the channel transmissions $\eta_i \in [0,1]$, which form a diagonal matrix $G_{ij} = \mathrm{Diag}\,[\eta_1, \eta_2]$. The uncorrelated noise operators $\hat{\epsilon}_1$ and $\hat{\epsilon}_2$ are explicitly expressed in the second terms as $\sqrt{\eta_{iN}(1-\eta_i)}\hat{v}_i$. Finally, the third terms are explicit forms of the operators $\hat{\xi}_1$ and $\hat{\xi}_2$ associated with the perfectly correlated noise contributions, with the annihilation operator $\hat{v}_c$ corresponding to an environmental mode causing perfectly correlated noise between the two channels, and the annihilation operator $\hat{v}_0$ corresponding to a vacuum mode.

Following our general approach from the previous section, for symmetric attenuation $\eta_1 = \eta_2$, symmetric uncorrelated noise $\eta_{1N} = \eta_{2N}$ and $\langle \hat{v}_1^\dagger \hat{v}_1 \rangle = \langle \hat{v}_2^\dagger \hat{v}_2 \rangle$, we can easily prove that the mode C (representing a source of correlated noise) can be completely eliminated by our method and only residual attenuation arising from the coupling to operators $\hat{v}_0$ of the vacuum mode 0 remains. In the experiment we assume a practical limit of weak symmetric coupling of strong correlated noise, which means $\eta_{1N} = \eta_{2N} \to 1$, implemented experimentally with a 99 : 1 beam splitter. Moreover, the Gaussian noise in mode C is assumed to be large compared to the vacuum noise in mode 0. Under such assumptions, the input-output relations approach two channels with purely additive classical noise

$$\begin{pmatrix} \hat{b}_1 \\ \hat{b}_2 \end{pmatrix} = \begin{pmatrix} \sqrt{\eta_1}\hat{a}_1 + \sqrt{1-\eta_1}\hat{v}_1 + \sqrt{g_1}v_c \\ \sqrt{\eta_2}\hat{a}_2 + \sqrt{1-\eta_2}\hat{v}_2 + \sqrt{g_2}v_c \end{pmatrix} . \tag{4.6}$$

Here, the second terms $\sqrt{1-\eta_i}\hat{v}_i$ are simplified forms of the noise operators associated with the uncorrelated noise, while the third terms $\sqrt{g_i}v_c$ are explicit forms of the complex random variables of classical additive noise associated with the perfectly correlated noise, whose magnitudes are given by the positive factors g_1 and g_2. The noise correction stategy we apply is depicted in Fig.4.2. The channel input modes are prepared by mixing the input signal $\hat{a}_{\text{in}}$ with an auxiliary vacuum state $\hat{a}_{\text{aux}}$ on the encoding beam splitter, characterized by a transmissivity T_{e}. The mixing is followed by a relative π phase shift between the two output modes. The encoding transformation can thus be written as

$$\begin{pmatrix} \hat{a}_1 \\ \hat{a}_2 \end{pmatrix} = \begin{pmatrix} \sqrt{T_{\text{e}}}\hat{a}_{\text{in}} - \sqrt{1-T_{\text{e}}}\hat{a}_{\text{aux}} \\ -\sqrt{1-T_{\text{e}}}\hat{a}_{\text{in}} - \sqrt{T_{\text{e}}}\hat{a}_{\text{aux}} \end{pmatrix} . \tag{4.7}$$

In turn, the decoding transformation is the reverse of the encoding one

$$\begin{pmatrix} \hat{b}_{\text{out}} \\ \hat{b}_{\text{aux}} \end{pmatrix} = \begin{pmatrix} \sqrt{T_{\text{d}}}\hat{b}_1 - \sqrt{1-T_{\text{d}}}\hat{b}_2 \\ -\sqrt{1-T_{\text{d}}}\hat{b}_1 - \sqrt{T_{\text{d}}}\hat{b}_2 \end{pmatrix} . \tag{4.8}$$

Now we can put together Eq.(4.8), Eq.(4.6) and Eq.(4.7) to obtain the overall input-output relation for contructive interference of the signal channel

$$\begin{aligned} \hat{b}_{\text{out}} = & \left(\sqrt{T_{\text{d}}T_{\text{e}}\eta_1} + \sqrt{(1-T_{\text{d}})(1-T_{\text{e}})\eta_2}\right)\hat{a}_{\text{in}} + \\ & + \left(\sqrt{(1-T_{\text{d}})T_{\text{e}}\eta_2} - \sqrt{T_{\text{d}}(1-T_{\text{e}})\eta_1}\right)\hat{a}_{\text{aux}} + \\ & + \sqrt{T_{\text{d}}(1-\eta_1)}\hat{v}_1 - \sqrt{(1-T_{\text{d}})(1-\eta_2)}\hat{v}_2 + \\ & + \left(\sqrt{T_{\text{d}}g_1} - \sqrt{(1-T_{\text{d}})g_2}\right)v_c . \end{aligned} \tag{4.9}$$

Now to completely eliminate the correlated noise we may set $T_{\rm d} = g_2/(g_1+g_2)$, and to avoid the noise impact from the operator $\hat{a}_{aux}$ introduced by the encoding, we set $T_{\rm e} = \eta_1 g_2/(\eta_1 g_2 + \eta_2 g_1)$. The resulting input-output relation therefore becomes

$$\hat{b}_{\rm out} = \sqrt{\frac{\eta_1 g_2 + \eta_2 g_1}{g_1+g_2}}\hat{a}_{\rm in} + \sqrt{\frac{g_2(1-\eta_1)}{g_1+g_2}}\hat{v}_1 - \sqrt{\frac{g_1(1-\eta_2)}{g_1+g_2}}\hat{v}_2\,, \tag{4.10}$$

where the transmission $G' = (\eta_1 g_2 + \eta_2 g_1)/(g_1+g_2)$ satisfies $\min[\eta_1,\eta_2] \leq G' \leq \max[\eta_1,\eta_2]$ and, together with the mean number of photons of the uncorrelated noise

$$\langle \hat{\epsilon}_1'^{\dagger}\hat{\epsilon}_1'\rangle = \frac{g_2}{g_1+g_2}(1-\eta_1)\langle \hat{v}_1^{\dagger}\hat{v}_1\rangle + \frac{g_1}{g_1+g_2}(1-\eta_2)\langle \hat{v}_2^{\dagger}v_2\rangle\,, \tag{4.11}$$

determines the quality of the output channel: $\hat{b}_{\rm out} = \sqrt{G'}\hat{a}_{\rm in} + \hat{\epsilon}_1'$.
We emphasize that for purely lossy channels with $\langle \hat{\epsilon}_i^{\dagger}\hat{\epsilon}_i\rangle = 0$ $(i=1,2)$, the error correcting scheme does not add any excess noise to the state, regardless of the values of η_1 and η_2. On the other hand for noisy channels, *i.e.* $\langle \hat{\epsilon}_i^{\dagger}\hat{\epsilon}_i\rangle \neq 0$ $(i=1,2)$, two identical channels with $\eta_1 = \eta_2 = \eta$ and $\langle \hat{\epsilon}_1^{\dagger}\hat{\epsilon}_1\rangle = \langle \hat{\epsilon}_2^{\dagger}\hat{\epsilon}_2\rangle = \langle \hat{\epsilon}^{\dagger}\hat{\epsilon}\rangle$ are sufficient to obtain a perfectly corrected channel with a complete elimination of the correlated noise, unaffected transmission (that is $G' = \eta$) and unaffected uncorrelated noise. The coherent encoding and decoding scheme is thus fully capable of correcting for all correlated noise of the channels.
It is important to note that such an error correction protocol is universal, *i.e.* it is valid for any input quantum state and for any statistics of the correlated noise.

4.3 Incoherent error-correction strategies

In order to verify the performance of our error correction protocol, we compare it to a fully incoherent protocol where one of the channels is directly measured and subsequently used to correct the other channel [89]. Such a strategy does not use coherent interactions at the encoding and decoding stations but instead uses a direct measurement of a probe state to detect the correlated noise and apply the gained information to correct the signal (cfr Fig.4.3). In the simplest case of two identical lossless ($\eta_1 = \eta_2 = 1$) additive channels, we obtain for the output modes

$$\begin{pmatrix} \hat{b}_1 \\ \hat{b}_2 \end{pmatrix} = \begin{pmatrix} \hat{a}_1 + \sqrt{g_1}v_c \\ \hat{a}_2 + \sqrt{g_2}v_c \end{pmatrix}\,, \tag{4.12}$$

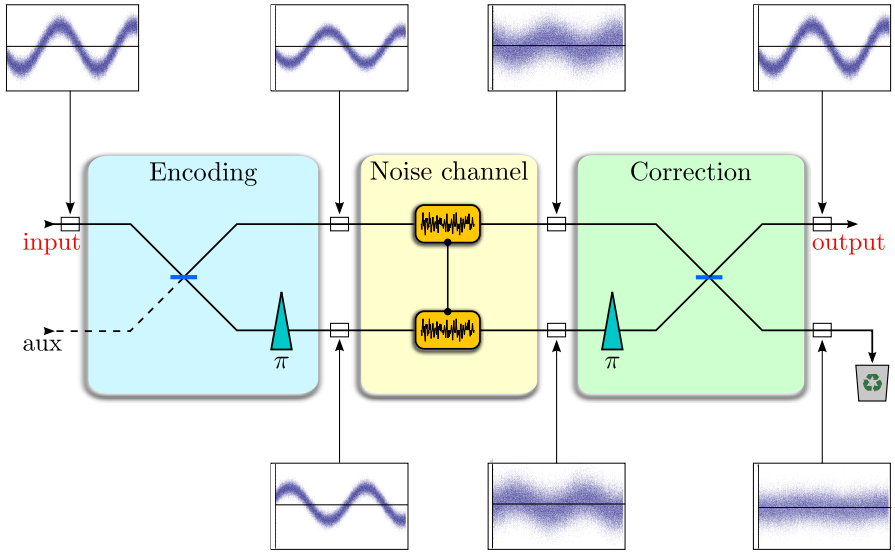

Figure 4.2: **Schematic representation of the error correction protocol.** The protocol is divided in three main stages associated with encoding, noisy transmission and decoding. The insets illustrate the working principle of the correction scheme applied on a coherent state. From top left to top right: a coherent state is mixed with an auxiliary mode on a balanced beam splitter; A π phase shift is imposed on one of the beam splitter output modes before they enter the noisy channel; The two modes are transmitted through the noisy channel, where they are polluted by correlated Gaussian excess noise; another π phase shift is applied on the same mode; a second mixing of the two modes on a beam splitter provides separation of the excess noise from the signal.

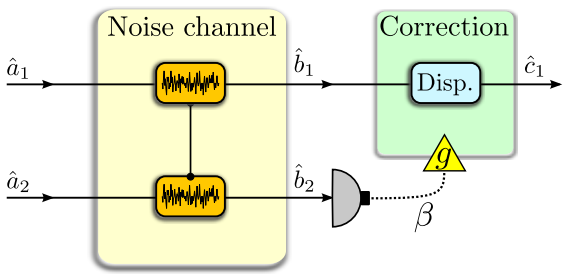

Figure 4.3: **Schematic representation of the incoherent strategy.** Here $\hat{a}_1$ represent the signal, while $\hat{a}_2$ is the probe. The measurement of $\hat{b}_2$ by heterodyne detection results in a number β which is used to displace $\hat{b}_1$.

where $\hat{a}_1$ is the signal and $\hat{a}_2$ is the auxiliary probe, which does not contain information. Performing an optimal heterodyne measurement on the second mode $\hat{b}_2$ results in the outcome $\beta = \hat{b}_2 + \hat{v}_0^\dagger$, where $\hat{v}_0^\dagger$ is the heterodyne vacuum noise contribution. β is used for the feed-forward correction of the remaining mode as

$$\hat{a}_1 \to \hat{c}_1 = \hat{b}_1 - \sqrt{g}\beta = \hat{a}_1 - \sqrt{g}\hat{a}_2 + (\sqrt{g_1} - \sqrt{gg_2})v_c - \sqrt{g}\hat{v}_0^\dagger \,. \tag{4.13}$$

By chosing a proper value of the feedforward gain g, it is possible to reduce the noise added to the signal mode. In the following, we consider two different strategies for incoherent error correction: a first approach requiring the constraint that g should be independent on the amount of added correlated noise, and a second one in which such constraint is relaxed.

The first approach is straightforward from Eq.(4.13): the correlated noise can be universally eliminated by setting $g = g_1/g_2$. The price to pay is the addition of the uncorrelated additive noise from mode 2 associated with the heterodyne measurement

$$\hat{c}_1 = \hat{a}_1 - \sqrt{\frac{g_1}{g_2}}(\hat{a}_2 + \hat{v}_0^\dagger) = \hat{a}_1 - \hat{\epsilon}_1' \,. \tag{4.14}$$

Clearly, it is better to measure the channel with the larger noise amplitude and correct the channel with the smaller noise amplitude, a choice that leads to $g_1 < g_2$ and the least amount of added uncorrelated noise. We can quantify the mean photon number of the remaining noise in the $\hat{c}_1$ mode as $\langle \hat{\epsilon}_1'^\dagger \hat{\epsilon}_1' \rangle = g_1/g_2$, and observe that this is negligible only for very asymmetrical channels with $g_1 \ll g_2$. Equivalently, the added noise can be quantified in terms of the variance

$$\Delta V_{\text{uni}} = \langle \Delta \hat{X}^2 \rangle = 2\frac{g_1}{g_2} \,. \tag{4.15}$$

For the worst case of symmetric channels ($g_1 = g_2$) the classical benchmark is given by two units of vacuum noise, $\Delta V_{\text{uni}} = 2$, one unit stemming from the probe mode and the second unit due to the noise penalty in estimating conjugate quadratures in the heterodyne detector.

As a second approach we relax the universality condition, thereby further reducing the added noise of the signal mode. By optimizing the feed-forward gain to minimize the additive noise contribution, we find $g = (g_1 g_2 V_c^2)/(2 + g_2 V_c)^2$ which depends on the added noise $V_c = \langle \Delta X_c^2 \rangle$. The resulting minimized quadrature variance of the added noise therefore reads

$$\Delta V_{\text{opt}} = \frac{2 g_1 V_C}{2 + g_2 V_C} \,, \tag{4.16}$$

which is in general lower than ΔV_{uni}, in particular for small V_c. However, even for very small V_c, the optimized threshold $\Delta V_{\text{opt}} < g_1 V_c$ does not vanish for any

$V_c > 0$. For large $g_2 V_c \gg 2$, the classical benchmark ΔV_{opt} approaches ΔV_{uni}. Therefore, even with perfectly correlated noise and optimized classical strategy, it is not possible to completely error correct the state using the incoherent strategy. Optimal error correction in a correlated noisy channel can only be performed by the collective encoding and decoding operations. As our coherent protocol is universal (*i.e.* it does not depend on the amount of added noise V_c), the universal incoherent strategy in Eq.(4.15) will serve as the incoherent benchmark in the analysis of the correction protocol performance.
In the following we introduce the experimental realization of the protocol, which was used to test the protocol's performance for coherent and CV entangled input states in a correlated Gaussian noisy environment.

4.4 Experiment

A diagram of our error correction protocol is shown in Fig.4.2 for the case of two partially correlated channels with classical noise. Such scenario could represent either two spatially separated channels with spatial correlations or two consecutive uses of the same channel with temporal correlations (non-Markovian channel). The experimental setup is shown in Fig.4.4 and consists of four different stages: encoding of the signal states; transmission of the signal through a noisy channel; separation of the noise from the signal; verification of the signals. Our light source was a continuous-wave Nd:YAG laser, which produced horizontally polarized light at 1064 nm. An internal second harmonic generator provided green light at 532 nm. Spatial and spectral quality of both the IR and the green light were enforced by mode cleaning cavities locked to the respective resonant frequencies by means of Pound-Drever-Hall (PDH) locking schemes [61]. All our states were generated at a sideband frequency of 4.9 MHz.
The noisy channel was simulated as a beam splitter interaction in which the signal was mixed with a thermal state generated using amplitude and phase modulators. The quantum interference at the beam splitter was characterized to have a visibility of 98%. We drove the modulators using two function generators which provided white noise with a bandwidth much larger than our states bandwidth. A wide range of modulation amplitudes allowed us to study the correction efficiency of the protocol with noise variances ranging from from 0 to more than 100 shot noise units.
We realized the two channels in two orthogonal polarization modes, thereby simulating correlated polarization noise. The protocol was implemented as follows:

first of all the states were sent on a balanced beam splitter, which sended one of the outputs to homodyne detector 1 for control, while the other was transmitted through a half wave plate (HWP1), which was set to $-22.5°$ with respect to the horizontal polarization of our laser. The polarization state of the signal beam was therefore rotated from horizontal to anti-diagonal ($-45°$), with the vertical component's phase delayed of π with respect to the horizontal

$$\hat{a}_H \to \frac{1}{\sqrt{2}} \left(\hat{a}_H - \hat{a}_V \right) , \tag{4.17}$$

where $\hat{a}$ is the mode operator of the signal state and the subscripts H and V indicate the polarization state. The beam then entered a 99/1 beam splitter where it was mixed with the thermal state, simulating the transmission through a noisy channel. In order to add the noise on both the polarization modes of the signal, the thermal state was itself rotated from horizontal to diagonal ($+45°$) polarization by a half wave plate (HWP2) placed before the 99/1 beam splitter, with the fast axis set to $+22.5°$ with respect to the horizontal

$$\hat{b}_H \to \frac{1}{\sqrt{2}} \left(\hat{b}_H + \hat{b}_V \right) , \tag{4.18}$$

where $\hat{b}$ is the thermal state mode operator. By detecting directly the beam splitter output beams we could verify that the noise was added to the signal. By changing the position of HWP2 we could set the noise correlation from completely correlated to asymmetrically correlated.
After the beam splitter simulating the noise channel, another half wave plate (HWP3) was placed, which was set to $+22.5°$ with respect to the horizontal. This rotated the signal to the horizontal and the noise to the vertical polarization according to

$$\frac{1}{\sqrt{2}} \left(\hat{a}_H - \hat{a}_V + \hat{b}_H + \hat{b}_V \right) \to \hat{a}_H + \hat{b}_V \, . \tag{4.19}$$

The actual separation of the signal from the noise, which now were in orthogonal polarization modes, was easily performed by a polarizing beam splitter which transmitted the horizontally polarized signal and reflected the vertically polarized noise. The two outputs finally reached homodyne stations 2 and 3, in which they were detected and the error correction verified.
We used six broadband amplified InGaAs pin-diode detectors to set up three homodyne detectors. The respective total detection efficiencies of the homodyne detectors were $90\% \pm 2\%$, $90\% \pm 2\%$ and $85\% \pm 2\%$. The visibility was more than 98% on each detector and we had 18 dB of clearance between shot noise and electronic noise. The detectors' AC outputs were subtracted two-by-two and

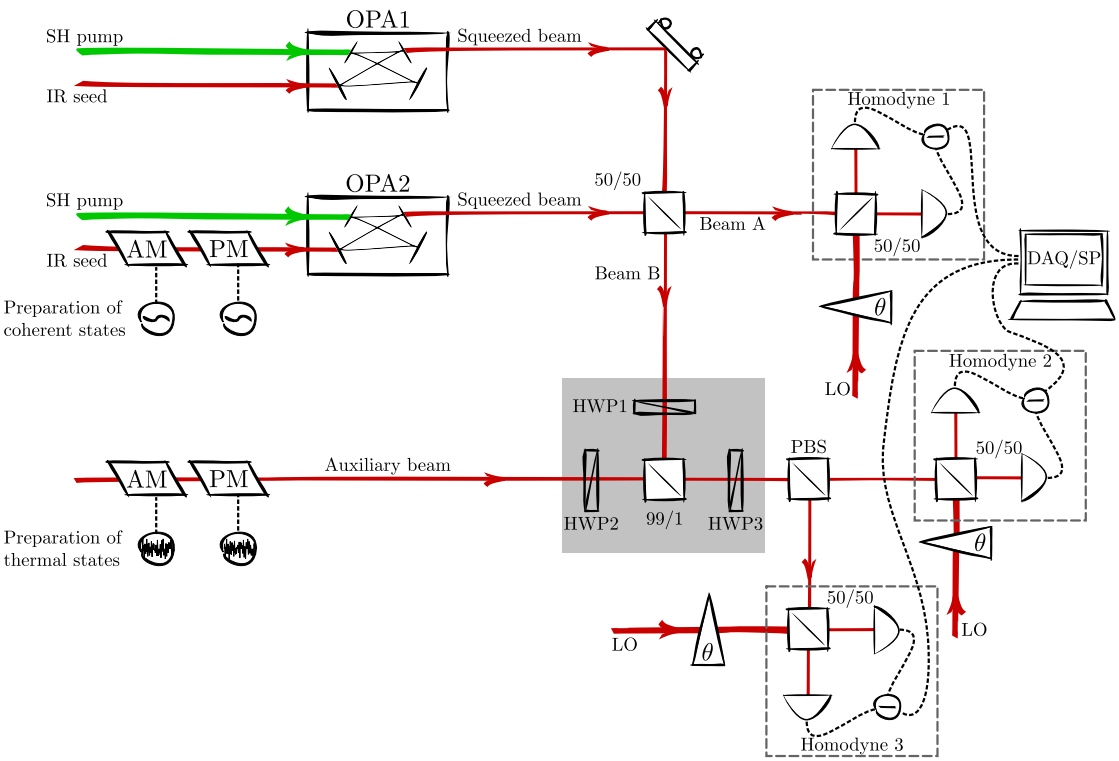

Figure 4.4: **Schematic of the experimental setup.** SH pump: second harmonic pump; IR seed: infrared seed; OPA: optical parametric amplifier; AM/PM: amplitude/phase modulator; 50/50: balanced beam splitter; 99/1: non balanced beam splitter; HWP: half wave plate; PBS: polarizing beam splitter; LO: local oscillator; DAQ/SP: data acquisition/signal processing.

then mixed down using a 4.9 MHz electronic local oscillator with a bandwidth of 100 kHz before being digitized by a data acquisition card with 14 bit resolution at 5×10^5 samples/sec. Since our states were Gaussian and were only subject to Gaussian operations, post processing of the data mainly consisted of normalization to shot noise and extraction of the variances from the time traces, which were used to characterize the performance of the protocol.

4.5 Results

Testing the protocol with coherent states required the output of OPA1 to be blockes and OPA2 to be offline while its seed was coherently modulated with an amplitude and a phase modulator to generate the signal. A quantitative study of the cancellation of excess noise is presented in Fig.4.5 for coherent states, where we plot

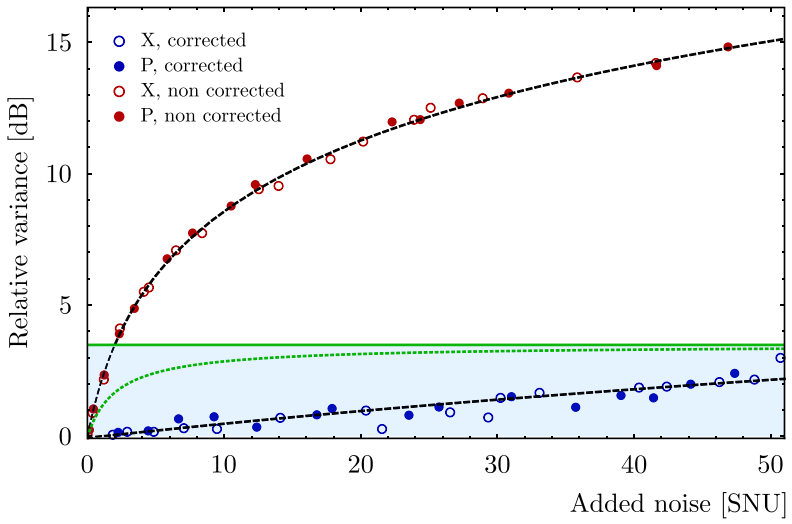

Figure 4.5: **Demonstration of error correction on a choerent state in an extremely noisy environment.** The relative noise variance of the quantum state, normalized to shot noise, is plotted against the channel excess noise for the case of slightly asymmetrically correlated noise, with a ratio $g_1/g_2 = 0.61$. Amplitude and phase quadrature measurements are represented by open and closed circles, respectively. The results before (red) and after (blue) correction are shown, where the non-corrected quantum states were measured with the transmittance of the decoding beam spplitter set to $T_\mathrm{d} = 1$ (no decoding) and the corrected ones were measured with $T_\mathrm{d} = 0.36$. Dashed black lines represent the theoretical predictions, and include a 1% mismatch of the modes at the decoding beam splitter. The solid and dotted green lines correspond to the two incoherent strategies. In particular, the solid green line represents our benchmark, since in that case the *a priori* channel information is similar to that needed for implementing the coherent strategy. The shaded region indicates where the classical strategy is beaten by our protocol. The statistical error bars are smaller than the dots.

the measured quadrature noise for both $\hat{x}$ and $\hat{p}$ versus the added noise with and without correction protocol. Clearly, application of the error correction scheme results in the elimination of most of the added noise for both quadratures. Moreover, it is apparent that both incoherent correction strategies are outperformed by our proposed scheme, for all the values of the added noise. As shown in Fig.4.6, also the fidelity of the input signal with the corrected output is consistently higher than the one obtained without error correction. To test the error correction in the context of a teleportation channel we used continuous variable entangled states, *i.e.* , two-mode squeezed states. In this scenario both OPAs were online, and their single mode-squeezing outputs were interfered at a balanced beam splitter with orthogonal squeezing quadratures. One of the beam splitter output modes was directly measured at the homodyning station 1, while the other output mode was sent to the encoding station, where it was mixed with the auxiliary mode, there-

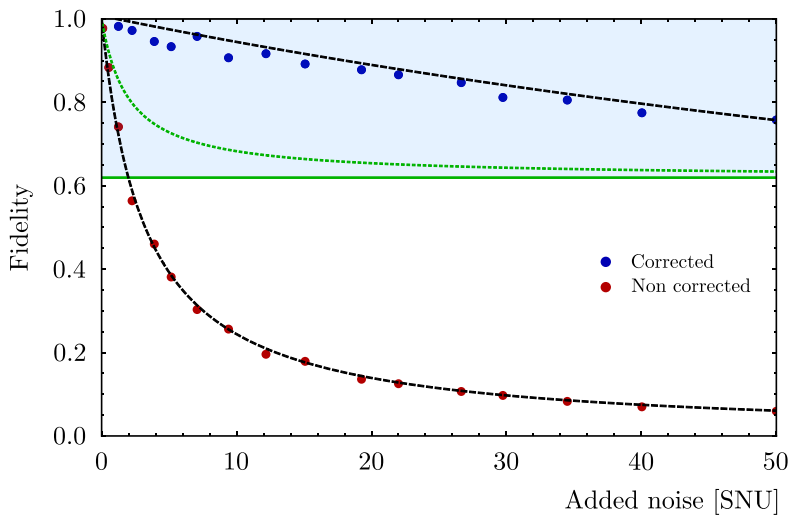

Figure 4.6: **Fidelity between the input coherent state and the output corrected and non-corrected states.** Dashed lines represent the theoretical predictions, while the solid and dotted green lines correspond to the two incoherent strategies. The shaded region indicates where the classical strategy is beaten by our protocol. The statistical error bars are smaller than the dots.

fore simulating the correlated noise channel (see Fig.4.4). With this setup it was possible to compute the correlations between mode A and mode B in terms of the variances of the joint quadratures $\langle(\hat{x}_{\mathrm{A}}-\hat{x}_{\mathrm{B}})^2\rangle$ and $\langle(\hat{p}_{\mathrm{A}}+\hat{p}_{\mathrm{B}})^2\rangle$, which we could use to verify the presence of entanglement. Specifically, according to the inseparability criterion [90, 91], entanglement is present if $\langle(\hat{x}_{\mathrm{A}}-\hat{x}_{\mathrm{B}})^2\rangle+\langle(\hat{p}_{\mathrm{A}}+\hat{p}_{\mathrm{B}})^2\rangle<2$. We show the results of such measurements in Fig.4.7, where the computed inseparability of modes A and B is plotted against the added noise. In the plot, a vertical dashed line represents the entanglement breaking point, which is the amount of added noise (2 SNU) for which a channel can no longer be used for entanglement distribution. As clearly showed in the plot, our proposed error correction protocol allows us to use the dual channel for deterministic entanglement distribution for up to ~ 35 SNU of excess noise. In addition to proving the channel's capability of transmitting entangled states, the results also indicate that our scheme is universal: since a CV entangled state can be used to prepare an arbitrary state via state projection, the survival of entanglement unambiguously proves the faithful transmission of a generalized state.

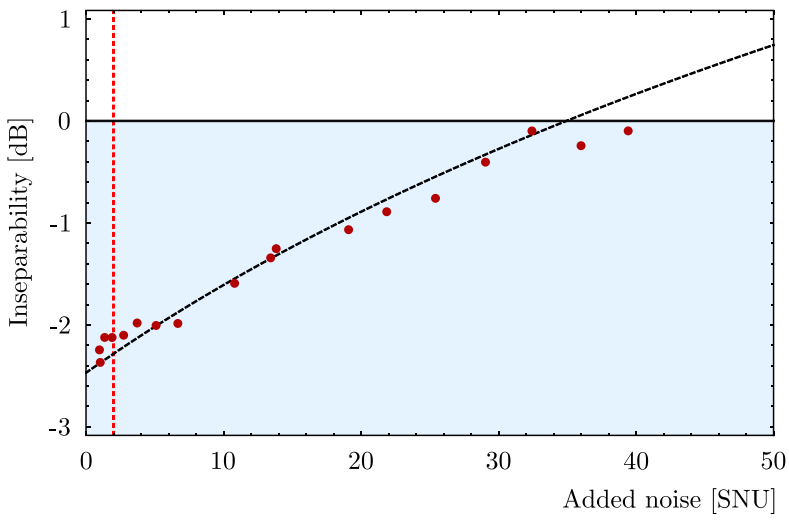

Figure 4.7: **Error correction of CV entangled states in an extremely noisy and symmetric channel.** Here we show the inseparability versus the added noise, normalized to shot noise (black solid line). The vertical red dashed line represents the entanglement breaking noise in absence of error correction, while the shaded region indicates presence of entanglement. The theoretical prediction is displayed as a dashed black curve, and it takes into account a 1% mode mismatch at the decoding beam splitter, which is the reason why the two-mode squeezing variance increases with the added noise. The statistical error bars are smaller than the dots.

4.6 Conclusions

We proposed a universal scheme for protection of arbitrary quantum states in a noisy non-Markovian environment. We implemented experimentally the error correction scheme using both coherent and entangled states to test its performance in both direct and teleportation-based communication, demonstrating near-ideal recovery of pure quantum states from a highly noisy environment. The main error source in the experiment was the imperfect mode matching at the encoding beam splitter, where the signals were mixed to the auxiliary modes. Such mismatch of the modes implies the presence of residual excess noise which was not corrected, as apparent from Fig.4.5, Fig.4.6 and Fig.4.7. Despite such imperfection in the experimental implementation of the correction scheme, we still show transmission of quantum states to a degree that allows for the generation of a secure key and the implementation of quantum teleportation.

Chapter 5

Quantum discord in an open system

In this chapter we discuss the concept of quantum correlations and we present experimental results aimed at investigating the robustness of a relatively novel quantifier for purely quantum correlations, namely the quantum discord, when subject to dissipative dynamics. We start introducing the framework and mathematical tools used to quantify the physical information encoded in quantum systems, introducing the notion of quantum discord. Then we move on to describe how the discord content of a quantum state, for which is in general difficult to obtain closed expressions, can be analytically calculated provided that the state is Gaussian and it undergoes Gaussian transformations and measurements. Finally, we introduce the experiment and describe the results we obtained.

5.1 Measuring information

The most common way to measure the information content of a quantum system derives from the entropic measure defined by Shannon in [92]. Indeed, being entropy itself a measure of the disorder of a system, it quantifies the degree of our uncertainty about the system's state. When we measure the system we gain information about its state, and such information gain corresponds to the decrease of entropy of the system.
Let's consider a system described by a random variable A whose values $\{a\}$ are distributed according to the classical probability distribution $p_{\mathrm{A}}(a)$. The Shannon

entropy is defined as

$$H(A) = -\sum_a p_{\mathrm{A}}(a)\log\left[p_{\mathrm{A}}(a)\right] \ , \tag{5.1}$$

where the base of the logarithm defines the entropy unit. The most common units are the *bit*, corresponding to base 2, and the *nat*, corresponding to base e. The Shannon entropy can be interpreted as the amount of information needed to predict that a measurement of the variable A on the system will yeld the result a. If we now consider a second system, described by a classical variable B with values $\{b\}$ distributed according to $p_{\mathrm{B}}(b)$, the bipartite system can be described by the joint probability distribution $p_{\mathrm{A,B}}(a,b)$ and its information content by the joint entropy $H(A,B) = -\sum_{a,b} p_{\mathrm{A,B}}(a,b)\log\left[p_{\mathrm{A,B}}(a,b)\right]$. As pictorially represented in Fig.5.1, the joint entropy is in general smaller than the sum of entropies of the two subsystems, being equal to the sum only when A and B are independent (*subadditivity* of the Shannon entropy). This prompts us to define the *mutual information* as the difference

$$I(A:B) = H(A) + H(B) - H(A,B) \ , \tag{5.2}$$

which expresses the total amount of correlations between A and B, *i.e.* their shared information. For a classical probability distribution the mutual information is equivalent to another expression, [93]:

$$I(A:B) = H(A) - H(A|B) \equiv H(B) - H(B|A) \ , \tag{5.3}$$

where the conditional entropy $H(A|B) = -\sum_{a,b} p_{\mathrm{A,B}}(a,b)\log\left[p_{\mathrm{A|B}}(a|b)\right]$ quantifies the amount of information B is missing in order to have complete knowledge of A. The following properties of the Shannon entropy are worth noting [23]:

$$\begin{aligned}
&H(A,B) = H(B,A) \text{ and } H(A:B) = H(B:A)\,,\\
&0 \leq H(A|B) \leq H(A)\,,\\
&0 \leq I(A:B) \leq H(A)\,,\\
&H(A,B) \leq H(A) + H(B)\,,\\
&H(A,B,C) + H(B) \leq H(A,B) + H(B,C)\,,
\end{aligned} \tag{5.4}$$

where the last property takes the name of *strong subadditivity*, which also implies the positivity of the mutual information.
The quantum analog of the Shannon entropy is the Von Neumann entropy, which quantifies the information content of a system A as

$$S(A) = -\mathrm{Tr}\left[\hat{\boldsymbol{\rho}}_{\mathrm{A}}\log\left[\hat{\boldsymbol{\rho}}_{\mathrm{A}}\right]\right] = -\sum_i \lambda_i \log\left[\lambda_i\right] \ , \tag{5.5}$$

where the λ_i are the eigenvalues of the density matrix obtained via its diagonalization $\hat{\boldsymbol{\rho}}_{\mathrm{A}} = \sum_i \lambda_i |i\rangle\langle i|$. From its definition is implied that the Von Neumann entropy is minimum for pure states, $S(|\psi_{\mathrm{A}}\rangle\langle\psi_{\mathrm{A}}|) = 0$, and is maximum for the maximally mixed state, $S(\mathbb{I}/d) = \log[d]$, with d being the dimension of the system's Hilbert state. Moreover, the Von Neumann entropy of a multipartite system might be lower than the sum of the entropies of each subsystem, as in the case of an entangled state which is pure when considered as a whole but each of its subsystems are mixed states if considered separately. For such a state therefore $S(A,B) = 0 < S(A) = S(B) > 0$.
Let's now consider two quantum systems A and B. We can establish the definition of mutual information in the quantum scenario for the composite system by simply replacing the Shannon entropy with the Von Neumann's, obtaining a measure that quantifies the total amount of correlations in the system:

$$\mathcal{I}(A:B) = S(A) + S(B) - S(A,B) \ , \tag{5.6}$$

where $S(A,B) = -\mathrm{Tr}\left[\hat{\boldsymbol{\rho}}_{AB} \log\left[\hat{\boldsymbol{\rho}}_{\mathrm{AB}}\right]\right]$ is the joint Von Neumann entropy of the system. However, if we apply the same approach to the mutual information of Eq.(5.3) we quickly realize that it leads to an ambiguous quantity, involving the conditional state of a subsystem after a measurement is performed on the other subsystem. As a consequence, the mutual information derived from Eq.(5.3) will be in general different from Eq.(5.6), and it will depend on which subsystem was measured, and on the measurement strategy. Without loss of generality we assume that a measurement described by the POVM $\hat{\Pi}_k$ is performed on subsystem B, leading to the observation of the outcome k. After such measurement the conditional state of subsystem A will be

$$\hat{\boldsymbol{\rho}}_{\mathrm{A}|k} = \frac{1}{p_{\mathrm{B}}(k)} \mathrm{Tr}_{\mathrm{B}} \left[\hat{\boldsymbol{\rho}}_{\mathrm{AB}}\, \mathbb{I} \otimes \hat{\Pi}_k\right] \ , \qquad p_{\mathrm{B}}(k) = \mathrm{Tr}\left[\hat{\boldsymbol{\rho}}_{\mathrm{AB}}\, \mathbb{I} \otimes \hat{\Pi}_k\right] \ . \tag{5.7}$$

Using this conditional density operator we can define the quantum analog of Eq.(5.3) as

$$\mathcal{J}_{\mathrm{A}}(A:B) = S(A) - \sum_k p_{\mathrm{B}}(k) S(A|k) \ , \tag{5.8}$$

where $S(A|k)$ is the conditional Von Neumann entropy associated to the state in Eq.(5.7). Eq.(5.8) can be interpreted as the information gain about subsystem A when the measurement $\hat{\Pi}_k$ is performed on subsystem B [94]. Maximization of this quantity over all possible measurements on B corresponds to finding the measurement that disturbs least the overall quantum state while at the same time providing the most information about A. The result of the maximization is the

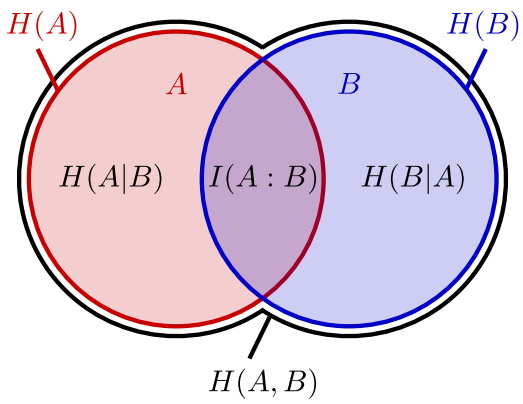

Figure 5.1: **Individual, joint and conditional Shannon entropies for the correlated subsystems A and B.** The total mutual information is shown as well.

upper bound

$$\mathcal{C}_{\mathrm{A}} = \sup_{\{\hat{\Pi}_k\}} \mathcal{J}_{\mathrm{A}}(A:B) = S(A) - \inf_{\{\hat{\Pi}_k\}} \sum_k p_{\mathrm{B}}(k) S(A|k) \ , \tag{5.9}$$

which is commonly interpreted as a measure of purely classical correlations in the system. Finally, the difference of the total correlations in Eq.(5.6) and the purely classical correlations of Eq.(5.9) gives the amount of purely quantum correlations in the system

$$\mathcal{D}_{\mathrm{A}}(\hat{\boldsymbol{\rho}}_{\mathrm{A,B}}) = \mathcal{I}(A:B) - \mathcal{C}_{\mathrm{A}} = S(B) - S(A,B) + \inf_{\{\hat{\Pi}_k\}} \sum_k p_{\mathrm{B}}(k) S(A|k) \ , \tag{5.10}$$

first introduced in [94] and in [95] with the name of *quantum A discord*. One could also derive the quantum B discord by considering a measurement on subsystem A, and in general this would produce a different result, $\mathcal{D}_{\mathrm{A}}(\hat{\boldsymbol{\rho}}_{\mathrm{ab}}) \neq \mathcal{D}_{\mathrm{B}}(\hat{\boldsymbol{\rho}}_{\mathrm{ab}})$. It is worth noting that the quantum discord is a non-negative quantity [96], as a result of the strong subadditivity of the Von Neumann entropy.
While explicit calculation of the quantum discord (QD) is feasible for specific families of discrete-variables quantum systems, like 2-qubits states [97], it is in general a challenging task due to the maximization in Eq.(5.9), especially for CV states [98, 99, 100]. Still, thanks to the power of the symplectic formalism introduced in Ch.2.2, the explicit derivation of the QD becomes simpler provided that we restrict the system to Gaussian states and operations [99, 100], as we will show in the next Section.

5.2 Gaussian quantum discord

In the following we restrict to two-mode Gaussian states and Gaussian operations, therefore full characterization of the system is provided by the covariance matrices of the states. In particular, the generic covariance matrix for a bipartite system of single mode Gaussian states $\hat{\boldsymbol{\rho}}_{\text{AB}}$ can be written as [101]

$$\hat{\boldsymbol{\sigma}}_{\text{AB}} = \begin{pmatrix} \boldsymbol{\alpha} & \boldsymbol{\gamma} \\ \boldsymbol{\gamma}^{\text{T}} & \boldsymbol{\beta} \end{pmatrix} , \tag{5.11}$$

where $\boldsymbol{\alpha}$ and $\boldsymbol{\beta}$ are the covariance matrices associated with the subsystems A and B, while $\boldsymbol{\gamma}$ contains the correlations between A and B. Let's now consider a generic local unitary transformation on the two modes associated with the symplectic operation $\hat{S}^{\Gamma}_{\text{A}} \oplus \hat{S}^{\Gamma}_{\text{B}}$: its action on the covariance matrix, given by Eq.(2.26), results in the following transformations on the submatrices:

$$\begin{aligned} \boldsymbol{\alpha} &\to \hat{S}^{\Gamma}_{\text{A}} \boldsymbol{\alpha} (\hat{S}^{\Gamma}_{\text{A}})^{\text{T}} \\ \boldsymbol{\beta} &\to \hat{S}^{\Gamma}_{\text{B}} \boldsymbol{\beta} (\hat{S}^{\Gamma}_{\text{B}})^{\text{T}} \\ \boldsymbol{\gamma} &\to \hat{S}^{\Gamma}_{\text{A}} \boldsymbol{\gamma} (\hat{S}^{\Gamma}_{\text{B}})^{\text{T}} \ . \end{aligned} \tag{5.12}$$

From these follows that the determinants of all three submatrices, $I_\alpha = \text{Det}\,[\alpha]$, $I_\beta = \text{Det}\,[\beta]$ and $I_\gamma = \text{Det}\,[\gamma]$, as well as the determinant of the covariance matrix itself $I_{\text{AB}} = \text{Det}\,[\hat{\boldsymbol{\sigma}}_{\text{AB}}]$, are local *symplectic invariants* with respect to the operation $\hat{S}^{\Gamma}_{\text{A}} \oplus \hat{S}^{\Gamma}_{\text{B}}$. We can always find $\hat{S}^{\Gamma}_{\text{A}}$ and $\hat{S}^{\Gamma}_{\text{B}}$ such that the submatrices of Eq.(5.11) be $\alpha = \text{Diag}\,[a, a]$, $\beta = \text{Diag}\,[b, b]$ and $\gamma = \text{Diag}\,[c, d]$. In turn, this allows us to express the symplectic invariants of the state in terms of the covariance matrix elements:

$$\begin{aligned} &I_\alpha = a^2 \ , \quad I_\beta = b^2 \ , \quad I_\gamma = cd \ , \\ &I_{\text{AB}} = (ab - c^2)(ab - d^2) \ . \end{aligned} \tag{5.13}$$

Interestingly, a condition [91] on the symplectic invariants for the physicality of $\hat{\boldsymbol{\rho}}_{\text{AB}}$ follows from Eq.(2.22) as

$$I_\alpha + I_\beta + 2I_\gamma \leq \frac{1}{2} + 2I_{\text{AB}} \ . \tag{5.14}$$

Another important consequence of the Williamson's theorem is that it is possible to express the eigenvalues of a generic covariance matrix, also known as the *symplectic eigenvalues*, in terms of the symplectic invariants as [102]

$$\nu_{\pm}^2 = \frac{\Delta \pm \sqrt{\Delta^2 - 4I_{\text{AB}}}}{2} \ , \tag{5.15}$$

where $\Delta = I_\alpha + I_\beta + 2I_\gamma$. As a final observation, as we pointed out in Sec.2.3, informationally relevant quantities such as the entropy and the entanglement of a system are invariant under local unitary transformations, therefore the quantum discord also shares this property, being defined through entropic quantities. We can express the Von Neumann entropy in terms of the symplectic eigenvalues as [102, 103]

$$S(\hat{\boldsymbol{\sigma}}) = f(\nu_+) + f(\nu_-) \ , \tag{5.16}$$

with $f(\nu) = (\frac{\nu+1}{2})\log\left[\frac{\nu+1}{2}\right] - (\frac{\nu-1}{2})\log\left[\frac{\nu-1}{2}\right]$, and it follows that we can derive a closed formula for the quantum discord of a generic two-mode Gaussian state from its standard form covariance matrix, which allows us to experimentally measure it through homodyning. From Eq.(5.19) we can see that the quantum A discord for a generic two-mode Gaussian state depends on the Von Neumann entropies of its measured subsystem B and of the whole system, and on the conditional entropy of subsystem A when B is measured. The Von Neumann entropy associated with subsystem B is easily found, as well as the Von Neumann entropy of the complete system, by applying Eq.(5.16) to $\boldsymbol{\beta}$ and $\hat{\boldsymbol{\sigma}}_{\rm AB}$ respectively. Calculation of the Von Neumann entropy for the conditional state of subsystem A of Eq.(5.7) can be obtained once we recall that we are considering only Gaussian states and Gaussian operations, thus the conditional entropy is restricted to generalized Gaussian POVMs on B. Any such measurement can be written as the POVM [104]

$$\hat{\Pi}_k = \frac{1}{\pi}\hat{D}(\alpha_k)\,\hat{\boldsymbol{\rho}}_0\,\hat{D}^\dagger(\alpha_k) \ , \tag{5.17}$$

where $\hat{D}(\alpha_k)$ is the displacement operator previously defined in Eq.(2.34) and $\hat{\boldsymbol{\rho}}_0$ is the density matrix of a generally mixed single-mode Gaussian state. Once the measurement on B is performed, the conditional state of subsystem A in Eq.(5.7) is associated with a covariance matrix given by the Shur complement [105]

$$\boldsymbol{\epsilon} = \boldsymbol{\alpha} - \boldsymbol{\gamma}(\boldsymbol{\beta} + \hat{\boldsymbol{\sigma}}_0)^{-1}\boldsymbol{\gamma}^\dagger \ , \tag{5.18}$$

where $\hat{\boldsymbol{\sigma}}_0$ is the covariance matrix associated to $\hat{\boldsymbol{\rho}}_0$, which does not depend on the measurement outcome k [106]. The general expression for the Gaussian quantum A discord therefore can be derived as

$$\mathcal{D}_{\rm A}(\hat{\boldsymbol{\rho}}_{\rm ab}) = f(\sqrt{I_\beta}) - f(\nu_-) - f(\nu_+) + \inf_{\hat{\boldsymbol{\sigma}}_0} f(\sqrt{\mathrm{Det}\,[\boldsymbol{\epsilon}]}) \ . \tag{5.19}$$

The minimization in the above expression is easily achieved as [100]

$$\mathrm{Det}\,[\boldsymbol{\epsilon}] = \begin{cases} \frac{2I_\gamma^2+(I_\beta-1)(I_{\rm AB}-I_\alpha)+2|I_\gamma|\sqrt{I_\gamma^2+(I_\beta-1)(I_{\rm AB}-I_\alpha)}}{(I_\beta-1)^2} & (a) \\ \frac{I_\alpha I_\beta - I_\gamma^3 + I_{\rm AB} - \sqrt{I_\gamma^4+(I_{\rm AB}-I_\alpha I_\beta)^2 - I - \gamma^2(I_{\rm AB}-I_\alpha I_\beta)}}{2I_\beta} & (b) \end{cases} \tag{5.20}$$

where (a) applies if $(I_{\text{AB}} - I_\alpha I_\beta)^2 \leq I_\gamma^2(I_\beta + 1)(I_{\text{AB}} + I_\alpha)$ and (b) applies otherwise.

5.3 Experiment

We may now introduce our experimental investigation of the evolution of quantum discord in an open system [107]. We start by giving some motivations for such study, followed by the description of the experimental setup. We finally present the results obtained in the cases of two-mode squeezed states and of mixtures of coherent states.

5.3.1 Motivation

Quantum correlations play a key role as the fundamental resource required for overcoming the classical limits on the performances of many information tasks, as in the case of quantum metrology [2]. In some cases quantum correlations even provide the means of performing tasks which have no classical counterpart at all, as for teleportation [6] and quantum cryptography [5]. Traditionally entanglement has been regarded as the only form of quantum correlations, yet it has been shown that some quantum information tasks which require quantum correlations can in fact be carried out using separable states, which do not contain any entanglement. Examples range from single-qubit quantum computation [108, 109] to quantum key distribution [110]. This raises the question whether quantum correlations in mixed states are to be considered as the fundamental resource for quantum information processing, and which kind of tasks require what type of quantum correlations. As shown in the previous sections, a measure of non-classical correlations that goes beyond entanglement in the class of separable states is the quantum discord. Since its introduction in 2001 [94, 95], the quantum discord has been extensively studied in order to verify whether it might be the actual source of the quantum enhancement in mixed-state quantum information [111, 112, 113], and it has been shown that almost all quantum states carry some discord-type correlations [114]. While entanglement is a very fragile resource, it has been shown, both in discrete [115, 116, 117] and in continuous variable settings [118], that the quantum discord of some states is instead robust against Markovian decoherence and in fact it can even increase under dissipation. Along these lines, we experimentally characterize the Gaussian discord of two-mode squeezed states and separable two-mode mix-

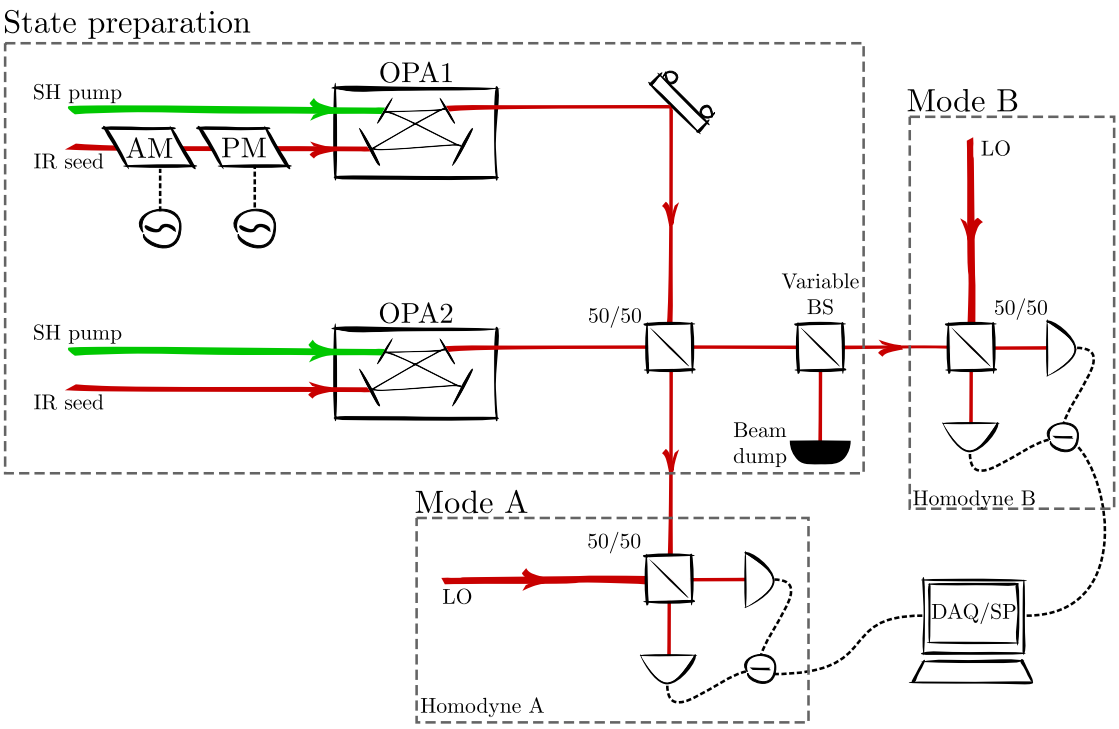

Figure 5.2: **Experimental setup.** IR: infrared (1064 nm); SH: second harmonic (532 nm); PM/AM: phase/amplitude electro-optical modulator; OPA: optical parametric amplifier; BS: beam splitter; LO: local oscillator; DAQ/SP: data acquisition/signal processing.

tures of coherent states. We analyze the evolution of the Gaussian discord in an open quantum system described by local Markovian decoherence in the form of Gaussian noise addition corresponding to a classical noise channel and pure attenuation, showing that while the discord of the two-mode squeezed states is degraded by dissipative dynamics, in the separable state scenario the opposite behaviour is observed.

5.3.2 Experimental setup

A schematic diagram of the experimental setup is shown in Fig.5.2. A pair of optical parametric amplifers (OPAs) based on type I quasi-phase-matched PPKTP (periodically poled potassium titanyl phosphate) cystals placed inside bow-tie cavities were used to generate two independent amplitude-squeezed beams at 1064 nm. The OPAs were weakly seeded at 1064 nm to lock the cavities and provide a reference phase for the experiment. Both OPA outputs had 3.2 ± 0.2 dB of squeezing and 6.7 ± 0.2 dB of anti-squeezing, which was measured using a homodyne detector

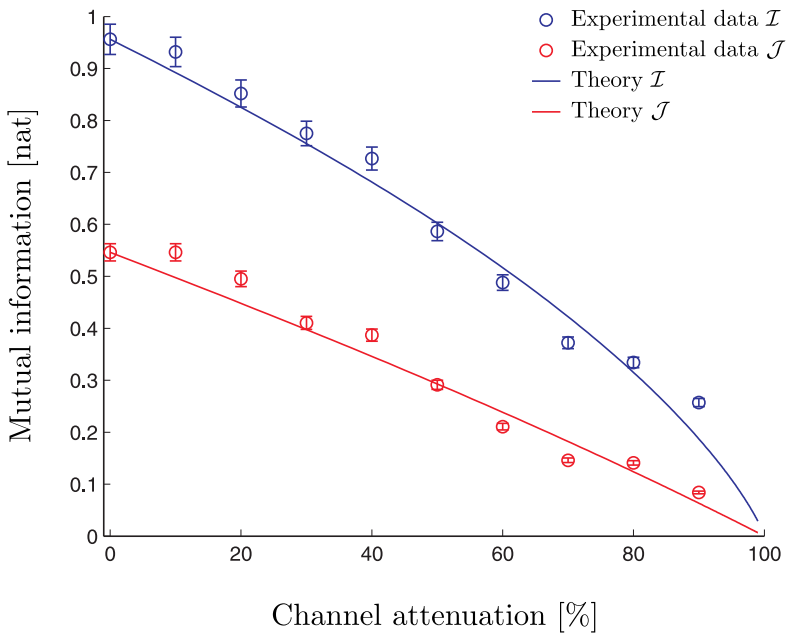

Figure 5.3: **Mutual information for the two-mode squeezed state.** The circles represent the total correlations $\mathcal{I}$ (blue) and the purely classical correlations $\mathcal{J}$. The solid lines are theoretical curves fitted to the first data point.

with a total efficiency of $85 \pm 5\%$ and electronic noise contribution of -20 dB relative to shot noise. The measurements were performed at the sideband frequency of 4.9 MHz with a bandwidth of 90 kHz. To generate correlations in addition to those produced in the OPAs, one of the seed beams was symmetrically modulated with two electro-optic modulators (EOM), specifically an amplitude and a phase modulator, that were driven by independent electronic noise generators. The two OPA output beams were interfered on a balanced beam splitter and locked to a $\pi/2$ relative squeezing phase between each other to produce a pair of quadrature entangled beams at the beam splitter outputs. While one of the beam splitter's output modes (mode A) was sent directly to the homodyning stage A, the other (mode B) propagated through a dissipative channel implemented with a variable transmissivity beam splitter (*i.e.* a polarizing beam splitter preceded by a half wave plate), before entering the homodyning stage B. With such setup we could therefore generate and investigate a variety of two-mode Gaussian states.

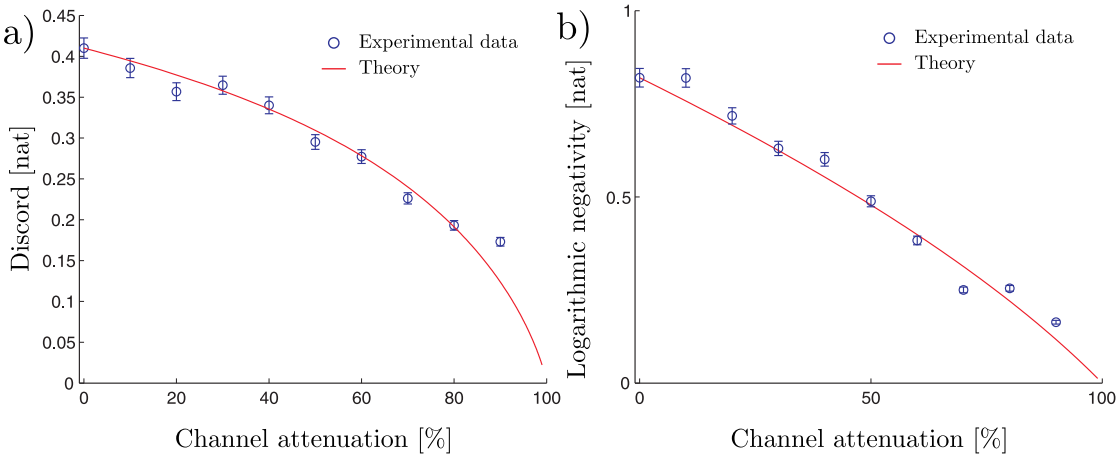

Figure 5.4: **Discord and entanglement for the two-mode squeezed state. a)** Here is shown the Gaussian discord versus the B mode's attenuation. **b)** Logarithmic negativity versus the B mode's attenuation. The circles represent experimental data, while the solid lines are theoretical curves obtained from the first data point. The error bars indicate the statistical error.

5.3.3 Discord of two-mode squeezed states

As pointed out in section 5.2, when a bipartite Gaussian state is subject to Gaussian operations and Gaussian measurements, its discord is easily obtainable through the elements of its covariance matrix as in Eq.(5.19) and Eq.(5.20). By homodyning on modes A and B we could directly measure the state's covariance matrix elements, and use them to compute the Gaussian discord of the two-mode squeezed state. We obtained the values for the Gaussian discord for different attenuations of mode B, by increasing the reflectivity of the variable beam splitter in its path. The results are shown in Fig.5.3, where we plot the total correlations $\mathcal{I}$ and purely classical correlations $\mathcal{J}$ versus the attenuation of mode B, and in Fig.5.4, where we plot the Gaussian discord and logarithmic negativity versus the attenuation of mode B. As expected, we observe a monotonic decrease of all quantities [119]: As the dissipation of mode B increases, the bipartite state loses both purely classical correlations and purely quantum correlations, resulting in the monotonic decrease of the total correlations $\mathcal{I}$. Since two-mode squeezed states are pure, they contain entanglement-type quantum correlations, which we can quantify using the logarithmic negativity [120]. As shown in Fig.(5.4) (**b**), attenuation of one of the modes is detrimental to the entanglement content of the state. We can conclude that dissipation affects negatively both the entanglement and the Gaussian discord of two-mode squeezed states.

5.3.4 Discord of mixtures of coherent states

As previously pointed out, the quantum discord is a measure of quantum correlations that goes beyond entanglement, deep into the class of separable states. We tested what the effect of dissipation is on separable mixed states, which indeed contain a certain degree of purely quantum correlations, as we will promptly show. In order to generate mixtures of coherent states we set both OPAs offline by turning off the pumps, generating therefore vacuum states as their output. We applied white noise amplitude and phase modulations on the seed beam of OPA1 to generate a thermal state, while we kept a vacuum as the output of OPA2. The output modes of the OPAs were then mixed on a balanced beam splitter, whose output was therefore a bipartite mixture of coherent states with correlations between the amplitude and the phase quadratures. Before testing the attenuating channel on mode B, we computed the total correlations, purely classical correlations and the discord for increasing modulation depth (average number of thermal photons). As shown in Fig.5.5, the discord of our mixed states was expected to increase monotonically with the modulation depth, eventually reaching saturation for large modulations. Instead, the experimental results followed the theoretical expectation for small modulation depths, reaching a maximum and then decreasing, thus deviating from the predicted behavior. Such discrepancy was due to the finite common mode rejection ratio (CMR) between the detectors, which we measured being 27 dB. Finite CMR results in the measurement of uncorrelated events which simulate a classically noisy channel, where the noise intensity scales with the modulation depth. To simulate the effect of such classical noise channel on the discord of our coherent mixtures, we measured the total correlations $\mathcal{I}$ and purely classical correlations $\mathcal{J}$ for a reduced CMR of 15 dB. We observed (Fig.5.6) the transition from a quantum regime with non-zero discord to a classical regime with near zero discord characterized by having a high energy but finite signal to noise ratio in the correlations.

To study the effect of dissipation on the coherent state mixtures we used the same method as in the two-mode squeezing scenario, setting the variable beam splitter to different transmissivities to simulate various dissipation levels. We performed such measurement for different fixed increasing modulation depths, corresponding to increasing classical noise addition. From the results, shown in Fig.5.7 and Fig.5.8, we observe a decrease of the overall discord content as a function of

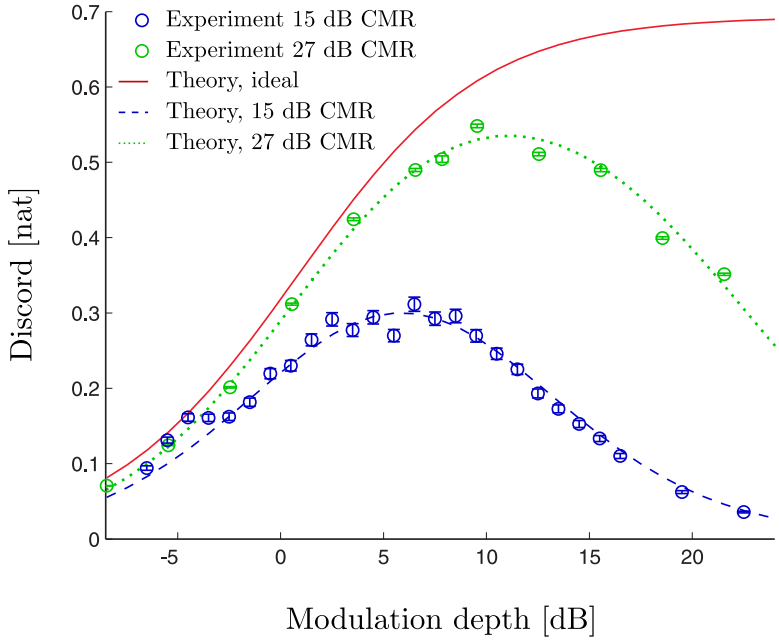

Figure 5.5: **Quantum discord of a mixture of coherent states as a function of the modulation depth.** Experimental data (circles) are shown for 27 dB (green) and 15 dB (blue) of common mode rejection ratio (CMR) between homodyne detectors A and B. The solid line is the ideal curve for infinite CMR, while the dotted and dashed lines are theoretical curves for 27 and 15 dB CMR, respectively. The error bars indicate the statistical error.

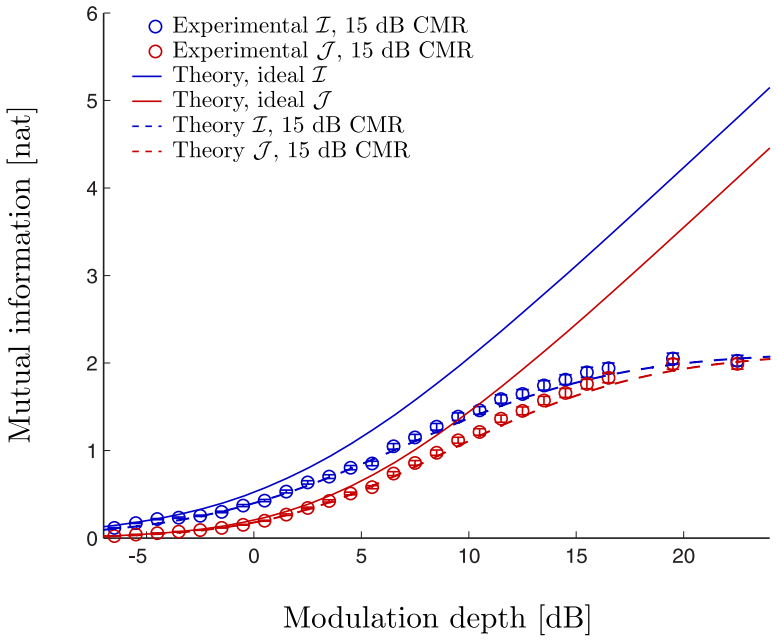

Figure 5.6: **Total correlations $\mathcal{I}$ and purely classical correlations $\mathcal{J}$ versus the modulation depth.** Solid lines represent the theoretical curves for infinite CMR, while the circles indicate experimental data for $\mathcal{I}$ (blue) and $\mathcal{J}$ (red), with 15 dB CMR. The dashed lines are theoretical curves for the experimental CMR of 15 dB. The error bars indicate the statistical error.

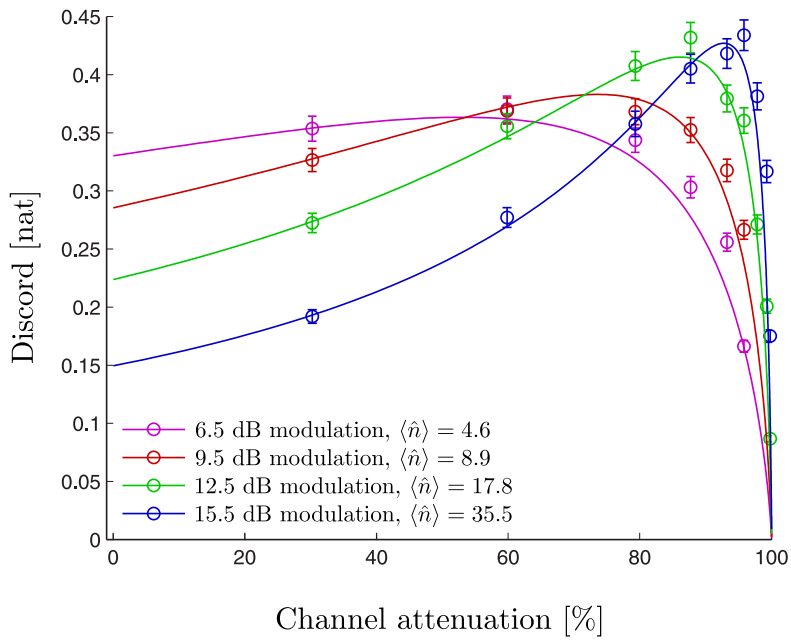

Figure 5.7: **Discord for different modulation depths of the coherent mixture, and for increasing attenuation of mode B.** The experimental data are represented by circles, while the solid lines represent the theoretical predictions obtained by fitting the first data point (zero attenuation). Error bars indicate the statistical uncertainty. **b)** Mutual information $\mathcal{I}$ (blue) and one-way classical information $\mathcal{J}$ (red) corresponding to the different modulation depths. The circles represent experimental data, while solid curves are theoretical fits to the first data point (no attenuation). Error bars indicate the statistical error.

the uncorrelated classical noise addition. yet, increasing attenuation corresponds to an increase of the discord content which gets steeper as the modulation depth increases. This suggests a high robustness of the discord of separable mixed states under dissipative dynamics, in contrast with entanglement, which cannot increase under any local transformation, let it be unitary or not [121]. The revival of the discord under dissipative dynamics is due to two separate effects. For starters, attenuation results in the attenuation of uncorrelated classical noise in mode B, which is responsible for the near death of discord, as shown in Fig.5.5. A second factor contributing to the discord revival is the relatively higher amplitude of mode A, which makes the noise contribution of a measurement on mode B more significant, thus increasing the difference between the information that can be obtained through classical and quantum means.

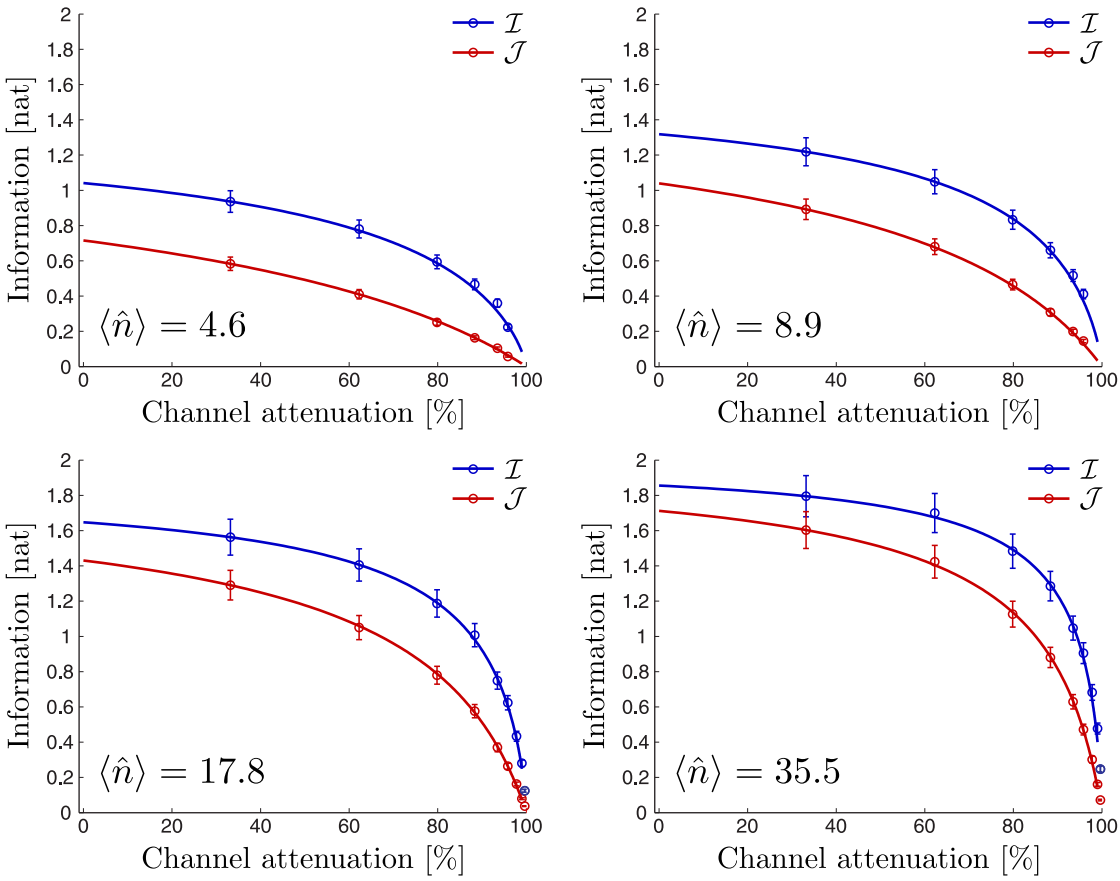

Figure 5.8: **Mutual and one way information for coherent states mixtures.** Mutual information $\mathcal{I}$ (blue) and one-way classical information $\mathcal{J}$ (red) corresponding to the different modulation depths. The circles represent experimental data, while solid curves are theoretical fits to the first data point (no attenuation). Error bars indicate the statistical error.

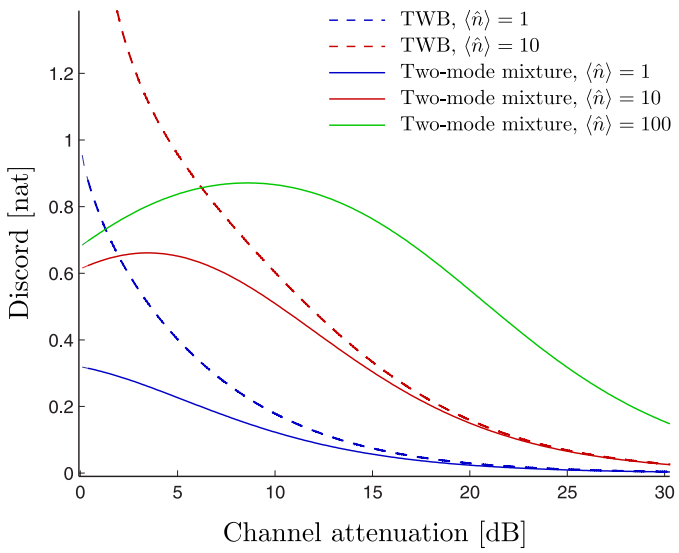

Figure 5.9: **Theoretical prediction for the evolution of the Gaussian discord.** Here are shown theoretical prediction for the evolution of the Gaussian discord in the two-mode squeezed (TWB) and the coherent mixture scenarios in an attenuating channel.

5.3.5 Conclusions

From the results of the previous section is apparent that the discord of separable mixtures of coherent states is more robust than the one of two-mode squeezed states when undergoing losses. It is worth noting though that the latter will exhibit the highest amount of discord for any amount of Markovian loss if we consider same probe energy scenarios, as shown in the simulations in Fig.5.9. Of course, as the number of photons in the bipartite state increase, the pure entangled states become more and more difficult to produce, while the separable states only require a higher modulation depth, which is easy to accomplish with electro-optical modulators.

In conclusion, we experimentally generated two sets of bipartite states containing quantum correlations: a two-mode squeezed state containing entanglement and quantum discord, and a separable mixture of coherent states containing quantum discord but not entanglement. We showed that the discord contained in the entangled state had no robustness at all when one of the modes was subject to dissipative dynamics, while the opposite was true for the discord of the separable state, which instead increased with the attenuation reaching a maximum after which it rapidly vanished. We also showed that the discord of the separable states was reduced as a consequence of uncorrelated noise addition, and that the overall content of discord-type correlations was higher in the entangled state.

Appendix A

Calculation of the Quantum Fisher information

Here we derive an expression for the quantum Fisher information of a pure, phase-shifted squeezed vacuum state (Eq.3.15). Afterwards, we extend the result to the thermal scenario (Eq.3.31).
Let us consider a general state $\hat{\boldsymbol{\rho}}$ undergoing a unitary phase transformation as defined in Eq.2.41

$$\hat{\boldsymbol{\rho}}_\phi = \hat{U}(\phi)\,\hat{\boldsymbol{\rho}}\,\hat{U}^\dagger(\phi)\,, \quad \hat{U}(\phi) = \mathrm{Exp}\left[-\imath\phi\hat{n}\right]\,.$$

In the following we will indicate the transformation simply as $\hat{U}$. In the pure state scenario we have $\hat{\boldsymbol{\rho}}_\phi = \hat{\boldsymbol{\rho}}_\phi^2$ because the phase transformation is unitary. As a consequence,

$$\partial_\phi\left(\hat{\boldsymbol{\rho}}_\phi^2\right) = \left(\partial_\phi\,\hat{\boldsymbol{\rho}}_\phi\right)\hat{\boldsymbol{\rho}}_\phi + \hat{\boldsymbol{\rho}}_\phi\left(\partial_\phi\,\hat{\boldsymbol{\rho}}_\phi\right) = \partial_\phi\,\hat{\boldsymbol{\rho}}_\phi\,.$$

Comparing this expression with the definition of the symmetric logarithmic derivative (Eq.3.6) allows us to retrieve an explicit form for the SLD

$$\begin{cases} \partial_\phi\,\hat{\boldsymbol{\rho}}_\phi = \left(\partial_\phi\,\hat{\boldsymbol{\rho}}_\phi\right)\hat{\boldsymbol{\rho}}_\phi + \hat{\boldsymbol{\rho}}_\phi\left(\partial_\phi\,\hat{\boldsymbol{\rho}}_\phi\right) \\ \partial_\phi\,\hat{\boldsymbol{\rho}}_\phi = \frac{1}{2}\hat{\Lambda}_\phi\,\hat{\boldsymbol{\rho}}_\phi + \frac{1}{2}\,\hat{\boldsymbol{\rho}}_\phi\,\hat{\Lambda}_\phi \end{cases} \Rightarrow \hat{\Lambda}_\phi = 2\partial_\phi\,\hat{\boldsymbol{\rho}}_\phi\,.$$

We may now observe that

$$\begin{aligned} 2\partial_\phi\,\hat{\boldsymbol{\rho}}_\phi &= 2\partial_\phi\left(\hat{U}\,\hat{\boldsymbol{\rho}}\,\hat{U}^\dagger\right) = 2\left((\partial_\phi\hat{U})\,\hat{\boldsymbol{\rho}}\,\hat{U}^\dagger + \hat{U}(\partial_\phi\,\hat{\boldsymbol{\rho}})\hat{U}^\dagger + \hat{U}\,\hat{\boldsymbol{\rho}}(\partial_\phi\hat{U}^\dagger)\right) = \\ &= 2\left(-\imath\hat{n}\hat{U}\,\hat{\boldsymbol{\rho}}\,\hat{U}^\dagger + \imath\hat{U}\,\hat{\boldsymbol{\rho}}\,\hat{n}\hat{U}^\dagger\right) = 2\imath\left(\hat{\boldsymbol{\rho}}_\phi\,\hat{n} - \hat{n}\,\hat{\boldsymbol{\rho}}_\phi\right)\,. \end{aligned}$$

Simple substitution in the definition of the quantum Fisher information, Eq.3.10, leads to

$$\begin{aligned} H &= \mathrm{Tr}\left[\hat{\boldsymbol{\rho}}_\phi \Lambda_\phi^2\right] = \mathrm{Tr}\left[\hat{U}\,\hat{\boldsymbol{\rho}}\,\hat{U}^\dagger\hat{U}\hat{\Lambda}_\phi\hat{U}^\dagger\hat{U}\hat{\Lambda}_\phi\hat{U}^\dagger\right] = \\ &= \mathrm{Tr}\left[\hat{\boldsymbol{\rho}}\,\hat{\Lambda}^2\right] = \mathrm{Tr}\left[\hat{\boldsymbol{\rho}}\,(2\imath\,(\hat{\boldsymbol{\rho}}\,\hat{n} - \hat{n}\,\hat{\boldsymbol{\rho}}))^2\right] = \\ &= 4\left(\langle\hat{n}^2\rangle_{\hat{\boldsymbol{\rho}}} - \langle\hat{n}\rangle_{\hat{\boldsymbol{\rho}}}^2\right) = 4(\Delta\hat{n}^2)_{\hat{\boldsymbol{\rho}}}\,. \end{aligned}$$

where we used $\hat{\Lambda}_\phi = \hat{U}\hat{\Lambda}\hat{U}^\dagger$, the purity of the state $\hat{\boldsymbol{\rho}}_\phi = \hat{\boldsymbol{\rho}}_\phi^2$ and the cyclic property of the trace. Now we can simply substitute the energy fluctuations $(\Delta\hat{n}^2)_{\hat{\boldsymbol{\rho}}}$ for the case of interest, *i.e.* a squeezed vacuum state, from Eq.2.46

$$H_{0,\mathrm{z}} = 8\cosh^2(r)\sinh^2(r) = 2\sinh^2(2r)\,.$$

In the general mixed scenario we start by expanding the state on an eigenvector basis $\{|\psi_i\rangle\}$ as

$$\hat{\boldsymbol{\rho}}_\phi = \sum_i p_i\hat{U}(\phi)|\psi_i\rangle\langle\psi_i|\hat{U}^\dagger(\phi) = \sum_i p_i|\tilde{\psi}_i\rangle\langle\tilde{\psi}_i|\,,$$

where we defined the transformed basis $|\tilde{\psi}_i\rangle := \hat{U}(\phi)|\psi_i\rangle$. Now we consider the definition of the symmetric logarithmic derivative in Eq.3.6

$$\partial_\phi\,\hat{\boldsymbol{\rho}}_\phi = \frac{1}{2}(\hat{\Lambda}_\phi\,\hat{\boldsymbol{\rho}}_\phi + \hat{\boldsymbol{\rho}}_\phi\,\hat{\Lambda}_\phi)\,.$$

Replacing the expansion of $\hat{\boldsymbol{\rho}}_\phi$ in the left and right side of the above expression we obtain respectively

$$\begin{aligned} \partial_\phi\,\hat{\boldsymbol{\rho}}_\phi &= \partial_\phi\left(\sum_i p_i\hat{U}(\phi)|\psi_i\rangle\langle\psi_i|\hat{U}^\dagger(\phi)\right) = \\ &= \imath\sum_{i,j}\langle\psi_i|\hat{n}|\psi_j\rangle(p_i - p_j)|\tilde{\psi}_i\rangle\langle\tilde{\psi}_j|\,, \\ \frac{1}{2}(\hat{\Lambda}_\phi\,\hat{\boldsymbol{\rho}}_\phi + \hat{\boldsymbol{\rho}}_\phi\,\hat{\Lambda}_\phi) &= \frac{1}{2}\sum_i p_i\left(\hat{\Lambda}_\phi|\tilde{\psi}_i\rangle\langle\tilde{\psi}_i| + |\tilde{\psi}_i\rangle\langle\tilde{\psi}_i|\hat{\Lambda}_\phi\right)\,. \end{aligned}$$

The matrix elements in the transformed basis of the SLD definition therefore read

$$\begin{aligned} \langle\tilde{\psi}_h|\partial_\phi\,\hat{\boldsymbol{\rho}}_\phi\,|\tilde{\psi}_k\rangle &= \tfrac{1}{2}\langle\tilde{\psi}_h|(\hat{\Lambda}_\phi\,\hat{\boldsymbol{\rho}}_\phi + \hat{\boldsymbol{\rho}}_\phi\,\hat{\Lambda}_\phi)|\tilde{\psi}_k\rangle\,, \\ \imath\textstyle\sum_{i,j} n_{ij}(p_i - p_j)\langle\tilde{\psi}_h|\tilde{\psi}_i\rangle\langle\tilde{\psi}_j|\tilde{\psi}_k\rangle &= \tfrac{1}{2}\textstyle\sum_i p_i\left(\langle\tilde{\psi}_h|\hat{\Lambda}_\phi|\tilde{\psi}_i\rangle\langle\tilde{\psi}_i|\tilde{\psi}_k\rangle + \langle\tilde{\psi}_h|\tilde{\psi}_i\rangle\langle\tilde{\psi}_i|\hat{\Lambda}_\phi|\tilde{\psi}_k\rangle\right)\,, \end{aligned}$$

where we defined $n_{ij} := \langle\psi_i|\hat{n}|\psi_j\rangle$. We can now perform the sums in the above expression, taking advantage of the Kronecker deltas

$$\imath n_{hk}(p_h - p_k) = \frac{1}{2}\langle\tilde{\psi}_h|\hat{\Lambda}_\phi|\tilde{\psi}_k\rangle(p_h + p_k)\,.$$

Since $\hat{\Lambda}_\phi = \hat{U}(\phi)\hat{\Lambda}\hat{U}^\dagger(\phi)$, the above result yields

$$\langle\tilde{\psi}_h|\hat{\Lambda}_\phi|\tilde{\psi}_k\rangle = \langle\psi_h|\hat{\Lambda}|\psi_k\rangle = 2\imath n_{hk}\frac{p_h - p_k}{p_h + p_k}\,.$$

At this point we can explicitly calculate the quantum Fisher information as defined in Eq.3.10

$$\begin{aligned}
H(\phi) &= \mathrm{Tr}\left[\hat{\boldsymbol{\rho}}_\phi\,\hat{\Lambda}_\phi^2\right] = \mathrm{Tr}\left[\hat{\boldsymbol{\rho}}\,\hat{\Lambda}^2\right] = \\
&= \sum_{i,j}\langle\psi_i|p_j|\psi_j\rangle\langle\psi_j|\hat{\Lambda}^2|\psi_i\rangle = \sum_{i,j,k} p_j\delta_{ij}\langle\psi_j|\hat{\Lambda}|\psi_k\rangle\langle\psi_k|\hat{\Lambda}|\psi_i\rangle = \\
&= \sum_{i,j,k} p_j\delta_{ij}(2\imath)^2 n_{jk}\frac{p_j - p_k}{p_j + p_k}n_{ki}\frac{p_k - p_i}{p_k + p_i} = 4\sum_{i,k} p_i|n_{ik}|^2\left(\frac{p_i - p_k}{p_i + p_k}\right)^2\,,
\end{aligned}$$

where we used $n_{ij} = n^*_{j,i}$.
In our specific case we deal with a squeezed thermal state, therefore we have

$$p_i = \nu_i = \frac{\mathrm{n_{th}}^i}{(\mathrm{n_{th}}+1)^{i+1}}\,, \qquad n_{ik} = \langle i|\hat{S}\hat{n}\hat{S}^\dagger|k\rangle\,,$$

where we expanded the initial state in the Fock basis. We have

$$H = 4\sum_{i,k}\nu_i\left(\frac{\nu_i - \nu_k}{\nu_i + \nu_k}\right)^2\left|\langle i|\hat{S}\hat{n}\hat{S}^\dagger|k\rangle\right|^2\,.$$

Since $\hat{S}$ is unitary, we can insert $\hat{S}^\dagger\hat{S} = \mathbb{I}$ between the creation and the annihilation operators in $\hat{n}$, so that we can take advantage of the relations in Eq.2.45 with $\mu := \cosh(r)$ and $\nu := \mathrm{e}^{\imath\psi}\sinh(r)$

$$\begin{aligned}
H &= 4\sum_{i,k}\nu_i\left(\frac{\nu_i - \nu_k}{\nu_i + \nu_k}\right)^2\left|\langle i|\hat{S}\hat{a}^\dagger\hat{S}^\dagger\hat{S}\hat{a}\hat{S}^\dagger|k\rangle\right|^2 = \\
&= 4\sum_{i,k}\nu_i\left(\frac{\nu_i - \nu_k}{\nu_i + \nu_k}\right)^2\left|\langle i|(\mu\hat{a}^\dagger + \nu^*\hat{a})(\mu\hat{a} + \nu\hat{a}^\dagger)|k\rangle\right|^2 = \\
&= 4\sum_{i,k}\nu_i\left(\frac{\nu_i - \nu_k}{\nu_i + \nu_k}\right)^2\Big[\left(\mu^2 k + |\nu|^2(k+1)\right)^2\delta_{i,k} + \\
&\qquad + k(k-1)\mu^2|\nu|^2\delta_{i,k-2} + \\
&\qquad + (k+1)(k+2)\mu^2|\nu|^2\delta_{i,k+2}\Big]\,,
\end{aligned}$$

Now, thanks to the thermal factor, the terms with $\delta_{i,k}$ vanish, and we are left with

$$
\begin{aligned}
H &= 4\mu^2|\nu|^2 \sum_k \nu_k \left(\frac{\nu_{k-2}-\nu_k}{\nu_{k-2}+\nu_k}\right)^2 k(k-1) + \\
&+ 4\mu^2|\nu|^2 \sum_k \nu_k \left(\frac{\nu_{k+2}-\nu_k}{\nu_{k+2}+\nu_k}\right)^2 (k+1)(k+2) = \\
&= \frac{8(\mathrm{n_{th}}+1)^3(2\,\mathrm{n_{th}}+1)\mu^2|\nu|^2}{\mathrm{n_{th}}(2\,\mathrm{n_{th}}^2+2\,\mathrm{n_{th}}+1)} - \frac{8\,\mathrm{n_{th}}^2(2\,\mathrm{n_{th}}+1)\mu^2|\nu|^2}{2\,\mathrm{n_{th}}^2+2\,\mathrm{n_{th}}+1}\,.
\end{aligned}
$$

We may now replace μ and ν to obtain the final expression

$$
H = 2\sinh^2(2r)\frac{(2\,\mathrm{n_{th}}+1)^2}{2\,\mathrm{n_{th}}^2+2\,\mathrm{n_{th}}+1}
$$

Appendix B

Calculation of the Fisher information

Here we calculate the classical Fisher information for homodyne detection of a pure, squeezed vacuum state (Eq.3.19). Afterwards, we extend the result to the thermal scenario (Eq.3.32).
We start with the definition of the Fisher information (Eq.3.5) applied to the case of a unitary phase transformation

$$F(\phi) = \int_{\mathbb{R}} \mathrm{d}x P(x|\phi) \left[\partial_\phi \log \left[P(x|\phi)\right]\right]^2$$

where $P(x|\phi)$ is the homodyne probability distribution for the x quadrature.
In the pure state scenario the $P(x|\phi)$ is given by Eq.3.18. By replacing it in the above expression we find

$$\begin{aligned}
F(\phi) &= \int_{\mathbb{R}} \frac{\mathrm{Exp}\left[-\frac{x^2}{2\sigma_{0,\mathrm{z}}}\right]}{\sqrt{2\pi\sigma_{0,\mathrm{z}}}} \left(\partial_\phi \log \left[\frac{\mathrm{Exp}\left[-\frac{x^2}{2\sigma_{0,\mathrm{z}}}\right]}{\sqrt{2\pi\sigma_{0,\mathrm{z}}}}\right]\right)^2 \mathrm{d}x = \\
&= \int_{\mathbb{R}} \frac{\mathrm{Exp}\left[-\frac{x^2}{2\sigma_{0,\mathrm{z}}}\right]}{\sqrt{2\pi\sigma_{0,\mathrm{z}}}} \left(\partial_\phi \left(-\frac{1}{2}\log\left[2\pi\sigma_{0,\mathrm{z}}\right] - \frac{x^2}{2\sigma_{0,\mathrm{z}}}\right)\right)^2 \mathrm{d}x = \\
&= \int_{\mathbb{R}} \frac{\mathrm{Exp}\left[-\frac{x^2}{2\sigma_{0,\mathrm{z}}}\right]}{\sqrt{2\pi\sigma_{0,\mathrm{z}}}} \left(-\frac{x^2}{2}\partial_\phi \frac{1}{\sigma_{0,\mathrm{z}}} - \frac{1}{2}\partial_\phi \log\left[\sigma_{0,\mathrm{z}}\right]\right)^2 \mathrm{d}x\,.
\end{aligned}$$

The two derivatives are easyly calculated

$$\partial_\phi \frac{1}{\sigma_{0,\mathrm{z}}} = -\frac{2\sinh(2r)\sin(2\phi)}{(\sigma_{0,\mathrm{z}})^2}\,,$$
$$\partial_\phi \log\left[\sigma_{0,\mathrm{z}}\right] = \frac{2\sinh(2r)\sin(2\phi)}{\sigma_{0,\mathrm{z}}}\,,$$

therefore we have

$$\begin{aligned}
F(\phi) &= \frac{1}{\sqrt{2\pi\sigma_{0,\mathrm{z}}}}\int_{\mathbb{R}} \mathrm{Exp}\left[-\frac{x^2}{2\sigma_{0,\mathrm{z}}}\right]\frac{\sinh^2(2r)\sin^2(2\phi)}{(\sigma_{0,\mathrm{z}})^2}\left(\frac{x^2}{\sigma_{0,\mathrm{z}}}-1\right)^2 \mathrm{d}x = \\
&= \frac{\sinh^2(2r)\sin^2(2\phi)}{(\sigma_{0,\mathrm{z}})^2\sqrt{2\pi\sigma_{0,\mathrm{z}}}}\int_{\mathbb{R}} \mathrm{Exp}\left[-\frac{x^2}{2\sigma_{0,\mathrm{z}}}\right]\left(\frac{x^4}{(\sigma_{0,\mathrm{z}})^2}-\frac{2x^2}{\sigma_{0,\mathrm{z}}}+1\right)^2 \mathrm{d}x = \\
&= \frac{\sinh^2(2r)\sin^2(2\phi)}{\sqrt{2\pi}(\sigma_{0,\mathrm{z}})^{5/2}}\left(\frac{1}{(\sigma_{0,\mathrm{z}})^2}\int_{\mathbb{R}} x^4 \mathrm{e}^{-\frac{x^2}{2\sigma_{0,\mathrm{z}}}}\mathrm{d}x - \frac{2}{\sigma_{0,\mathrm{z}}}\int_{\mathbb{R}} x^2 \mathrm{e}^{-\frac{x^2}{2\sigma_{0,\mathrm{z}}}}\mathrm{d}x + \int_{\mathbb{R}} \mathrm{e}^{-\frac{x^2}{2\sigma_{0,\mathrm{z}}}}\mathrm{d}x\right)\,.
\end{aligned}$$

Calculation of the three Gaussian integrals leads to

$$\int_{\mathbb{R}} x^4 e^{-\frac{x^2}{2\sigma_{0,\mathrm{z}}}}\mathrm{d}x = 3\sqrt{2\pi}(\sigma_{0,\mathrm{z}})^{\frac{5}{2}}\,,$$
$$\int_{\mathbb{R}} x^2 e^{-\frac{x^2}{2\sigma_{0,\mathrm{z}}}}\mathrm{d}x = \sqrt{2\pi}(\sigma_{0,\mathrm{z}})^{\frac{3}{2}}\,,$$
$$\int_{\mathbb{R}} e^{-\frac{x^2}{2\sigma_{0,\mathrm{z}}}}\mathrm{d}x = \sqrt{2\pi\sigma_{0,\mathrm{z}}}\,,$$

therefore the final expression for the Fisher information of homodyne detection on a phase shifted amplitude-squeezed vacuum state reads

$$F(\phi) = \frac{\sinh^2(2r)\sin^2(2\phi)}{(\sigma_{0,\mathrm{z}})^{5/2}}\left(3\sqrt{\sigma_{0,\mathrm{z}}} - 2\sqrt{\sigma_{0,\mathrm{z}}} + \sqrt{\sigma_{0,\mathrm{z}}}\right) = \frac{2\sinh^2(2r)\sin^2(2\phi)}{(\sigma_{0,\mathrm{z}})2}\,.$$

In the thermal scenario the covariance matrix of the phase shifted squeezed thermal state in Eq.3.30 has the same form as in the pure case, rescaled by the thermal factor $(2\,\mathrm{n_{th}}+1)$. In this case the homodyne probability distribution for the x quadrature reads

$$P(x|\phi) = \frac{1}{\sqrt{2\pi\sigma_{\mathrm{th,z}}}}\mathrm{Exp}\left[-\frac{x^2}{2\sigma_{\mathrm{th,z}}}\right]\,,$$

where $\sigma_{\mathrm{th,z}} = (2\,\mathrm{n_{th}}+1)\sigma_{0,\mathrm{z}}$. By simply applying the variable change

$$u = \frac{x}{\sqrt{2\,\mathrm{n_{th}}+1}} \longrightarrow \mathrm{d}u = \frac{1}{\sqrt{2\,\mathrm{n_{th}}+1}}\mathrm{d}x$$

the problem is reduced to the calculation of

$$F(\phi) = \int_{\mathbb{R}} \frac{\mathrm{Exp}\left[-\frac{u^2}{2\sigma_{0,\mathrm{z}}}\right]}{\sqrt{2\pi\sigma_{0,\mathrm{z}}}} \left(\partial_\phi \log\left[\frac{\mathrm{Exp}\left[-\frac{u^2}{2\sigma_{0,\mathrm{z}}}\right]}{\sqrt{2\pi(2\,\mathrm{n_{th}}+1)\sigma_{0,\mathrm{z}}}}\right]\right)^2 \mathrm{d}u\,.$$

Reminding the procedure for the calculation of $F(\phi)$ in the pure case, we notice that the last remaining thermal factor in the above expression (at the denominator in the logarithm) vanishes when we expand and derive the logarithm. As a result, the calculation proceeds in exactly the same way as in the pure case, leading to the same result.

Appendix C

Calculation of posterior probability distribution

In this section we calculate the posterior probability distribution for homodyne detection of a squeezed thermal state.
We start from the Bayes rule, $P(x|\phi)P(\phi) = P(\phi|x)P(x)$, where $P(\phi) = \frac{2}{\pi}$ corresponds to the assumption of no prior knowledge about ϕ and $P(x)$ is the overall probability of observing x. To simplify the discussion we include $P(\phi)$ and $P(x)$ in the normalization factor $\mathcal{N} = \int_0^{\pi/2} P(\phi|\{x\}_{\mathrm{M}})\mathrm{d}\phi$. We start inverting the Bayes rule to explicit the posterior probability distribution:

$$P(\phi|x) = \frac{1}{\mathcal{N}} P(x|\phi)\,.$$

After M independent measurements we collect the data set $\{x\}_{\mathrm{M}}$, and the PPD writes:

$$P(\phi|\{x\}_{\mathrm{M}}) = \frac{1}{\mathcal{N}} \prod_{k=1}^{M} P(x_k|\phi)\,.$$

In the limit of a large number of samples, $M \gg 1$, we can write the number of occurrences of x as $MP(x|\phi^*)$, where ϕ^* is the actual (unknown) value of the

parameter:

$$
\begin{aligned}
P(\phi|\{x\}_{\mathrm{M}}) &\overset{M\gg 1}{\simeq} \frac{1}{\mathcal{N}}\prod_x P(x|\phi)^{MP(x|\phi^*)} = \frac{1}{\mathcal{N}}\mathrm{Exp}\left[\log\left[\prod_x P(x|\phi)^{MP(x|\phi^*)}\right]\right] = \\
&= \frac{1}{\mathcal{N}}\mathrm{Exp}\left[\sum_x \log\left[P(x|\phi)^{MP(x|\phi^*)}\right]\right] = \\
&= \frac{1}{\mathcal{N}}\mathrm{Exp}\left[M\sum_x P(x|\phi^*)\log\left[P(x|\phi)\right]\right] \overset{M\gg 1}{\simeq} \\
&\overset{M\gg 1}{\simeq} \frac{1}{\mathcal{N}}\mathrm{Exp}\left[M\int_{-\infty}^{+\infty}\mathrm{d}x\; P(x|\phi^*)\log\left[P(x|\phi)\right]\right]
\end{aligned}
$$

We may now substitute the homodyne probability distribution $P(x|\phi)$, 3.18:

$$
\begin{aligned}
P(\phi|\{x\}_M) &= \frac{1}{\mathcal{N}}\mathrm{Exp}\left[M\int \mathrm{d}x\; \frac{1}{\sqrt{2\pi\delta^2_{\phi^*}}}e^{-\frac{x^2}{2\delta^2_{\phi^*}}}\log\left[\frac{1}{\sqrt{2\pi\delta^2_{\phi}}}e^{-\frac{x^2}{2\delta^2_{\phi}}}\right]\right] = \\
&= \frac{1}{\mathcal{N}}\mathrm{Exp}\left[\frac{M}{\sqrt{2\pi\delta^2_{\phi^*}}}\left(-\frac{1}{2}\log\left[2\pi\delta^2_{\phi}\right]\int \mathrm{d}x\; e^{-\frac{x^2}{2\delta^2_{\phi^*}}} - \frac{1}{2\delta^2_{\phi}}\int \mathrm{d}x\; x^2 e^{-\frac{x^2}{2\delta^2_{\phi^*}}}\right)\right] = \\
&= \frac{1}{\mathcal{N}}\mathrm{Exp}\left[-\frac{M\log\left[2\pi\delta^2_{\phi}\right]}{2\sqrt{2\pi\delta^2_{\phi^*}}}\int \mathrm{d}x\; e^{-\frac{x^2}{2\delta^2_{\phi^*}}}\right]\mathrm{Exp}\left[-\frac{M}{2\delta^2_{\phi}\sqrt{2\pi\delta^2_{\phi^*}}}\int \mathrm{d}x\; x^2 e^{-\frac{x^2}{2\delta^2_{\phi^*}}}\right] = \\
&= \frac{1}{\mathcal{N}}\mathrm{Exp}\left[\log\left[(2\pi\delta^2_{\phi})^{-M/2}\right]\right]\mathrm{Exp}\left[-\frac{M\delta^2_{\phi^*}}{2\delta^2_{\phi}}\right] = \frac{1}{\mathcal{N}}\frac{1}{(2\pi\delta^2_{\phi})^{M/2}}e^{-\frac{M\delta^2_{\phi^*}}{2\delta^2_{\phi}}}
\end{aligned}
$$

where we used the Gaussian integrals

$$
\begin{aligned}
\int_{-\infty}^{+\infty}\mathrm{d}x\; e^{-\frac{x^2}{2\delta^2_{\phi^*}}} &= \sqrt{2\pi\delta^2_{\phi^*}} \\
\int_{-\infty}^{+\infty}\mathrm{d}x\; x^2 e^{-\frac{x^2}{2\delta^2_{\phi^*}}} &= \frac{1}{2}\sqrt{\pi(2\delta^2_{\phi^*})^3}
\end{aligned}
$$

Appendix D

Bow-tie cavity

To produce squeezed light for the experiments described in Chapter 4 and Chapter 5 we use the nonlinear interaction generated in a 10 mm long PPKTP crystal designed for type I parametric down-conversion (see Fig.D.1). The crystal is pumped with a 532 nm pump beam and generates squeezed light at 1064 nm. The crystal is characterized by a surface reflectivity of 0.2% to reduce losses due to back-reflection. To enhance the down-conversion efficiency the crystal is placed in a 0.25 m long bow-tie cavity designed to be resonant at 1064 nm. The phase matching condition for the down-conversion process is ensured by a Peltier element which keeps the crystal at optimal temperature ($\simeq$ 30 degrees). The incoupling mirror is HR-coated for a reflectivity of 0.998, while the outcoupling mirror has a lower reflectivity of 0.92. The cavity is characterized by $\sim$ 0.5% of intracavity losses, a finesse of $\sim$ 73, a bandwidth of $\sim$ 16 MHz and a free spectral range of $\sim$ 1.2 GHz. The outcoupling efficiency is $\sim$ 95%.
Three beams of light enter the cavity: a pump beam at 532 nm modulated at 12 MHz; a seed beam at 1064 nm in a TEM00 mode; a lock beam at 1064 nm in a frequency-shifted TEM01 mode with a 25 MHz modulation.
Locking of the cavity on resonance is achieved using an AC lock. The lock beam counter-propagates in the cavity with respect to the seed beam, and it is detected by a resonant photodetector after the cavity. In order to avoid interference between the lock beam and the seed, the lock beam is kept in a TEM01 mode and frequency-shifted by an acousto-optical modulator to match the resonant frequency of the cavity. Once the lock beam is detected, an error signal is produced by mixing down the photodetector signal with the 25 MHz electronic oscillator. The resulting error signal is fed to a proportional-integral controller that drives a piezoelectric element situated on the back of the outcoupling mirror.

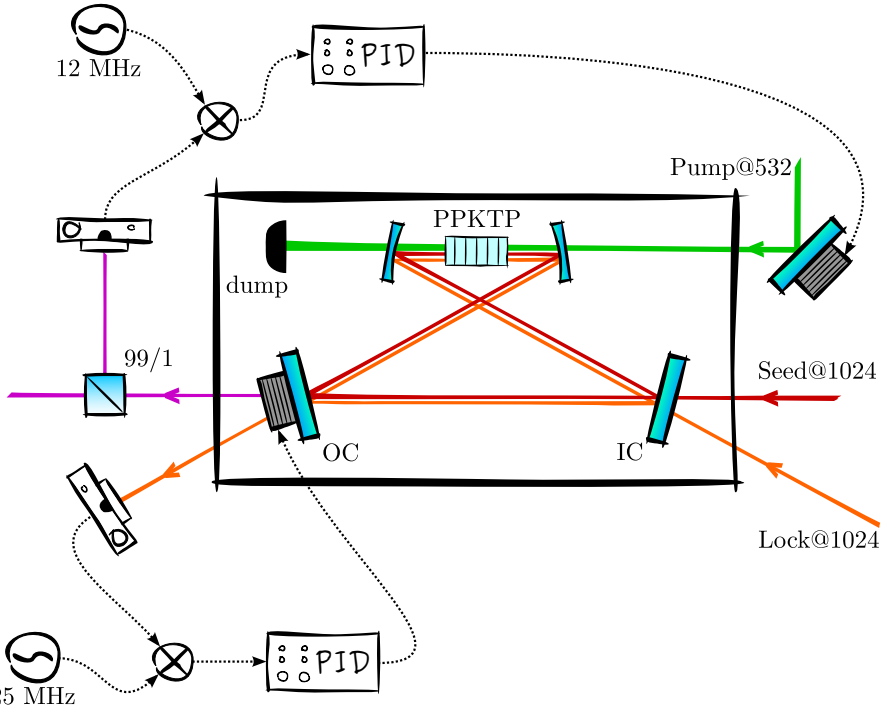

Figure D.1: **Bow-tie cavity for the generation of squeezed light.** PID: proportional-integral-derivative controller; PPKTP: periodically poled potassium titanyl phosphate; OC: output coupler; IC: input coupler.

The seed beam provides a reference for locking the squeezing phase. Locking of the squeezing phase is accomplished via AC-lock. After the cavity the output seed beam enters a 99/1 beam splitter, where a fraction of the light is diverted into a resonant photodetector. The signal from such detector is mixed down with the 12 MHz electronic oscillator that modulates the pump beam. The resulting error signal is fed to a PI controller which drives a piezoelectric element on the pump beam path. In this way the squeezing phase is set as the relative phase between the pump beam and the seed in either an amplitude or a phase squeezing configuration.

Bibliography

[1] Vittorio Giovannetti, Seth Lloyd, and Lorenzo Maccone. Quantum-enhanced measurements: Beating the standard quantum limit. *Science*, **306**(5700):1330–1336, 2004. http://www.sciencemag.org/content/306/5700/1330.abstract.

[2] Vittorio Giovannetti, Seth Lloyd, and Lorenzo Maccone. Advances in quantum metrology. *Nat. Phot.*, **5**(4):222–229, 2011. http://dx.doi.org/10.1038/nphoton.2011.35.

[3] David P. DiVincenzo. Quantum computation. *Science*, **270**(5234):255–261, 1995. http://www.sciencemag.org/content/270/5234/255.abstract.

[4] Andrew M. Steane. Error correcting codes in quantum theory. *Phys. Rev. Lett.*, **77**(5):793–797, 1996. http://link.aps.org/doi/10.1103/PhysRevLett.77.793.

[5] Nicolas Gisin, Grégoire Ribordy, Wolfgang Tittel, and Hugo Zbinden. Quantum cryptography. *Rev. Mod. Phys.*, **74**(1):145–195, 2002. http://link.aps.org/doi/10.1103/RevModPhys.74.145.

[6] Charles H. Bennett, Gilles Brassard, Claude Crépeau, Richard Jozsa, Asher Peres, and William K. Wootters. Teleporting an unknown quantum state via dual classical and Einstein-Podolsky-Rosen channels. *Phys. Rev. Lett.*, **70**(13):1895–1899, 1993. http://link.aps.org/doi/10.1103/PhysRevLett.70.1895.

[7] Charles Bennett and Stephen Wiesner. Communication via one- and two-particle operators on Einstein-Podolsky-Rosen states. *Phys. Rev. Lett.*, **69**(20):2881–2884, 1992. http://link.aps.org/doi/10.1103/PhysRevLett.69.2881.

[8] Christian Weedbrook, Stefano Pirandola, Raúl García-Patrón, Nicolas Cerf, Timothy Ralph, Jeffrey Shapiro, and Seth Lloyd. Gaussian quantum information. *Rev. Mod. Phys.*, **84**(2):621–669, 2012. http://link.aps.org/doi/10.1103/RevModPhys.84.621.

[9] Gerardo Adesso, Sammy Ragy, and Antony R. Lee. Continuous variable quantum information: Gaussian states and beyond. *Open Syst. Inf. Dyn.*, **21**(01n02):1440001, 2014. http://www.worldscientific.com/doi/abs/10.1142/S1230161214400010.

[10] Reinhard F. Werner. Quantum states with Einstein-Podolsky-Rosen correlations admitting a hidden-variable model. *Phys. Rev. A*, **40**(8):4277–4281, 1989. http://link.aps.org/doi/10.1103/PhysRevA.40.4277.

[11] Ulf Leonhardt. *Measuring the quantum state of light.* Cambridge University Press, 1997.

[12] Alessandro Ferraro, Stefano Olivares, and Matteo G. A. Paris. *Gaussian states in quantum information.* Bibliopolis, Napoli, 2005.

[13] Rajiah Simon, Narasimhaiengar Mukunda, and Biswadeb Dutta. Quantum-noise matrix for multimode systems: U(n) invariance, squeezing, and normal forms. *Phys. Rev. A*, **49**(3):1567–1583, 1994. http://link.aps.org/doi/10.1103/PhysRevA.49.1567.

[14] Robin L. Hudson. When is the wigner quasi-probability density non-negative? *Reports on Mathematical Physics*, **6**(2):249–252, 1974. http://www.sciencedirect.com/science/article/pii/003448777490007X.

[15] Aikaterini Mandilara, Evgueni Karpov, and Nicolas J. Cerf. Extending hudson's theorem to mixed quantum states. *Phys. Rev. A*, **79**(6):062302, 2009. http://link.aps.org/doi/10.1103/PhysRevA.79.062302.

[16] Rajiah Simon, George E. C. Sudarshan, and Narasimhaiengar Mukunda. Gaussian pure states in quantum mechanics and the symplectic group. *Phys. Rev. A*, **37**(8):3028–3038, 1988. http://link.aps.org/doi/10.1103/PhysRevA.37.3028.

[17] Roy J. Glauber. Coherent and incoherent states of the radiation field. *Phys. Rev.*, **131**(6):2766–2788, 1963. http://link.aps.org/doi/10.1103/PhysRev.131.2766.

[18] David Stoler. Equivalence classes of minimum uncertainty packets. *Phys. Rev. D*, **1**(12):3217–3219, 1970. http://link.aps.org/doi/10.1103/PhysRevD.1.3217.

[19] Cristopher C. Gerry and Peter L. Knight. *Introductory Quantum Optics*. Cambridge University Press, 2005.

[20] Matteo G.A. Paris. Joint generation of identical squeezed states. *Phys. Lett. A*, **225**(1–3):28–32, 1997. http://www.sciencedirect.com/science/article/pii/S0375960196008705.

[21] Jeff Z. Y. Ou, Silvania F. Pereira, Jeff H. Kimble, and Kunchi Peng. Realization of the Einstein-Podolsky-Rosen paradox for continuous variables. *Phys. Rev. Lett.*, **68**(25):3663–3666, 1992. http://link.aps.org/doi/10.1103/PhysRevLett.68.3663.

[22] Akira Furusawa, Jens L. Sørensen, Samuel L. Braunstein, Cristopher A. Fuchs, Jeff H. Kimble, and Eugene S. Polzik. Unconditional quantum teleportation. *Science*, **282**(5389):706–709, 1998. http://www.sciencemag.org/content/282/5389/706.abstract.

[23] Michael A. Nielsen and Isaac L. Chuang. *Quantum Computation and Quantum Information, X Ed.* Cambridge University Press, 2011.

[24] Carl W. Helstrom. *Quantum detection and estimation theory.* Academic Press, 1946.

[25] Paul A. M. Dirac. The quantum theory of the emission and absorption of radiation. *Proc. R. Soc. London A*, **114**(767):243–265, 1927. http://rspa.royalsocietypublishing.org/content/114/767/243.

[26] William H. Louisell. Amplitude and phase uncertainty relations. *Phys. Lett.*, **7**(1):60–61, 1963. http://www.sciencedirect.com/science/article/pii/0031916363904426.

[27] Robert Lynch. The quantum phase problem: a critical review. *Phys. Rep.*, **256**(6):367–436, 1995. http://www.sciencedirect.com/science/article/pii/037015739400095K.

[28] Peter A. Carruthers and Michael M. Nieto. Phase and angle variables in quantum mechanics. *Rev. Mod. Phys.*, **40**(2):411–440, 1968. http://link.aps.org/doi/10.1103/RevModPhys.40.411.

[29] Leonard Susskind and Jonathan Glogower. Quantum mechanical phase and time operator. *Physics*, **1**:49, 1964.

[30] Mohammed Dakna, Tomáš Opatrný, and Dirk-Gunnar Welsch. Homodyne measurement of exponential phase moments. *Optics Communications*, **148**(4-6):355–375, 1998. http://www.sciencedirect.com/science/article/pii/S0030401897007013.

[31] Stephen M. Barnett and David T. Pegg. Phase in quantum optics. *J. Phys. A*, **19**(18):3849, 1986. http://stacks.iop.org/0305-4470/19/i=18/a=030.

[32] Michael J. W. Hall and Ian G. Fuss. Quantum phase detection and digital communication. *Quantum Opt.*, **3**(3):147, 1991. http://stacks.iop.org/0954-8998/3/i=3/a=002.

[33] Carlton M. Caves. Quantum-mechanical noise in an interferometer. *Phys. Rev. D*, **23**(8):1693–1708, 1981. http://link.aps.org/doi/10.1103/PhysRevD.23.1693.

[34] Keisuke Goda, Osamu Miyakawa, Eugeniy E. Mikhailov, Shailendhar Saraf, Rana Adhikari, Kirk McKenzie, Robert Ward, Steve Vass, Alan J. Weinstein, and Nergis Mavalvala. A quantum-enhanced prototype gravitational-wave detector. *Nat. Phys.*, **4**(6):472–476, 2008. http://dx.doi.org/10.1038/nphys920.

[35] The LIGO Scientific Collaboration. A gravitational wave observatory operating beyond the quantum shot-noise limit. *Nat. Phys.*, **7**(12):962–965, 2011. http://www.nature.com/nphys/journal/v7/n12/full/nphys2083.html.

[36] Matteo G.A. Paris. Small amount of squeezing in high-sensitive realistic interferometry. *Phys. Lett. A*, **201**(2–3):132–138, 1995. http://www.sciencedirect.com/science/article/pii/037596019500235U.

[37] Luca Pezzé and Augusto Smerzi. Mach-zehnder interferometry at the heisenberg limit with coherent and squeezed-vacuum light. *Phys. Rev. Lett.*, **100**(7):073601, 2008. http://link.aps.org/doi/10.1103/PhysRevLett.100.073601.

[38] Vittorio Giovannetti, Seth Lloyd, and Lorenzo Maccone. Quantum metrology. *Phys. Rev. Lett.*, **96**(1):010401, 2006. http://link.aps.org/doi/10.1103/PhysRevLett.96.010401.

[39] Tomohisa Nagata, Ryo Okamoto, Jeremy L. O'Brien, Keiji Sasaki, and Shigeki Takeuchi. Beating the standard quantum limit with four-entangled photons. *Science*, **316**(5825):726–729, 2007. http://www.sciencemag.org/content/316/5825/726.abstract.

[40] John J. Bollinger, Wayne M. Itano, David J. Wineland, and Daniel J. Heinzen. Optimal frequency measurements with maximally correlated states. *Phys. Rev. A*, **54**(6):R4649–R4652, 1996. http://link.aps.org/doi/10.1103/PhysRevA.54.R4649.

[41] Uwe Dorner, Rafal Demkowicz-Dobrzanski, Brian J. Smith, Jeff S. Lundeen, Wojciech Wasilewski, Konrad Banaszek, and Ian A. Walmsley. Optimal quantum phase estimation. *Phys. Rev. Lett.*, **102**(4):040403, 2009. http://link.aps.org/doi/10.1103/PhysRevLett.102.040403.

[42] Petr Anisimov, Gretchen Raterman, Aravind Chiruvelli, William Plick, Sean Huver, Hwang Lee, and Jonathan Dowling. Quantum metrology with two-mode squeezed vacuum: Parity detection beats the heisenberg limit. *Phys. Rev. Lett.*, **104**(10):103602, 2010. http://link.aps.org/doi/10.1103/PhysRevLett.104.103602.

[43] Jeffrey H. Shapiro and Stuart S. Wagner. Phase and amplitude uncertainties in heterodyne detection. *Quantum Elecron., IEEE Journal of*, **20**(7):803–813, 1984. http://ieeexplore.ieee.org/stamp/stamp.jsp?tp=&arnumber=1072470.

[44] Giacomo D'Ariano, Matteo Paris, and Raffaella Seno. Feedback-assisted homodyne detection of phase shifts. *Phys. Rev. A*, **54**(5):4495–4504, 1996. http://link.aps.org/doi/10.1103/PhysRevA.54.4495.

[45] Horace P. Yuen. Generalized quantum measurements and approximate simultaneous measurements of noncommuting observables. *Phys. Lett. A*, **91**(3):101–104, 1982. http://www.sciencedirect.com/science/article/pii/0375960182903590.

[46] Alex Monras. Optimal phase measurements with pure gaussian states. *Phys. Rev. A*, **73**(3):033821, 2006. http://link.aps.org/doi/10.1103/PhysRevA.73.033821.

[47] Howard M. Wiseman and Rowan B. Killip. Adaptive single-shot phase measurements: A semiclassical approach. *Phys. Rev. A*, **56**(1):944–957, 1997. http://link.aps.org/doi/10.1103/PhysRevA.56.944.

[48] Howard M. Wiseman and Rowan B. Killip. Adaptive single-shot phase measurements: The full quantum theory. *Phys. Rev. A*, **57**(3):2169–2185, 1998. http://link.aps.org/doi/10.1103/PhysRevA.57.2169.

[49] Michael Armen, John Au, John Stockton, Andrew Doherty, and Hideo Mabuchi. Adaptive homodyne measurement of optical phase. *Phys. Rev. Lett.*, **89**(13):133602, 2002. http://link.aps.org/doi/10.1103/PhysRevLett.89.133602.

[50] Hidehiro Yonezawa, Daisuke Nakane, Trevor A. Wheatley, Kohjiro Iwasawa, Shuntaro Takeda, Hajime Arao, Kentaro Ohki, Koji Tsumura, Dominic W. Berry, Timothy C. Ralph, Howard M. Wiseman, Elanor H. Huntington, and Akira Furusawa. Quantum-enhanced optical-phase tracking. *Science*, **337**(6101):1514–1517, 2012. http://www.sciencemag.org/content/337/6101/1514.abstract.

[51] Harald Cramér. *Mathematical Methods of Statistics*. Princeton University Press, 1946.

[52] Carl W. Helstrom. Minimum mean-squared error of estimates in quantum statistics. *Phys. Lett. A*, **25**(2):101–102, 1967. http://www.sciencedirect.com/science/article/pii/0375960167903660.

[53] Richard D. Gill and Serge Massar. State estimation for large ensembles. *Phys. Rev. A*, **61**(4):042312, 2000. http://link.aps.org/doi/10.1103/PhysRevA.61.042312.

[54] Stefano Olivares and Matteo G A Paris. Bayesian estimation in homodyne interferometry. *J. Phys. B*, **42**(5):055506, 2009. http://stacks.iop.org/0953-4075/42/i=5/a=055506.

[55] Sergio Boixo, Steven T. Flammia, Carlton M. Caves, and JM Geremia. Generalized limits for single-parameter quantum estimation. *Phys. Rev. Lett.*, **98**(9):090401, 2007. http://link.aps.org/doi/10.1103/PhysRevLett.98.090401.

[56] Zden ěk Hradil, Robert Myška, Tomá š Opatrný, and Ji říBajer. Entropy of phase measurement: Quantum phase via quadrature measurement. *Phys. Rev. A*, **53**(6):3738–3742, 1996. http://link.aps.org/doi/10.1103/PhysRevA.53.3738.

[57] L. Pezzé, A. Smerzi, G. Khoury, J. F. Hodelin, and D. Bouwmeester. Phase detection at the quantum limit with multiphoton mach-zehnder interferom-

etry. *Phys. Rev. Lett.*, **99**(22):223602, 2007. http://link.aps.org/doi/10.1103/PhysRevLett.99.223602.

[58] Samuel L. Braunstein. How large a sample is needed for the maximum likelihood estimator to be approximately gaussian? *J. of Phys. A*, **25**(13):3813, 1992. http://stacks.iop.org/0305-4470/25/i=13/a=027.

[59] Lucien Le Cam. *Asymptotic methods in statistical decision theory.* Springer-Verlag, 1986.

[60] M. Aspachs, J. Calsamiglia, R. Muñoz Tapia, and E. Bagan. Phase estimation for thermal gaussian states. *Phys. Rev. A*, **79**(3):033834, 2009. http://link.aps.org/doi/10.1103/PhysRevA.79.033834.

[61] Eric D. Black. An introduction to pound–drever–hall laser frequency stabilization. *American J. of Phys.*, **69**(1):79–87, 2001. http://scitation.aip.org/content/aapt/journal/ajp/69/1/10.1119/1.1286663.

[62] A. Abramovici and J. Chapsky. *Feedback control systems, a fast-track guide for scientists and engineers.* Kluwer Academic Publishers, Boston, 2000.

[63] Tobias Eberle, Vitus Händchen, and Roman Schnabel. Stable control of 10 db two-mode squeezed vacuum states of light. *Opt. Expr.*, **21**(9):11546–11553, 2013. http://www.opticsexpress.org/abstract.cfm?URI=oe-21-9-11546.

[64] Mikael Lassen, Adriano Berni, Lars S. Madsen, Radim Filip, and Ulrik L. Andersen. Gaussian error correction of quantum states in a correlated noisy channel. *Phys. Rev. Lett.*, **111**(18):180502, 2013. http://link.aps.org/doi/10.1103/PhysRevLett.111.180502.

[65] Jeff H. Kimble. The quantum internet. *Nature*, **453**:1023–1030, 2008. http://www.nature.com/nature/journal/v453/n7198/full/nature07127.html.

[66] Lu-Ming Duan, Mikhail D. Lukin, J Cirac Ignatio, and Peter Zoller. Long-distance quantum communication with atomic ensembles and linear optics. *Nature*, **414**:413–418, 2001. http://www.nature.com/nature/journal/v414/n6862/abs/414413a0.html.

[67] Raúl García-Patrón and Nicolas J. Cerf. Continuous-variable quantum key distribution protocols over noisy channels. *Phys. Rev. Lett.*, **102**(13):130501, 2009. http://link.aps.org/doi/10.1103/PhysRevLett.102.130501.

[68] Lars S. Madsen, Vladyslav C. Usenko, Mikael Lassen, Radim Filip, and Ulrik L. Andersen. Continuous variable quantum key distribution with modulated entangled states. *Nat. Comm.*, **3**:1083, 2012. http://www.nature.com/ncomms/journal/v3/n9/full/ncomms2097.html.

[69] Stefano Pirandola, Stefano Mancini, Seth Lloyd, and Samuel L. Braunstein. Continuous-variable quantum cryptography using two-way quantum communication. *Nat. Phys.*, **4**:726–730, 2008. http://www.nature.com/nphys/journal/v4/n9/abs/nphys1018.html.

[70] Lu-Ming Duan, G. Giedke, J. I. Cirac, and P. Zoller. Entanglement purification of gaussian continuous variable quantum states. *Phys. Rev. Lett.*, **84**(17):4002–4005, 2000. http://link.aps.org/doi/10.1103/PhysRevLett.84.4002.

[71] Peter W. Shor. Scheme for reducing decoherence in quantum computer memory. *Phys. Rev. A*, **52**(4):R2493–R2496, 1995. http://link.aps.org/doi/10.1103/PhysRevA.52.R2493.

[72] Charles H. Bennett, David P. DiVincenzo, John A. Smolin, and William K. Wootters. Mixed-state entanglement and quantum error correction. *Phys. Rev. A*, **54**(5):3824–3851, 1996. http://link.aps.org/doi/10.1103/PhysRevA.54.3824.

[73] Seth Lloyd and Jean-Jacques E. Slotine. Analog quantum error correction. *Phys. Rev. Lett.*, **80**(18):4088–4091, 1998. http://link.aps.org/doi/10.1103/PhysRevLett.80.4088.

[74] R. M. Shelby, M. D. Levenson, and P. W. Bayer. Resolved forward brillouin scattering in optical fibers. *Phys. Rev. Lett.*, **54**(9):939–942, 1985. http://link.aps.org/doi/10.1103/PhysRevLett.54.939.

[75] Samuel L. Braunstein. Quantum error correction for communication with linear optics. *Nature*, **4**:47–49, 1998. http://www.nature.com/nature/journal/v394/n6688/abs/394047a0.html.

[76] Julien Niset, Ulrik L. Andersen, and Nicolas J. Cerf. Experimentally feasible quantum erasure-correcting code for continuous variables. *Phys. Rev. Lett.*, **101**(13):130503, 2008. http://link.aps.org/doi/10.1103/PhysRevLett.101.130503.

[77] Mikael Lassen, Metin Sabuncu, Alexander Huck, Julien Niset, Gerd Leuchs, Nicolas J. Cerf, and Ulrik L. Andersen. Quantum optical coherence can sur-

vive photon losses using a continuous-variable quantum erasure-correcting code. *Nat. Phot.*, **4**:700–705, 2010. http://www.nature.com/nphoton/journal/v4/n10/full/nphoton.2010.168.html.

[78] Ruifang Dong, Mikael Lassen, Joel Heersink, Christoph Marquardt, Radim Filip, Gerd Leuchs, and Ulrik L. Andersen. Experimental entanglement distillation of mesoscopic quantum states. *Nat. Phys.*, **4**:919–923, 2008. http://www.nature.com/nphys/journal/v4/n12/abs/nphys1112.html.

[79] Jens Eisert, Stefan Scheel, and Martin B. Plenio. Distilling gaussian states with gaussian operations is impossible. *Phys. Rev. Lett.*, **89**(13):137903, 2002. http://link.aps.org/doi/10.1103/PhysRevLett.89.137903.

[80] Jaromír Fiurášek. Gaussian transformations and distillation of entangled gaussian states. *Phys. Rev. Lett.*, **89**(13):137904, 2002. http://link.aps.org/doi/10.1103/PhysRevLett.89.137904.

[81] Julien Niset, Jaromír Fiurášek, and Nicolas J. Cerf. No-go theorem for gaussian quantum error correction. *Phys. Rev. Lett.*, **102**(12):120501, 2009. http://link.aps.org/doi/10.1103/PhysRevLett.102.120501.

[82] Jens Eisert, Dan E. Browne, Stefan Scheel, and Martin B. Plenio. Distillation of continuous-variable entanglement with optical means. *Ann. Phys.*, **311**(2):431–458, 2004. http://www.sciencedirect.com/science/article/pii/S0003491604000041.

[83] Hiroki Takahashi, Jonas N. Neergaard-Nielsen, Makoto Takeuchi, Masahiro Takeoka, Kazuhiro Hayasaka, Akira Furusawa, and Masahide Sasaki. Entanglement distillation from gaussian input states. *Nat. Phot.*, **4**:178–181, 2010. http://www.nature.com/nphoton/journal/v4/n3/abs/nphoton.2010.1.html.

[84] Dennis Kretschmann and Reinhard F. Werner. Quantum channels with memory. *Phys. Rev. A*, **72**(6):062323, 2005. http://link.aps.org/doi/10.1103/PhysRevA.72.062323.

[85] Joel F. Corney, Peter D. Drummond, Joel Heersink, Vincent Josse, Gerd Leuchs, and Ulrik L. Andersen. Many-body quantum dynamics of polarization squeezing in optical fibers. *Phys. Rev. Lett.*, **97**(2):023606, 2006. http://link.aps.org/doi/10.1103/PhysRevLett.97.023606.

[86] Vittorio Giovannetti and Stefano Mancini. Bosonic memory channels. *Phys. Rev. A*, **71**(6):062304, 2005. http://link.aps.org/doi/10.1103/PhysRevA.71.062304.

[87] Nicolas J. Cerf, Julien Clavareau, Chiara Macchiavello, and Jérémie Roland. Quantum entanglement enhances the capacity of bosonic channels with memory. *Phys. Rev. A*, **72**(4):042330, 2005. http://link.aps.org/doi/10.1103/PhysRevA.72.042330.

[88] Cosmo Lupo, Vittorio Giovannetti, and Stefano Mancini. Capacities of lossy bosonic memory channels. *Phys. Rev. Lett.*, **104**(3):030501, 2010. http://link.aps.org/doi/10.1103/PhysRevLett.104.030501.

[89] Metin Sabuncu, Radim Filip, Gerd Leuchs, and Ulrik L. Andersen. Environment-assisted quantum-information correction for continuous variables. *Phys. Rev. A*, **81**(1):012325, 2010. http://link.aps.org/doi/10.1103/PhysRevA.81.012325.

[90] Lu-Ming Duan, G. Giedke, J. I. Cirac, and P. Zoller. Inseparability criterion for continuous variable systems. *Phys. Rev. Lett.*, **84**(12):2722–2725, 2000. http://link.aps.org/doi/10.1103/PhysRevLett.84.2722.

[91] Rajiah Simon. Peres-horodecki separability criterion for continuous variable systems. *Phys. Rev. Lett.*, **84**(12):2726–2729, 2000. http://link.aps.org/doi/10.1103/PhysRevLett.84.2726.

[92] Claude Shannon. A mathematical theory of communication. *Bell System Technical Journal*, **27**:379–423, 623–656, 1948. http://cm.bell-labs.com/cm/ms/what/shannonday/shannon1948.pdf.

[93] Thomas M. Cover and Joy A. Thomas. *Elements of Information Theory, II Ed.* Wiley-Interscience, 2006.

[94] Leah Henderson and Vlatko Vedral. Classical, quantum and total correlations. *J. of Phys. A*, **34**(35):6899–6905, 2001. http://stacks.iop.org/0305-4470/34/i=35/a=315.

[95] Harold Ollivier and Wojciech H. Zurek. Quantum discord: A measure of the quantumness of correlations. *Phys. Rev. Lett.*, **88**(1):017901, 2001. http://link.aps.org/doi/10.1103/PhysRevLett.88.017901.

[96] Animesh Datta. A condition for the nullity of quantum discord, ArXiv:1003.5256v2 [quant-ph]. 2011. http://link.aps.org/doi/10.1103/PhysRevA.83.052108.

[97] Davide Girolami and Gerardo Adesso. Quantum discord for general two-qubit states: Analytical progress. *Phys. Rev. A*, **83**(5):052108, 2011. http://link.aps.org/doi/10.1103/PhysRevA.83.052108.

[98] Richard Tatham, Ladislav Mišta, Gerardo Adesso, and Natalia Korolkova. Nonclassical correlations in continuous-variable non-gaussian werner states. *Phys. Rev. A*, **85**(2):022326, 2012. http://link.aps.org/doi/10.1103/PhysRevA.85.022326.

[99] Paolo Giorda and Matteo G. A. Paris. Gaussian quantum discord. *Phys. Rev. Lett.*, **105**(2):020503, 2010. http://link.aps.org/doi/10.1103/PhysRevLett.105.020503.

[100] Gerardo Adesso and Animesh Datta. Quantum versus classical correlations in gaussian states. *Phys. Rev. Lett.*, **105**(3):030501, 2010. http://link.aps.org/doi/10.1103/PhysRevLett.105.030501.

[101] John Williamson. On the algebraic problem concerning the normal forms of linear dynamical systems. *Am. J. of Math.*, **58**(1):141–163, 1936. http://www.jstor.org/stable/2371062.

[102] Alessio Serafini, Fabrizio Illuminati, and Silvio De Siena. Symplectic invariants, entropic measures and correlations of gaussian states. *J. Phys. B*, **37**(2):L21, 2004. http://stacks.iop.org/0953-4075/37/i=2/a=L02.

[103] Alexander S. Holevo and Reinhard F. Werner. Evaluating capacities of bosonic gaussian channels. *Phys. Rev. A*, **63**(3):032312, 2001. http://link.aps.org/doi/10.1103/PhysRevA.63.032312.

[104] Jaromír Fiurášek and Ladislav Mišta. Gaussian localizable entanglement. *Phys. Rev. A*, **75**(6):060302, 2007. http://link.aps.org/doi/10.1103/PhysRevA.75.060302.

[105] Jens Eisert and Martin B. Plenio. Introduction to the basics of entanglement theory in continuous-variable systems. *Int. J. Quantum Inform.*, **01**(04):479–506, 2003. http://www.worldscientific.com/doi/abs/10.1142/S0219749903000371.

[106] Géza Giedke and J. Ignacio Cirac. Characterization of gaussian operations and distillation of gaussian states. *Phys. Rev. A*, **66**(3):032316, 2002. http://link.aps.org/doi/10.1103/PhysRevA.66.032316.

[107] Lars S. Madsen, Adriano Berni, Mikael Lassen, and Ulrik L. Andersen. Experimental investigation of the evolution of gaussian quantum discord in an

open system. *Phys. Rev. Lett.*, **109**(3):030402, 2012. http://link.aps.org/doi/10.1103/PhysRevLett.109.030402.

[108] Emanuel Knill and Raymond Laflamme. Power of one bit of quantum information. *Phys. Rev. Lett.*, **81**(25):5672–5675, 1998. http://link.aps.org/doi/10.1103/PhysRevLett.81.5672.

[109] Ben P. Lanyon, Marco Barbieri, Marcelo P. Almeida, and Andrew G. White. Experimental quantum computing without entanglement. *Phys. Rev. Lett.*, **101**(20):200501, 2008. http://link.aps.org/doi/10.1103/PhysRevLett.101.200501.

[110] Frederic Grosshans, Gilles Van Assche, Jerome Wenger, Rosa Brouri, Nicolas J. Cerf, and Philippe Grangier. Quantum key distribution using gaussian-modulated coherent states. *Nature*, **421**:238–241, 2003. http://www.nature.com/nature/journal/v421/n6920/suppinfo/nature01289_S1.html.

[111] Animesh Datta, Anil Shaji, and Carlton M. Caves. Quantum discord and the power of one qubit. *Phys. Rev. Lett.*, **100**(5):050502, 2008. http://link.aps.org/doi/10.1103/PhysRevLett.100.050502.

[112] Marco Piani, Paweł Horodecki, and Ryszard Horodecki. No-local-broadcasting theorem for multipartite quantum correlations. *Phys. Rev. Lett.*, **100**(9):090502, 2008. http://link.aps.org/doi/10.1103/PhysRevLett.100.090502.

[113] Kavan Modi, Hugo Cable, Mark Williamson, and Vlatko Vedral. Quantum correlations in mixed-state metrology. *Phys. Rev. X*, **1**(2):021022, 2011. http://link.aps.org/doi/10.1103/PhysRevX.1.021022.

[114] Alessandro Ferraro, Leandro Aolita, Daniel Cavalcanti, Fernando M. Cucchietti, and Antonio Acín. Almost all quantum states have nonclassical correlations. *Phys. Rev. A*, **81**(5):052318, 2010. http://link.aps.org/doi/10.1103/PhysRevA.81.052318.

[115] Alexander Streltsov, Hermann Kampermann, and Dagmar Bruß. Behavior of quantum correlations under local noise. *Phys. Rev. Lett.*, **107**(17):170502, 2011. http://link.aps.org/doi/10.1103/PhysRevLett.107.170502.

[116] Steve Campbell, Tony J. G. Apollaro, Carlo Di Franco, Leonardo Banchi, Alessandro Cuccoli, Ruggero Vaia, Francesco Plastina, and Mauro Paternostro. Propagation of nonclassical correlations across a quantum spin chain.

Phys. Rev. A, **84**(5):052316, 2011. http://link.aps.org/doi/10.1103/PhysRevA.84.052316.

[117] Francesco Ciccarello and Vittorio Giovannetti. Creating quantum correlations through local nonunitary memoryless channels. *Phys. Rev. A*, **85**(1):010102, 2012. http://link.aps.org/doi/10.1103/PhysRevA.85.010102.

[118] Francesco Ciccarello and Vittorio Giovannetti. Local-channel-induced rise of quantum correlations in continuous-variable systems. *Phys. Rev. A*, **85**(2):022108, 2012. http://link.aps.org/doi/10.1103/PhysRevA.85.022108.

[119] Warwick P. Bowen, Roman Schnabel, Ping K. Lam, and Tim C. Ralph. Experimental investigation of criteria for continuous variable entanglement. *Phys. Rev. Lett.*, **90**(4):043601, 2003. http://link.aps.org/doi/10.1103/PhysRevLett.90.043601.

[120] Guifre Vidal and Reinhard F. Werner. Computable measure of entanglement. *Phys. Rev. A*, **65**(3):032314, 2002. http://link.aps.org/doi/10.1103/PhysRevA.65.032314.

[121] Ryszard Horodecki, Paweł Horodecki, Michał Horodecki, and Karol Horodecki. Quantum entanglement. *Rev. Mod. Phys.*, **81**(2):865–942. http://link.aps.org/doi/10.1103/RevModPhys.81.865.